DNA Condensate Morphology – Examples from the Test Tube and Nature

A Thesis

Presented to

The Academic Faculty

by

Igor D. Vilfan

In Partial Fulfillment

of the Requirements for the Degree

Doctor of Philosophy in Chemistry

Georgia Institute of Technology

August 2005

DNA Condensate Morphology – Examples from the Test Tube and Nature

Approved by:

Dr. Nicholas V. Hud, Advisor
School of Chemistry and Biochemistry
Georgia Institute of Technology

Dr. Roger M. Wartell
School of Biology
Georgia Institute of Technology

Dr. Donald F. Doyle
School of Chemistry and Biochemistry
Georgia Institute of Technology

Dr. Lore Williams
School of Chemistry and Biochemistry
Georgia Institute of Technology

Dr. Rigoberto Hernandez
School of Chemistry and Biochemistry
Georgia Institute of Technology

Date Approved: July 8th, 2005

‘’… It is astonishing and incredible to us, but not to Nature; for she performs with utmost ease and simplicity things which are even infinitely puzzling to our minds, and what is very difficult for us to comprehend is quite easy for her to perform.’’

Galileo, *The Two Chief World Systems*

DEDICATION

I would like to dedicate this thesis to my dear friend Helena Pezdir. Thank you for all those years we spent together growing up and showing me that an absolute determination to achieve any goals we may set for ourselves is the only possible way to success! The way you led your life will always be an inspiration for everything I do.

ACKNOWLEDGMENT

I would like to thank Dr. Nicholas V. Hud for putting a Georgia Tech poster up at University of Ljubljana, Slovenia, by which I got inspired to apply to graduate school in Atlanta. Also, I would like to thank him for giving me an opportunity to work on a very exciting project of DNA condensation that transformed my view of Nature's most popular molecule, and to help me realize it is simply not possible for a molecule like this to cease to amaze us.

I would like to thank my parents Boštjan and Marjetka Vilfan for their unconditional support through all the years leading to my graduation; from my ABCs in the first grade to our weekly phone conversations across the Atlantic which came as a true encouragement in times when experiments alone were not enough! I thank my siblings Tanja and Aleš for all the understanding and making me believe that anybody can be whatever they want.

I would like to thank many friends and colleagues here in Atlanta for being a true family in a foreign country. To everybody in Dr. Hud's laboratory that made days at work like being on a set of a sit-com. Also, to all my friends beyond the confinements of the laboratory with whom we perfected the art of Sunday brunches.

And last but not least, I would like to thank Yolande Berta for teaching me how to use the TEM, and to be ready to help whenever the green lights of the microscope went blank.

TABLE OF CONTENTS

LIST OF TABLES

LIST OF FIGURES

LIST OF SYMBOLS AND ABBREVIATIONS

AFM	Atomic Force Microscopy
B	Second viral coefficient
bp	Base pair
c	Concentration [$g \cdot mL^{-1}$]
Cryo-TEM	Cryo-Trasmission Electron Microscopy
D	Diffusion coefficient [$cm^2 \cdot s^{-1}$]
DLS	Dynamic Light Scattering
EM	Electron Microscopy
$G(\tau)$	Autocorrelation coefficient at correlation time τ [a.u.]
G_0	Autocorrelation constant [a.u.]
I_0	Density of incident light intensity [$W \cdot m^{-2}$]
i_0	Density of scattered light intensity at zero detection angle [$W \cdot m^{-2}$]
I_{av}	Average scattered light intensity [a.u.]
I(t)	Scattered light intensity at time t [a.u.]
i_Θ	Density of scattered light intensity at detection angle Θ [$W \cdot m^{-2}$]
K	Light scattering constant [$mol \cdot m^2 \cdot g^{-2}$]
k	Boltzman constant
kb	kilo base pair
λ	Wavelength of the incident light [nm]

λ'	Wavelength of the scattered light on a moving particle [nm]
λ''	Wavelength of the scattered light on a moving particle [nm]
M	Molecular weight [$g \cdot mol^{-1}$]
N_A	Avogadro's number
n	Refractive index [ ]
η	Viscosity [$kg \cdot m^{-1} \cdot s^{-1}$]
n_0	Solvent refractive index [ ]
$P(\Theta)$	Relative density of scattered light intensity at detection angle Θ [ ]
r	Distance from the particle to the detector [m]
R_g	Radii of gyration [m]
R_h	Radii of hydration [m]
R_Θ	Rayleigh ratio [m^{-1}]
SLS	Static Light Scattering
T	Temperature [K]
t	Time [s]
TEM	Transmission Electron Microscopy

SUMMARY

DNA condensation is a process, where semi-flexible and highly charged DNA molecule undergoes a drastic reduction in its solution dimensions upon neutralization of DNA backbone phosphate groups by multivalent counterion. In biology, *in vitro* DNA condensation has been used for studying the structure of densely packed DNA such as spooled structures observed in viral capsids. As a result, *in vitro* studies of condensed spooled DNA structures obtained with multivalent counterions have provided a wealth of information on biologically relevant viral DNA structures.

In polymer science, *in vitro* DNA condensation has served as a model system for testing polyelectrolyte condensation theories, theories that often consider exclusively the kinetic or exclusively the thermodynamic factors governing polyelectrolyte condensate size and morphology. The research presented in this dissertation provides a biophysical study of DNA condensate morphology and size with the analysis of the kinetic and thermodynamic factors governing DNA condensate formation. The results demonstrate that the condensate morphology and size obtained in a commonly used DNA condensation model system cannot be explained in the context of either only kinetics or only thermodynamics of DNA condensate formation, which implies that future experimental testing of polyelectrolyte theories with *in vitro* DNA condensation model systems must consider both kinetic and thermodynamic factors.

In addition to the study of *in vitro* DNA condensation as a model system for polyelectrolyte condensation, *in vitro* DNA condensation was also applied to study the compaction of DNA by protamine I, which is a major DNA packing protein in

mammalian sperm cell chromatin. The results of the study of protamine-assisted DNA condensation were used to propose a model for the local structure of the bull protamine-DNA complex.

1. INTRODUCTION

For more than thirty years biophysicists have been intrigued by the observation that multivalent cations can cause DNA in solution to collapse into nanometer-scale structures (1-3). The properties of the particles that form in solutions of DNA and multivalent counterions depend on their respective concentrations, and DNA phosphate to multivalent counterion charge ratios (4-12). DNA condensation has been used to refer more specifically to the phenomenon in which DNA in the presence of multivalent counterions collapses into ordered nanometer-scale particles of well defined morphology (13,14). This is to distinguish DNA condensation from other DNA and multivalent counterion concentration conditions where DNA collapses into morphologically less defined structures (i.e. at high DNA to multivalent counterion charge ratio) or conditions at which DNA remains in a uncondensed conformation (i.e. at low DNA to multivalent counterion charge ratio).

DNA condensation is more than a mere curiosity, as DNA condensates have served as models of high density packing in biological systems, particularly in viruses and sperm cells (15,16), and have found applications (either by design or serendipity) in artificial gene delivery (17). The power of biology to prepare monodisperesed DNA polymers thousands of nucleotide units in length has also made DNA condensates attractive to polymer physicists as a model of polymer phase transitions and polyelectrolyte collapse (18-24). However, despite the many and diverse experiments

conducted on DNA condensation, the answers to some fundamental questions concerning DNA condensation have proven rather illusive, both to experimentalists and to theoreticians. Fortunately, continued research on the problem of DNA condensate structure and formation has produced substantial new results and insights during the past several years.

1.1. Intermolecular forces in DNA condensation

Ever since *in vitro* DNA condensation was first observed in the early seventies of the past century (25), theoreticians and experimentalist alike have been trying to understand the nature of attractive forces that drive the collapse of a highly-negatively-charged DNA polymer in the presence of counterions with a charge +3 or higher (26-38). The proposed attractive forces can be devided into several different groups: (1) hydration forces (31-33,39,40), (2) long-range attractive forces (34-36,41), and (3) attractive forces arising from the correlated counterion fluctuations (26,30,37,42-50).

Hydration forces have been proposed to arise from reconfiguration of water molecules located between macromolecular surfaces, which is promoted by the polyvalent counterions bound to DNA (32,39). The observation of aggregation of mononucleosomal DNA in the absence of multivalent cations has lead some investigators to suggest that attraction results from the enhanced translation entropy of the condensed counterions as they share the space between the like-charged polyions (e.g. DNA) (36). However, extensive theoretical work by several groups during the past ten years suggests that DNA condensation is a result of an attractive potential between DNA molecules at

close range due to the correlated fluctuations of shared polyvalent counterions (42-50). The theory of correlated counterion fluctuations predicts that the uneven screening of charges on the polyelectrolyte molecules creates local dipoles that correlate their direction with each other to create ultimately an attractive potential between like-charged polyelectrolytes. The predictions of this theory have been confirmed by Brownian dynamics simulations (51), however, they still remain to be evaluated experimentally (52).

1.2. DNA condensate morphology

In the presence of multivalent counterions, DNA has been shown to condense into nanoscale particles with various morphologies such as toroids, rods, and spheres (Figure 1.1A-C) (13,43,53). Clusters of these morphological forms, as well as morphologically less defined aggregates, have been reported (Figure 1.1D-E) (54). The morphology of DNA condensates depends on solution conditions (e.g. solvent polarity) as well as on the properties of the DNA polymer (e.g. DNA persistance length, DNA fragment length or structural elements caused by breaks in DNA backbone) (53,55-58). The properties of the condensing agent (e.g. polarity, the number of positive charges) have also been shown to affect DNA condensate morphology. Inspite of the diversity of morphological forms adopted by condensed DNA, it has been proposed by theoreticians that toroids represent the thermodynamically most favorable state of condensed DNA with other morphologies representing metastable states (23,24,59-62).

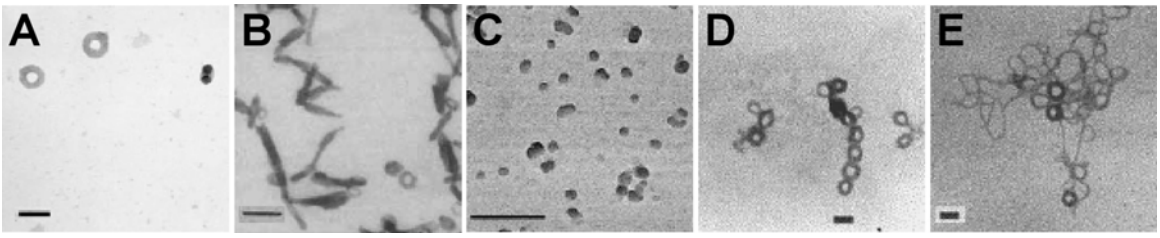

Figure 1.1 DNA condenses into different morphological forms. (A) Toroids formed by plasmid DNA with hexammine cobalt as a condensing agent. The scale bar represents 100 nm. (63) (B) Rods formed by plasmid DNA with hexammine cobalt as a condensing agent in a water-ethanol mixture as a solvent. The scale bar represents 100 nm. From: DNA condensation by cobalt hexammine(III) in Alcohol-Water Mixtures: Dielectric constant and other solvent effects; Arscott, P.G., Ma, C., Wenner, J.R., Bloomfield, V.A. *Biopolymers*, Copyright ©1995 John Wiley & Sons; Reprinted with the permission of John Wiley & Sons, Inc. (C) Spheres produced by condensing plasmid DNA with a poly-(lysine-*g*-(Lactide-*b*-ethylene glycol)) as a condensing agent. The scale bar corresponds to 500 nm. (53) (D) Clusters of toroids detected at 30 min reaction time after condensing plasmid DNA with hexammine cobalt. The scale bar represents to 100 nm. (E) Morphologically poorly defined aggregates obtained 60min after condensing plasmid DNA with hexammine cobalt. The scale bar represents 100 nm. (D)-(E) From: Condensation of DNA by multivalent cations: Experimental studies of condensation kinetics; He, S., Arscott P.G., Bloomfield, V.A. *Biopolymers*, Copyright ©2000 John Wiley & Sons; Reprinted with the permission of John Wiley & Sons, Inc.

1.3. Toroidal DNA condensates

1.3.1. DNA packing within toroids

We begin with the ever-intriguing shape of DNA toroids and how this relates to the packing of condensed DNA. The toroid morphology readily suggests that condensed DNA is circumferentially wound around the toroid, much like one would instinctively coil a length of rope or a garden hose (Figure 1.2). For optimal packing density, one might also expect the DNA strands of a toroid to be locally packed in a hexagonal lattice (Figure 1.2). Accordingly, it appears that most investigators of DNA toroids have assumed circumferential winding and hexagonal packing of DNA helices. However, the first actual experimental evidence to support the circumferential winding of DNA came

more than ten years after the discovery of DNA toroids. This evidence was provided by the freeze-fracture electron microscopy studies of Marx & Ruben (64,65) that revealed the circumferential path of one or two DNA strands around the top of individual toroids. Nevertheless, some experimental observations and theoretical arguments regarding DNA within toroids suggested that DNA might not be packing in the idealized arrangement of circumferential windings with perfect hexagonal packing of DNA helices (66,67).

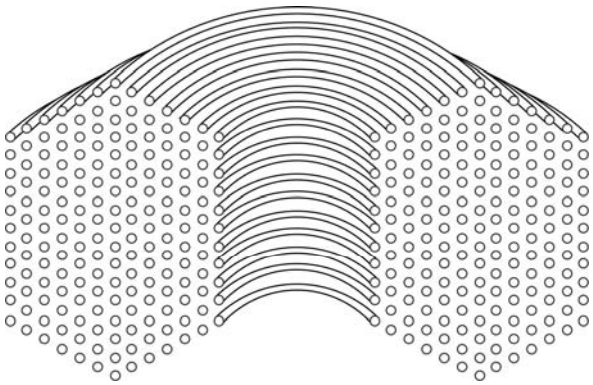

Figure 1.2 Cutaway view of an idealized DNA toroid in which DNA is circumferentially wound and packed in a perfect hexagonal lattice.

1.3.1.1. Hexagonal packing of DNA within toroids

On the basis of X-ray diffraction studies, Schellman & Parthasarathy (68) demonstrated early on that the spacing of DNA helices within toroids was consistent with hexagonal packing. However, owing to the lack of an ordered sample of DNA toroids, hexagonal packing could not be proven beyond the level of a working model. The development of cryo-electron transmission microscopy (cryo-TEM) has since made it possible to directly observe molecular architectures with nanometer-scale resolution (69,70). Böttcher et al. were the first to report the application of cryo-TEM to the study of DNA toroids. In this

study, 7.7 kb DNA was condensed with spermine and air dried onto carbon-coated EM grids (71). Cryo-TEM revealed striations with 1.8 nm spacing around the circumference of toroids that lie coplanar with the EM grids. Böttcher et al. interpreted these striations to be the interlattice spacing of DNA within the toroids. This unusually close packing of DNA helices, along with a non-B-form circular dichroism spectrum for similar DNA condensate preparations, led the authors to conclude that DNA within air-dried toroids is C-form DNA, a slightly underwound variant of B-form DNA (71).

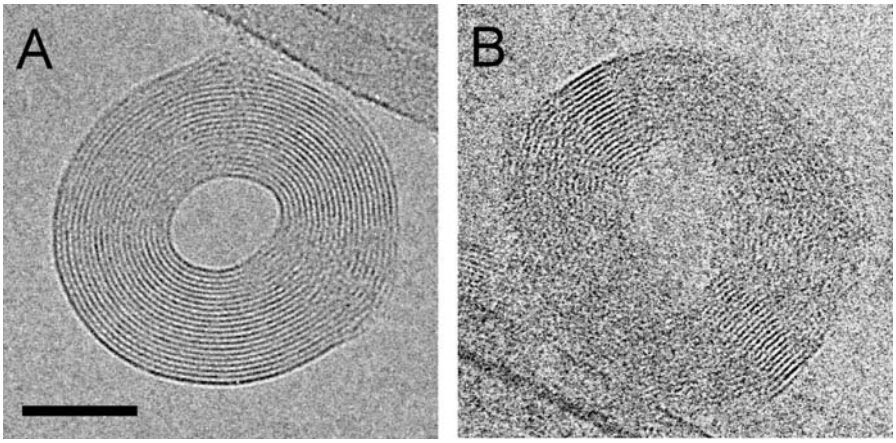

Figure 1.3 Cryoelectron micrographs of λ phage DNA toroids with the plane of the toroid approximately coplanar with the microscope image plane (i.e. top-view toroids). (A) A toroid with DNA fringes visible around almost the entire circumference of the toroid. (B) A toroid with two small arc angles of well-defined DNA fringes that appear on opposite sides of the toroid center. Scale bar is 50 nm. Adapted from reference (72).

A cryo-TEM study by Hud & Downing (72) of DNA toroids subsequently provided the next level of detail concerning the fine structure of DNA organization within toroids. In this study, toroids of λ phage DNA (48 kb) were prepared with hexammine cobalt chloride as a condensing agent, and rapidly frozen prior to imaging. The rapid freezing of toroids within a thin film had the advantage of trapping individual

toroids at different orientations with respect to the image plane of the microscope, which allowed acquisition of information necessary to determine the three-dimensional structure of toroids. Furthermore, the frozen-hydrate DNA toroids prepared by this method are likely more representative of toroids in solution than the air-dried toroids of most prior EM studies. Toroids oriented coplanar to the image plane of the microscope (termed top-view toroids) exhibited circular striations (Figure 1.3), similar to those observed by Böttcher et al. (71), and were also supportive of a spool-like winding of DNA.

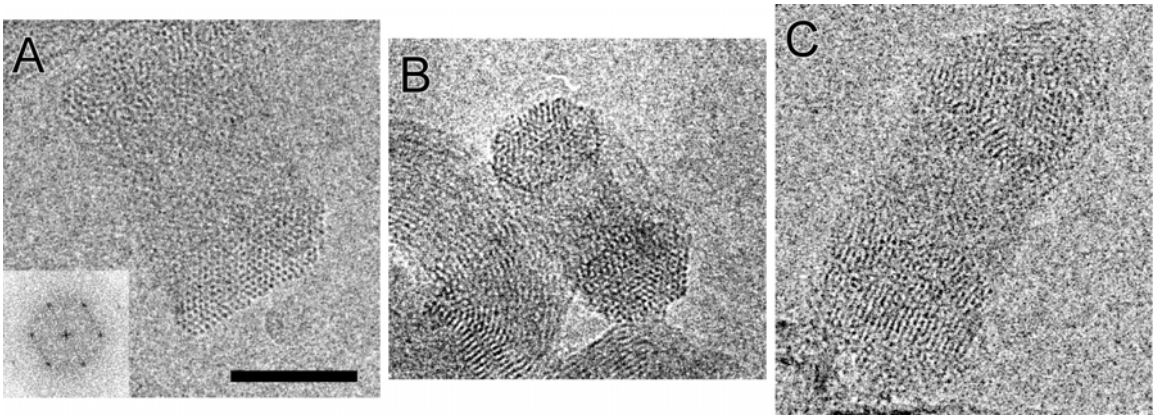

Figure 1.4 Cryoelectron micrographs of λ phage DNA toroids with the plane of the toroid oriented approximately 90° with respect to the microscope image plane (i.e. edge-view toroid images). (A) A toroid in which the hexagonal packing of DNA helices is clearly apparent in the outer regions. (*Inset*) Fourier transform of image region containing the highly ordered DNA lattice. (B) A toroid for which the outer regions are well-defined hexagons. (C) A toroid in which the outer regions appear to have DNA packed in a nonhexagonal lattice. Scale bar is 50 nm. Adapted from reference (72).

Frozen-hydrate toroids orientated perpendicular to the TEM image plane (termed edge-view toroids) proved particularly revealing of DNA packing within toroids. These images allowed for the first time the direct observation of hexagonally packed DNA in toroidal condensates (Figure 1.4). A Fourier transform of a region of an edge-view toroid micrograph that contained a highly ordered DNA lattice produced a diffraction-like

pattern typical of a hexagonal array with a Bragg spacing of $(2.4\ nm)^{-1}$ (Figure 1.4A, inset). This spacing corresponds to hexagonal packing of helices with radial spacing of 2.8 nm, as the Bragg spacing is related to the inverse of the lattice spacing by a factor of $2/\sqrt{3}$ for a hexagonal lattice. A DNA interhelical spacing of 2.8 nm is consistent with the much earlier determinations by X-ray scattering for the interhelical spacing of DNA condensed with hexammine cobalt chloride (68). On the basis of these results, it is likely that the DNA spacing reported by Böttcher et al. (71) for air-dried toroids of 1.8 nm actually corresponds to a lattice spacing 2.1 nm, which is closer to the expected value for air-dried DNA condensed by a multivalent cation, such as spermine (32,73,74).

1.3.1.2. Regions of nonhexagonal DNA packing

Böttcher et al. (71) reported that circular striations progress around air-dried toroids for up to 80% – 85% of the circumference of many toroids, but not around the entire circumference for any toroid. These authors proposed that the loss of striations for a small circumferential angle of each toroid results from regions where DNA strand packing deviates from an idealized hexagonal close-packed structure because of the presence of strand crossover points (Figure 1.5). Such crossover points are necessary if the DNA within a toroid is to have appreciable regions of hexagonal packing and contain the variations in the DNA radius of curvature that are necessary to construct a toroid from a continuous polymer (20,71). This spool-like model of Böttcher et al., with the explicit inclusion of crossovers, appears to be the only model that is consistent with both the observation of local hexagonal packing and the topological restrictions imposed by DNA being a continuous polymer.

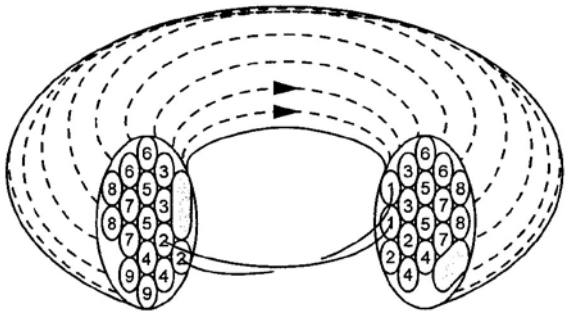

Figure 1.5 The arrangement of multiple loops of a continuous DNA molecule packed in a toroid as proposed by Böttcher et al.: Arrow heads indicate the two inner-most loops of the toroid that are hexagonally packed in the region where the arrow heads appear, but cross over within the cutaway region. To follow the topology of the crossover associated with these two specific loops, start at arrow heads and exit the hexagonal pack on the right hand side at positions numbered "1". The two loops then cross over each other (i.e. deveate from parallel, hexagonal packing) to enter the left hand side of the hexagonal pack at positions numbered "2". All successive loop pairs follow a similar pattern. Reproduced from (71); copyright American Chemical Society.

In addition to providing direct evidence of hexagonal DNA packing, the cryo-TEM images of edge-view frozen-hydrate toroids reported by Hud & Downing (72) also revealed significant variations in packing within single toroids, and also between different toroids prepared in the same condensation reaction (Figure 1.4)**.** For some toroids there are regions where DNA packing deviates significantly from a regular hexagonal lattice, yet the DNA is still packed in a regular but alternative lattice geometry (Figure 1.4C). This observation suggested that the deviation from the hexagonal array required for crossovers might not be associated with disordered DNA packing, but rather a change in the local packing lattice. As a means to investigate the origin and nature of these nonhexagonal regions of DNA packing, Hud & Downing (72) created three-dimensional computer models of toroids from which simulated cryo-TEM images were generated and compared to actual cryo-TEM images of frozen-hydrate toroids. One set of simulated toroid images was produced using a highly idealized model toroid, a model that

was constructed from closed rings of various diameters that were packed in a perfect hexagonal lattice. As expected, a simulated top-view image of the idealized toroid appeared as a series of concentric circles (Figure 1.6). An edge-view image of the same toroid appeared as two hexagonal lattices separated by a region where the DNA strands were virtually undefined (Figure 1.6). Less expected was the observation that small rotations of this idealized model toroid from approximately 5º to 45º resulted in the simulated toroid images containing two localized regions of apparent DNA order located across the center of the toroid from one another (Figure 1.6). The striations within these regions were also linear, rather than curved with the circumference of the toroid (Figure 1.6). Thus, many top-view toroids that have only two localized regions of apparent DNA order (e.g., Figure 1.3B) may simply be toroids rotated slightly with respect to the image plane of the microscope.

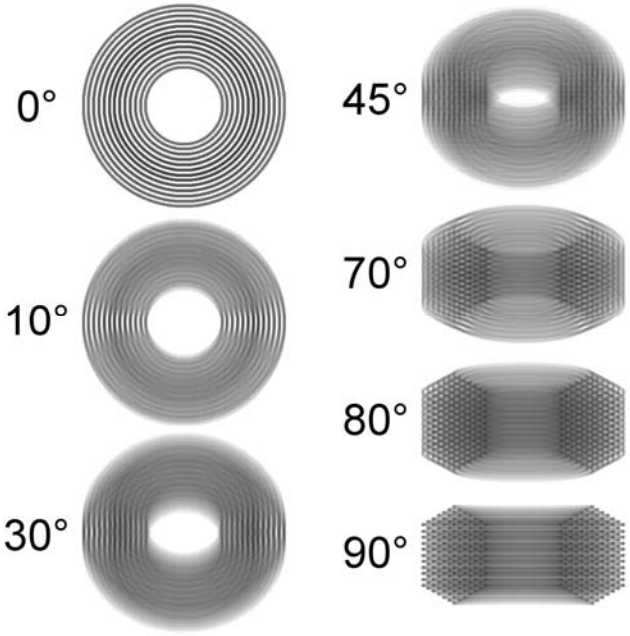

Figure 1.6 Simulated TEM images of an idealized model DNA toroid rotated at various angles with respect to the image plane. The model toroid was constructed from 179 closed circles packed in an ideal hexagonal lattice. Adapted from (72).

A physically more realistic three-dimensional model of DNA toroids was necessary to explain the observed deviations from a hexagonal lattice in edge-view images and the relationship between these deviations and the regions of apparent disorder in top-view images. This more realistic model was constructed by wrapping a semiflexible polymer into a toroid with several topological constraints (72). These constraints included (*a*) a hard-cylinder repulsive potential between polymers, (*b*) the requirement that the DNA be packed at least at one position in the toroid in a hexagonal lattice, and (*c*) the requirement that toroid growth must proceed such that each segment of DNA laid down on a growing toroid be in contact with two helices of DNA already deposited onto the toroid. In addition, DNA bending was minimized by requiring that each circumferential winding of DNA begin and end at a neighboring lattice site in the region of the toroid where the DNA was packed in an ideal hexagonal lattice. One variable that needed to be specified during the construction of physically realistic three-dimensional model toroids was the circumferential angle over which a crossover takes place between leaving and returning to the region of ideal hexagonal packing. On the basis of cryo-TEM images of top-view toroids, it was expected that the multiple crossovers within a toroid all take place within the same region of the toroid, so that there are actually two distinct regions of a toroid, the region where crossovers take place and the region where there is ideal hexagonal packing. It was not clear *a priori* how large an angle was required for these crossovers to take place. The relative size of these regions should be governed by the relative energetic penalties of deviating from a hexagonal lattice and the bending of DNA. Cryo-TEM images show limited regions of disorder, which would at first suggest that crossovers take place over a small circumferential angle.

Figure 1.7 Simulated TEM images of a model toroid constructed from a single continuous path. (*Top*) Top-view image, toroid plane is parallel to the image plane. (*Bottom*) Edge-view image, toroid plane is perpendicular to the image plane. At the nine o'clock position the top-view image DNA helices are packed in a perfect hexagonal lattice. The progression of each loop from one position in the hexagonal lattice to a neighboring position takes place over a 359º arc. Note that in the top-view image two regions exist where DNA fringe definition is lost. Also note that the DNA fringes at the nine and three o'clock positions of the top-view toroid appear similar in spacing and clarity. However, the rotation of this toroid by 90º to the edge-view reveals that the packing of DNA polymers at the three o'clock position is different from the perfect hexagonal lattice at the nine o'clock position. Adapted from (72).

However, the three-dimensional models of Hud & Downing proved otherwise. It was found that toroids in which the crossing over of DNA from one position in a hexagonal lattice to another takes place over the entire circumference of the toroid actually produced model toroids that appear well ordered in top-view images, except for two small regions (Figure 1.6). Furthermore, it was found that the size of these regions did not vary significantly upon changing the angle over which the crossovers take place. The angle between regions of apparent disorder varied linearly with the angle over which the DNA

within the toroid was allowed to deviate from an ideal hexagonal lattice structure, with the angle being approximately one half that of the angle for which deviation from an ideal hexagonal lattice was allowed. These models also revealed that the regions of apparent disorder in top-view images were not necessarily less ordered than other regions. In fact, the region of the toroid directly opposite the region with an ideal hexagonal lattice appeared in the top-view images to be as ordered as that of the hexagonal lattice (Figure 1.6). The regions in top-view toroid images that appear less ordered may be so because the local packing lattice is oriented such that from the top the density of DNA is almost uniform across this region rather than actually being disordered.

1.3.1.3. The possibility of external crossover points

In the construction of models for the wrapping of DNA into a toroid, it was assumed that DNA would not be able to feed through the hole of a toroid, which is a reasonable restriction given the hole size of a toroid and the length of λ phage DNA. However, there is no obvious reason to believe that DNA cannot crossover the outside of a toroid from one face of a toroid to the other during the course of DNA deposition. Furthermore, crossing over the outside of a toroid is topologically equivalent to a toroid flipping over during formation. The transition from adding DNA on one face of a toroid to the other would relieve superhelical strain built up in a DNA polymer during its winding onto a toroid by topologically reversing the direction of winding. A close inspection of a particularly good image of a top-view frozen-hydrate toroid shows two regions where the DNA apparently deviates from the otherwise well-defined outer border of the toroid

(Figure 1.3A). These regions may be points where the DNA has crossed back and forth between the two faces of the toroid. If so, these would represent yet one more level of fine structure for DNA packing into toroids.

1.3.2. Toroid mechanism of formation

1.3.2.1. Kinetics versus thermodynamics in toroid growth limits

Unraveling the factors that govern DNA toroid size has also proven to be a long-term research venture (13,20,75-77). A wide variety of condensing agents produce toroids approximately 100 nm in outside diameter (1,3,10,56,78-81). Furthermore, toroids of this size have been reported for DNA molecules ranging from 1 to more than 50 kb in length (13). A DNA toroid 100 nm in outside diameter with a 30-nm hole contains approximately 50 kb of DNA (56). This implies that toroids produced from DNA lengths much shorter than 50 kb contain multiple DNA molecules, whereas toroids produced from DNA around 50 kb in length can be unimolecular. The wide range of conditions and DNA lengths that produce toroids of similar size seems to imply that a 100-nm toroid represents a minimum energy state for condensed DNA (13). Accordingly, a number of researchers have sought to model toroid formation as a process under thermodynamic control that favors toroids of a particular size (13,20,77). Advancements in polyelectrolyte theory over the past several years have revealed that the attractive potential that leads to DNA condensation originates from the correlated fluctuation of counterions shared between DNA molecules at close range (42-44,46-50). Although it may now be clear why DNA condenses, it is less clear why DNA toroids grow to a

particular size. Energetic terms presented as possible limits to DNA condensate size include undercharging (i.e., build up of a net negative charge) and overcharging (i.e., build up of a net positive charge) (12,47,82-84), local defects in the packing of DNA helices (20), and kinetics of growth (21,85-89). In recent years, theoreticians have apparently reached the consensus that either under or over charging ultimately limits DNA condensate growth (49). However, despite significant advances in the theoretical treatment of DNA condensation, theoretical explanations for observed toroid dimensions have largely been developed under the assumption that toroid size is thermodynamically controlled, as opposed to being controlled by the kinetics of formation. Such thermodynamic treatments would therefore predict toroid size only when DNA condensation reaches an equilibrium state.

The distribution of toroid sizes observed within single condensation reactions had suggested for some time that toroid formation may not be under equilibrium control and that the kinetics of condensation may limit toroid growth (13,76). Furthermore, there is now considerable evidence that DNA toroid formation is a nucleation-growth phenomenon (23,76,90-92). For example, results from single-molecule studies and molecular simulations of DNA condensation are in agreement with a nucleation event being the first and rate-determining step of toroid formation (23,59,90,91,93,94). The size of particles resulting from such a process can depend on the kinetics of particle nucleation and subsequent growth. It has been appreciated for decades that particles (e.g., crystals) that form from a solution that favors rapid nucleation are generally smaller than particles formed from a solution that favors less frequent nucleation and slower growth (95). Nevertheless, experimental results had long been lacking that could help

differentiate to what degree toroid size is controlled by the kinetics versus the thermodynamics of DNA condensation.

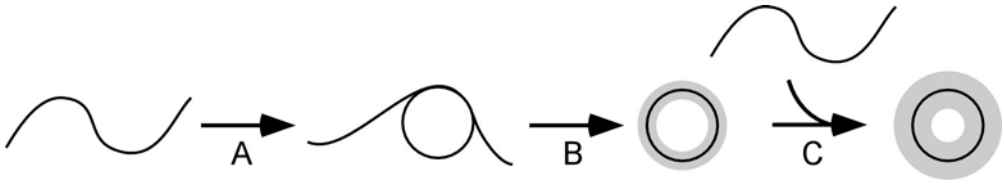

Figure 1.8 A model for the process of toroid nucleation and growth under conditions in which there is approximately equal outward and inward growth from the nucleation loop. The first step in toroid formation is the spontaneous formation of a nucleation loop (A). This loop acts as the nucleation site for condensation on which the remainder of the DNA polymer condenses to form a proto-toroid (B). The proto-toroid grows equally inward and outward by the addition of free DNA polymers from the solution (C). The black circle on the proto-toroid (structure second from right) and the fully grown toroid (right-most structure) illustrates the size of the nucleation loop. Adapted from (63).

1.3.2.2. Nucleation loop size and toroid dimensions

For an extended DNA polymer in solution with a condensing agent, intrapolymer condensation into a toroid begins when a loop forms and establishes a close contact between two regions of the DNA polymer (Figure 1.8). The appearance of this nucleation loop is expected to be a spontaneous event that results from random thermal fluctuations in DNA conformation. A recent series of experiments from the Hud laboratory have sought to determine the degree to which the nucleation loop determines toroid dimensions, and to what extent toroid thickness is governed by the kinetics of growth versus thermodynamic limits (63,96). To investigate the effects of nucleation loop size on toroid formation, DNA molecules were constructed that contained static loops that would be expected to act as "built-in" (i.e., always present) nucleation sites. For these studies, a DNA plasmid was constructed with a sequence that contained 60 A-tract sequences (e.g.,

AAAAAA) that were spaced such that their center-to-center distance along the helical axis corresponded to one helical turn of DNA in solution (96). A-tract sequences have been shown to impart a bend of approximately 12º in the helical axis B-form DNA (97). Thus, the 60 phased A-tracts of the artificial DNA sequence were designed to produce two static loops in the DNA plasmid, each with an approximate diameter of 25 nm. The inclusion of these loops was expected to reduce the size of DNA toroids, as the loops that spontaneously form along a DNA polymer in solution are on average around 50 nm in diameter (96). The static A-tract loops were also expected to enjoy a kinetic advantage over loops formed by random thermal fluctuations, under conditions in which the spontaneous formation of a nucleation loop is the rate-determining step for condensation.

Toroids produced with DNA containing the 25-nm static loops were significantly smaller than toroids produced by the same DNA plasmid, which lacked static loops (96) (Figure 1.9A,B). The toroid diameter (the average of hole diameter and outside diameter; Figure 1.10) of toroids nucleated by static A-tract loops was in excellent agreement with the expected size of the static loops (i.e., 25 nm). The thickness of toroids nucleated on the A-tract loops was virtually identical, in both mean thickness and standard deviation, to that of toroids formed without static loops under the same condensation conditions. Thus, under low salt conditions, the toroid diameter of a toroid is apparently determined by the nucleation loop of the toroid, whereas toroid thickness is determined by the conditions of condensation.

Under low salt conditions, toroid diameter and toroid thickness were uncorrelated, for both linear plasmid DNA and DNA containing static A-tract loops (63). This observation is supportive of the nucleation-growth model, in which toroid diameter is

dictated by the first loop of the toroid and toroid thickness is governed by the kinetics/thermodynamics of additional DNA deposition onto a nucleated toroid (Figure 1.8). This result also emphasizes why toroid size is probably best discussed in terms of the toroid diameter and toroid thickness (Figure 1.10) rather than outside diameter and thickness.

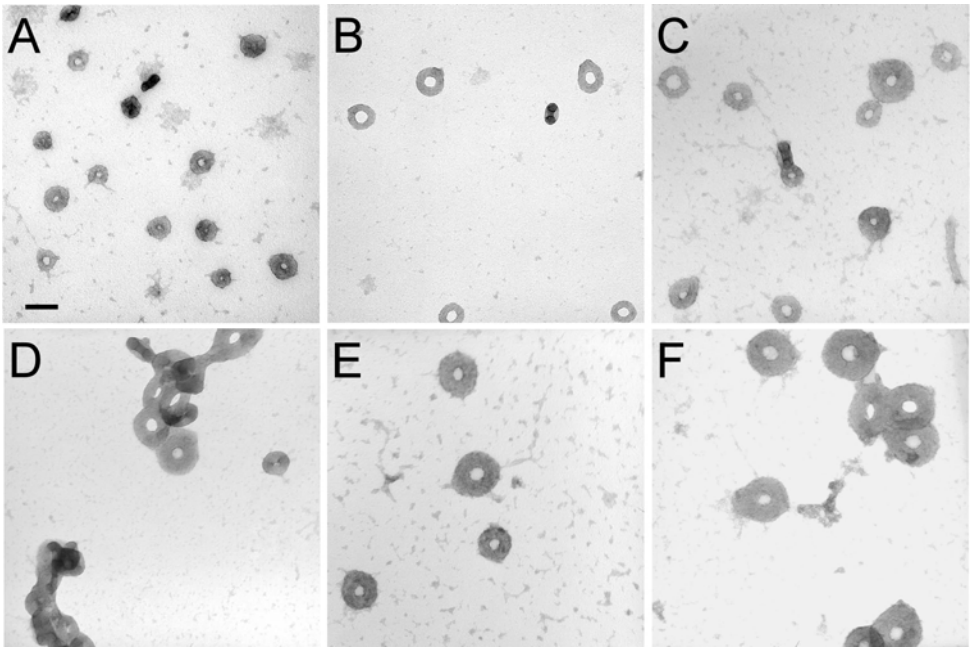

Figure 1.9 TEM images of toroids produced by the condensation of DNA by hexammine cobalt chloride. (A) *Atract60* DNA condensed from a low salt buffer. *Atract60* is a linear 3681-bp DNA with extensive sequence-directed curvature near one end. (B) *3kbDNA* condensed in a low salt buffer. *3kbDNA* is a linear 2961-bp plasmid DNA. (C) *3kbDNA* condensed from 2.5 mM NaCl. (D) *3kbDNA* condensed from 1.75 mM $MgCl_2$. (E) *3kbDNA* condensed from 3.75 mM NaCl. (F) *3kbDNA* condensed from 2.5 mM $MgCl_2$. All samples were 8.5 μg ml^{-1} in DNA and 100 μM hexammine cobalt chloride. Scale bar is 100 nm. Adapted from (63).

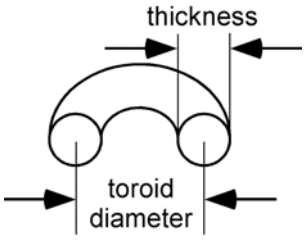

Figure 1.10 Definition of toroid diameter and toroid thickness.

1.3.2.3. Nucleation-growth kinetics as a determinant of toroid thickness

As mentioned above, toroid growth can theoretically be limited by incomplete charge compensation between DNA and condensing agents (i.e. undercharging) or by reversing the DNA charge by excessive condensate agent binding (i.e. overcharging). However, recent experiments by Conwell et al. (63) have demonstrated that, for rather typical DNA condensation reaction conditions, undercharging or overcharging do not appear to limit toroid size. It was observed that small increases in ionic strength resulted in significant changes in the size of toroids produced upon DNA condensation by hexammine cobalt chloride. For example, increasing the concentration of monovalent cations by less than 4 mM from low salt solution conditions resulted in a twofold increase in toroid dimensions (Figure 1.9). This observation implies that toroid size is not limited by undercharging. If toroids at the lower salt concentration were limited by undercharging, then an increase in the concentration of competing monovalent counterions would only increase the undercharging effect and thus decrease toroid size. Overcharging was also ruled out because the concentration of multivalent cations was not sufficient to cause charge reversal on the DNA surface (98).

The observed increase in toroid diameter with monovalent cation concentration reported by Conwell et al. (63) was accompanied with an increase in toroid thickness (Figure 1.9). The positive correlation between toroid diameter and toroid thickness at slightly elevated ionic strengths indicated a change in the mode of toroid growth with increased ionic strength, as no correlation had been observed under the low salt conditions (63). The loops that spontaneously form along DNA in solution (prior to condensation) would not be expected to increase with increasing salt, because the persistence length of DNA is not expected to increase as the ionic strength of a solution is elevated from 6.5 to 10 mM (99-101). Thus, the increase in toroid size with increased ionic strength must be due to an increase in toroid thickness (i.e., increased growth), rather than an increase in the size of the nucleation loop. Because the addition of monovalent cations would only be expected to thermodynamically suppress DNA condensation, the observation of larger toroids in the presence of higher concentrations of monvalent cations must be of a kinetic origin. A simple model for toroid nucleation and growth explained this observation (63). In the presence of increasing concentrations of monovalent cations, nucleation is suppressed because proto-toroids (i.e., toroids in the early stages of formation) are destabilized. The fewer toroids that do successfully nucleate a proto-toroid will have more DNA in solution to add during the growth phase of the toroid. This scenario is again analogous to crystal growth, where the suppression of rapid nucleation results in fewer but larger crystals.

Recent experiments involving the addition of $MgCl_2$ at different stages of DNA condensation have also shed light on the importance of nucleation in determining toroid size (102). When $MgCl_2$ was added to DNA prior to condensation with hexammine

cobalt chloride, toroids also increased in size. At 1.75 mM $MgCl_2$ toroid dimensions were similar to those of toroids produced in the presence of 3.75 mM NaCl, a comparable ionic strength (Figure 1.9E,D). A further increase in $MgCl_2$ to 2.5 mM resulted in a disproportionate increase in toroid diameter with respect to toroid thickness. This particular change in average toroid dimensions might be interpreted as resulting from an increase in the size of the loop that nucleated these toroids with respect to toroids formed at lower ionic strengths. However, the persistence length of DNA is not expected to increase with an increase in $MgCl_2$, and thus one would not expect an increase in nucleation loop size. Conwell & Hud (102) have proposed that the observed disproportionate increase in toroid diameter with increasing $MgCl_2$ concentrations results from a change in the nucleation-growth pathway of toroids. It is proposed that for sufficient concentration of $MgCl_2$, proto-toroids are destabilized to an extent that only those nucleated from larger loops (with low bending energy) go on to form full-size toroids (Figure 1.11). Because fewer toroids achieve successful nucleation, those that do are able to grow larger.

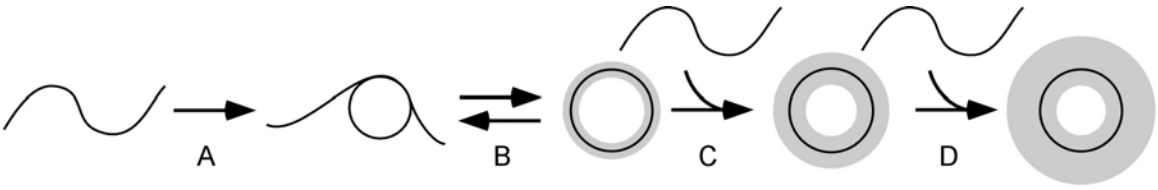

Figure 1.11 A model for the process of toroid nucleation and growth under conditions in which proto-toroids with larger nucleation loop sizes are favored during the early stage of formation. In the first step of toroid formation, a DNA polymer spontaneously forms a nucleation loop (A). The remainder of the DNA polymer condenses onto the nucleation loop to form a proto-toroid (B). At sufficient $MgCl_2$ concentrations, proto-toroids nucleated from smaller loops readily decondense, whereas those nucleated by larger loops proceed to the next step of toroid growth (C). During the last step of toroid formation, growth is preferentially outward from the nucleation loop (D). Adapted from (63).

1.3.2.4. Specific effects of divalent cations on toroid nucleation

Conwell et al. (63,102,103) have also shown that condensation of DNA by hexammine cobalt chloride in the presence of 1 mM $MgCl_2$ results in the formation of toroid clusters (Figure 1.9D). This phenomenon is not observed for toroids produced in the presence of NaCl. Furthermore, toroid clustering was not observed for DNA samples containing 2.5 mM $MgCl_2$ (Figure 1.9F). Toroid clustering appears to result from a specific effect of $MgCl_2$ on condensate nucleation. When $MgCl_2$ is associated with DNA prior to condensation, the polymers of DNA possess helix-helix contacts that are mediated by Mg(II) ions. Such contacts create a loose network of DNA polymers with both intra- and interpolymer contacts. When a condensing agent is added, such as hexammine cobalt(III), toroid nucleation within these loose networks results in the sharing of DNA polymers between toroids and thus networks of joined toroids. The disappearance of toroid clusters at higher concentrations of $MgCl_2$ can be explained by the increased competition between Mg(II) and hexammine cobalt(III) during the condensation reaction allowing the rearrangement of DNA strands from the conjoined toroids to single toroids, which are presumably more energetically favorable (102).

To confirm that the clustering of toroids by $MgCl_2$ was in fact due to the preassociation of Mg(II) with DNA, Conwell & Hud (102) also performed condensation reactions in which $MgCl_2$ was added coincident with the condensing agent hexammine cobalt chloride. This condensation protocol resulted in the production of much larger toroid-like condensates, typically over 200 nm in outside diameter (Figure 1.12). It is proposed that these condensates were able to grow much larger than toroids formed in the absence of $MgCl_2$ owing to a suppression of nucleation by a competition between Mg(II)

and hexammine cobalt(III) for association with DNA. It appears that when the same concentration of $MgCl_2$ is associated with DNA before condensation, such large toroids are not produced because the structures created by Mg(II)-stabilized DNA-DNA contacts favor the nucleation of clustered toroids over the much larger single toroid-like structures.

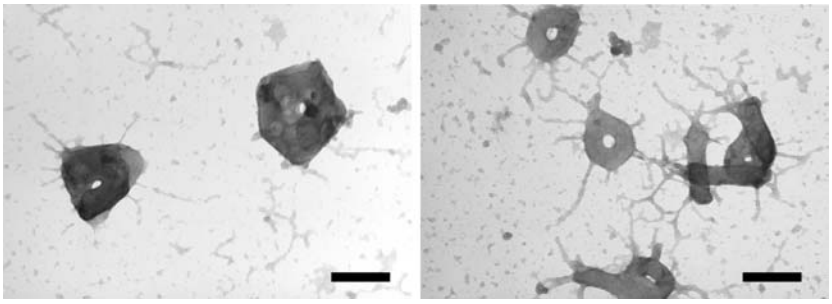

Figure 1.12 (*Left*) TEM images of DNA condensates formed at 22°C by mixing DNA with an equal volume solution of 200 μM hexammine cobalt chloride, 3.5 mM $MgCl_2$. DNA was a linearized 3-kb bacterial plasmid. DNA concentration was 10 μg ml^{-1} following mixing with the hexammine cobalt chloride, $MgCl_2$ solution. (*Right*) Same solution conditions and condensation protocol as given for left image, except carried out at 37°C. Scale bars are 200 nm. Adapted from (102).

Theoretical attempts to explain observed DNA toroid size have focused almost exclusively on the kinetics and thermodynamics of polyelectrolyte bundle growth in the presence of polyvalent counterions (12,20,21,82,83,86-89). However, in light of recent experimental results on the mechanism of DNA condensation (63,102), it is clear that any theoretical treatise presented to explain toroid size must take into account toroid nucleation rate and the rate of depletion of free DNA from solution as a potential limit to toroid growth. Thus, in addition to the necessity to understand what governs the kinetics and thermodynamic limits of polyelectrolyte bundle growth, to fully explain final toroid

dimensions requires theoretical approaches that also consider the factors governing toroid nucleation (85).

1.3.3. Are toroids ever observed at their maximum possible size?

1.3.3.1. Partially condensed DNA as an indicator of thermodynamically limited toroid growth

The experimental demonstration that nucleation and growth kinetics are a substantial, and often dominant, determinant of DNA toroid dimensions raises the question of whether toroids can actually be grown to a thermodynamic limit under conditions typically used for in vitro DNA condensation. The lack of a clear criterion for determining if a toroid has grown to a thermodynamic limit makes it challenging to demonstrate that any given toroid has not been limited by the kinetics of its nucleation and growth. Nevertheless, there are several reports of toroids with features that suggest growth to a thermodynamic limit. The large toroid-like structures of Conwell & Hud (102), produced by the coincident addition of $MgCl_2$ and hexammine cobalt chloride (Figure 1.12), represent one possible example. This possibility is suggested by the observation of a relatively small amount of partially condensed DNA protruding from these structures, which suggests condensates at the edge of stability. To test if these structures were truly at a thermodynamic limit, the same condensation protocol was repeated at 37^{o}C, which was 15^{o}C warmer than the room temperature conditions that produced the very large structures. The attractive potential between DNA molecules in the presence of multivalent cations is predicted to decrease with increasing temperature (21,42,49,51,86). If these large condensate structures were near a thermodynamic size limit, one would

predict that smaller structures would be formed at 37°C. However, if these structures were primarily limited by the kinetics of condensation, then even larger structures should appear. It was found that considerably smaller condensates were formed at 37°C (102) (Figure 1.12). Thus, it appears that the very large condensates were not kinetically limited as much as their growth was under thermodynamic control. In addition, the substantial increase in what appears to be uncondensed DNA protruding from the toroids produced at 37°C (Figure 1.12) is another indication that toroid size was thermodynamically controlled.

1.3.3.2. Very large DNA toroids

Schurr and coworkers (104) demonstrated some twenty years ago that DNA toroids 200 nm in outside diameter can be formed by dialyzing the trivalent, polyamine spermidine into a DNA solution. The DNA in these toroid preparations was initially in a low ionic strength, monovalent cation buffer, and the dialysate was 30 μM in spermidine. Schurr and coworkers reported that these very large toroids almost exclusively appeared in EM micrographs with "swirls of filamentous materials…near the outer edge of the toroids." This report of large toroids in apparent equilibrium with partially uncondensed DNA may represent the first report of DNA toroids grown to a thermodynamic limit. The use of dialysis to slowly introduce a condensing agent into a DNA solution may have allowed such large toroids to form by restricting the rate of DNA condensate nucleation. Under such conditions, the depletion of free DNA from solution might not become a limit to toroid growth before the growing toroids reach a thermodynamic size limit.

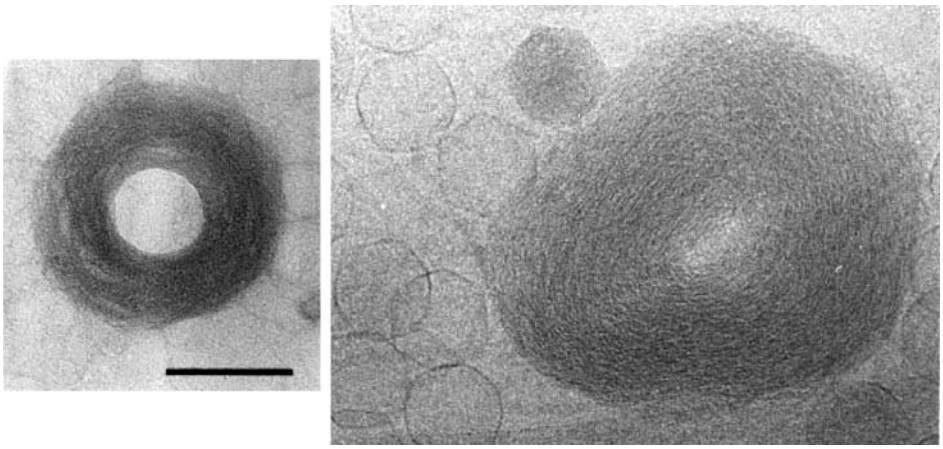

Figure 1.13 (*Left*) TEM image of a large DNA toroid produced by the condensation of T4 DNA by 6 mM spermidine in the presence of high salt (50 mM NaCl, 10 mM $MgCl_2$). Reprinted from (105), copyright American Chemical Society. (*Right*) TEM image of a large toroid formed by the release of DNA from several T5 bacteriophages into a solution containing 5 mM spermine. Empty and DNA-filled bacteriophages can be seen around the much larger DNA toroid. Both images are at the same magnification. The scale bar in the left panel corresponds to 100 nm. Reprinted from (106), copyright The National Academy of Sciences.

Yoshikawa et al. (105) have also reported the formation of very large toroids (200 nm in outside diameter) by the condensation of T4 DNA (166 kb) under conditions of relatively high concentrations of salt (50 mM NaCl, 10 mM $MgCl_2$) and spermidine (6 mM). Like the condensates of comparable size reported by Shurr and coworkers (104) and Conwell & Hud (102), Yoshikawa et al. also observed fibrous structures protruding from the surface of these larger toroids (Figure 1.13). These fibers were also interpreted by Yoshikawa et al. to be a sign of incompletely condensed DNA and DNA toroids near the edge of stability. On the basis of toroid dimensions and the length of T4 DNA, Yoshikawa et al. suggested that their giant toroids were monomolecular in T4 DNA. The hole diameters of these giant toroids were on average larger than the nucleation loop diameters expected to form along linear DNA owing to random thermal fluctuations (63).

Thus, an increase in hole diameter most likely indicates a suppression of toroid nucleation by increased ionic strength such that only proto-toroids with low bending energy (e.g., large nucleation loops) are able to successfully grow into full toroids (102). Furthermore, monomolecular toroids would indicate that each 166-kb T4 DNA molecule nucleated its own toroid. On the other hand, the fibrous structures protruding from these toroids suggest that the conditions of condensation did not favor the addition of more than one T4 DNA onto each toroid. Together these observations are consistent with the giant toroids reported by Yoshikawa et al. being limited by the thermodynamics of bundle growth, rather than by the kinetics of toroid nucleation and growth.

1.3.3.3. Bacteriophages reduce the impact of nucleation kinetics on toroid growth

Whereas the kinetics of condensate nucleation may limit DNA toroid size under most solution conditions, very large toroids that are not limited by nucleation kinetics may be accessible for a much wider range of conditions with the aid of bacteriophages. In the intriguing study by Lambert et al. (106), DNA toroids up to 300 nm in outside diameter were produced by triggering the ejection of DNA from T5 phages into a solution 5 mM in spermine, a tetravalent polyamine, and 150 mM NaCl. The toroids produced by Lambert et al. were larger than those of Schurr and coworkers (104) and Yoshikawa et al. (105), but did not exhibit any partially uncondensed DNA protruding from their surfaces (Figure 1.13). Thus, the giant toroids of Lambert et al. do not appear to have been limited by the thermodynamics of DNA bundle growth. It is possible that by temporally confining DNA within a number of bacteriophage capsids, Lambert et al. were able to decrease the rate of toroid nucleation sufficiently to grow a smaller number of very large toroids under

condensation conditions that would have resulted in a larger number of much smaller toroids if the same amount of DNA was allowed to condense from a free state in solution. While the salt and condensing agent concentrations used by Lambert et al. (106) were similar to those of Yoshikawa et al. (105), it is possible that Lambert et al. were able to grow even larger toroids without reaching the point of incomplete condensation because of their use of a tetravalent cation (i.e., spermine) rather than the trivalent cation (i.e., spermidine), as used by Yoshikawa et al.

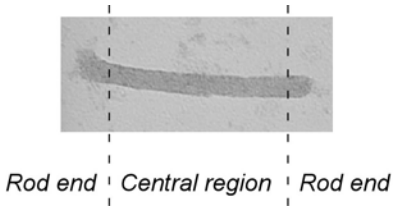

Figure 1.14 An example of rod morphology, which can be divided into three regions. Two end regions and a central region. Dashed lines have been drawn for clarity.

1.4. Rod-like DNA condensates

Rod morphology of DNA condensates (Figure 1.1B) has attracted far less attention than more commonly observed toroidal particles. Consequently, the structure and mechanism of formation of rod-like DNA condensates (also referred as *rods* throughout the text) are not as well understood.

The rod-like DNA condensates can be divided into three regions (Figure 1.14). In the central region the DNA strands are thought to be arranged in a parallel hexagonal close-pack, similarly as in the case of the toroid. In the regions at both ends, DNA strands are thought to loop back on themselves by a sharp kink to provide for a continuous growth of the rod-like condensate (62). However, there have not been detailed

experimental structural studies of rod-like DNA condensates as in the case of cryo-TEM studies of toroids discussed above (72).

In addition to structural studies, the mechanism of rod-like DNA condensates formation has been investigated extensively by theoretical means (23,59-62,85,93,107), however, experimental mechanistic studies have been lacking. Nevertheless, rods are thought to evolve by a similar mechanism as toroids (23,61,93). Rod like DNA condensate has been proposed to form by a nucleation-growth mechanism, where it is nucleated by a sharp kink in DNA backbone, and subsequent formation of a monomolecular condensate (i.e. proto-rod) (Figure 1.15). The formation of a proto-rod is then followed by its growth as free DNA molecules from the solution further stabilize the proto-rod.

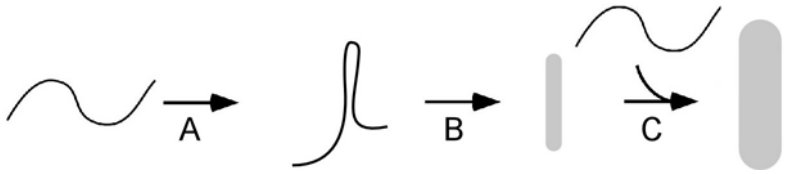

Figure 1.15 Nucleation and growth model of rod formation. (A) A formation of a sharp kink in DNA backbone. (B) Intramolecular collapse of DNA molecule to form a monomolecular proto-rod. (C) A growth of rod DNA condensate by the addition of free DNA molecules from the solution.

1.5. DNA condensation in nature

In most living organism, DNA molecule is a carrier of genetic information and has long been recognized as one of the three pillars of the central dogma in molecular biology (108). The amount of information needed for the development and life function of an organism requires extremely long genomic DNAs (Table 1-1). However, the cellular

organelle in eukaryotes responsible for storage of genomic DNA (i.e. nuclei) is too small to include genomic DNA in its extended (i.e. uncondensed) form. Thus, several DNA packing system have evolved to condense genomic DNA in organisms as simple as viruses or as complex as humans.

Table 1-1 Examples of genomic DNAs from various organisms and their respective lengths. Radius of gyration has been calculated for each genomic DNA assuming DNA persistence length of 50 nm.

Source	***Genome Length*** [m]	***Rg*** [μm]
Oryza sativa (Rice)	0.15	50
Gallus gallus (Chicken)	0.41	83
Homo sapiens (Human)	1.02	130
Fritilliaria assyriaca (Butterfly)	44.2	860

A classic example of DNA packing in nature comes from the simplest organisms. In bacteriophage heads, DNA packing represent one of the most efficient DNA packing systems *in vivo* (15). For example, a 40 000 bp long T7 phage DNA that would extend several microns in the solution is packed into its viral capsid with a diameter of only 55 nm. This results in a highly compressed and strongly bent viral DNA, forming a spool-like condensate, and storing enormous elastic energy that has been proposed to help eject bacteriophage DNA into a bacterial cell (109-111).

Condensation of the eukaryotic genome is a complex phenomenon involving a variety of proteins and biochemical processes in the cell nucleus (112-114). The structure of condensed eukaryotic DNA (e.g. morphology, size, density of packing), and the identity of DNA-associated proteins, depends on cell type as well as the stage of the cell cycle (112,113,115). In metaphase somatic cells, histones organize DNA into nucleosomes which further coil into the higher order structures of chromatin (113). Long loops of chromatin then attach to the chromosome scaffold composed of nonhistone proteins to form the chromosomes (113,114). During spermiogenesis in vertebrates, the structure of spermatid chromatin is dramatically reorganized when histones and other nonhistone-chromosomal proteins are replaced by arginine-rich oligopeptides known as protamines (116). In some vertebrate sperm cells, the replacement of histones by protamines is complete, while in others, including humans, a portion of the haploid genome remains condensed by histones (117). The DNA packaged by protamines in mature sperm cells is transcriptionally inactive and packed at a density that approaches that of a crystalline state (112,118).

2. A TIME STUDY OF DNA CONDENSATE MORPHOLOGY AND SIZE: IMPLICATIONS FOR THE EQUILIBRIUM BETWEEN TOROIDS AND RODS

2.1. Introduction

The particles that are formed by DNA and multivalent cations vary in their morphology (e.g. toroids, rods, speheres, clusters, aggregates) as well as their size. The morphology and size of DNA condensates depend on solution conditions (e.g. ionic strength, solvent polarity), properties of DNA (e.g. DNA length, persistence length, the extent of supercoiling) and properties of the condensing agent (e.g. charge density, polarity) (13,14,55-58,63,102,103,119). These variations in particle morphology and size have been used to study the mechanism of DNA condensation. Consequently, the formation of DNA condensates has been described as a nucleation and growth phenomenon (13,14,55,63,90,94,96,102,106). For example, the formation of the most commonly observed toroid morphology starts by a formation of a nucleation loop which is followed by an intramolecular collapse of the remainder of DNA molecule to form a monomolecular proto-toroid (63,96). In the final stage, the proto-toroid grows by collecting free DNA molecules from solution (63).

DNA condensate nucleation and its initial growth are thought to be complete within the millisecond time range (120). Most of the mechanistic studies have focused on these initial stages of DNA condensation reaction (63,90,94,96,102,106), even though an

additional growth and clustering of individual DNA condensates at longer reaction times have been reported (54). Theoretical studies of DNA condensation mechanism have focused on the formation of monomolecular DNA condensates (23,24,60-62,77,85,93,107,121-123). Molecular and Brownian dynamics simulations have shown that rod morphology of a monomolecular condensate represents only a metastable state which converts to thermodynamically stable toroid morphology either by internal conversion or decondensation followed by a re-collapse into a thermodynamically stable toroidal state (23,24,60,62,93). Most of the theoretical studies have thus been limited to nucleation and intramolecular collapse, and have not provided an insight into the intermolecular growth of DNA condensation mechanism.

We have studied condensation of plasmid DNA by hexammine cobalt during the first three hours of its initiation to evaluate the changes in DNA condensate properties beyond its initial nucleation and growth. By examining DNA condensates with transmission electron microscope (TEM), we were able to detect a gradual decrease in the relative rod population, and an increase in the relative toroid population. The relative populations of single toroids and rods stabilize at quasi-equlibrium values until the condensation reaction mixture reaches a true equilibrium where only clusters or aggregates are observed, if such a state remains kinetically accessible. An observation that initial toroid and rod populations are not at their quasi-equilibrium values suggests that monomolecular condensates formation is at least in part governed by the kinetics of DNA condensate nucleation. The rate of decrease in relative rod population is shown to increase with an increase in the ionic strength of the solution. However, the quasi-equlibrium relative populations of toroids and rods do not change with the increase in

ionic strength. It is proposed that the increase in the rate of morphology change reflects the increase in DNA strand exchange between rods and toroids that establishes quasi-equlibrium between the two major DNA condensate morphological forms.

In addition to the shift towards toroid morphology, we demonstrate that DNA condensates grow beyond their usually reported dimensions at longer reaction times, which is in agreement with the result of a kinetic study of Bloomfield and coworkers (54). Under our low ionic strength conditions, the changes in morphology and size of DNA condensates could not be correlated. The decrease in relative rod population to its quasi-equilibrium value is completed before an appreciable DNA condensate growth can be accurately measured by TEM. Similar to DNA condensate morphology change, DNA condensate growth rate depends on the ionic strength of the reaction mixture. Under our high ionic strength conditions, the increase in condensate size overlaps with the change in the relative toroid and rod populations. However, the condensate growth at high ionic strength does not stop after the relative toroid and rod populations reach their quasi-equilibrium values. It is concluded that the release of free DNA by dissociation of rod-like condensates is one of the factors contributing to condensate growth at high ionic strength. The results of the present kinetic study were used to propose a model of DNA condensation mechanism to account for processes observed to occur during the time frame of the reported experiments (i.e. condensate morphology conversion and growth).

The observed changes in DNA condensate morphology and size indicate that DNA condensates do not reach their equilibrium state during their initial nucleation and growth. These results have implications for further experimental and theoretical research on the collapse of polyelectrolytes with multivalent counterions. For example, any

experimental evaluation of either strictly kinetic or strictly thermodynamic models cannot use current experimental model systems where kinetic and thermodynamic factors are not both taken into account.

2.2. Experimental procedures

2.2.1. DNA preparation

2961 base pairs long Bluescript II SK- plasmid DNA (Stratagene, La Jolla, CA) was grown in DH5α cells (Life Technologies, Rockville, MD) and isolated by using the Qiagen Maxi Prep kit (Qiagen, Valencia, CA). The DNA was dissolved in 1× TE (10 mM Tris, pH 7.8, 1 mM EDTA) in the final step of isolation. The Bluescript II SK- plasmid DNA was linearized with *Hin*dIII (New England Biolabs, Beverly, MA). The linearized Bluescript II SK- plasmid DNA is referred to as *3kbDNA* throughout the text. A Bluescript II SK- plasmid was previously modified by the insertion of two tandem repeats of the multiple phased A-tract sequence 5'-ATCCATCGACC($A_6CG_3CA_6CG_2C$)$_7A_6$GCAGTGGAAG-3', which produces approximately one full loop of sequence-directed curvature (96). This A-tract-rich plasmid was grown in Sure2 Supercompetent cells (Stratagene, La Jolla, CA), isolated as described above, linearized with *Hin*dIII, and will be referred to as *3kbAtract*. To obtain a sample with shorter DNA fragment lengths, *3kbDNA* sample was digested with *BspH*I (New England Biolabs, Beverly, MA) to obtain a mixture of 0.7 kb, 1 kb, and 1.2 kb fragments (referred to as *1kbDNA*). Restriction enzyme buffers were removed from all DNA samples after digestion by rinsing at least five times with 1× TE using a Microcon YM-30 spin column (Amicon, Billerica, MA). After the final rinse, DNA samples were

eluted with 1× TE. A concentrated solution of NaCl in 1× TE was added to *3kbDNA* sample in 1× TE to obtain *3kbDNA* stock solution in a buffer with an elevated ionic strength (10 mM Tris, 7.5 mM NaCl, pH 7.8, 1 mM EDTA). All DNA samples were diluted from their stock solutions to 20 μg/ml in their respective buffers. DNA concentrations were confirmed spectrophotometrically.

2.2.2. DNA condensation

For all DNA samples, DNA condensation reaction was initiated by mixing equal volumes of DNA sample and 200 μM hexammine cobalt chloride (Sigma, St. Louis, MO) in Millipore water to yield a reaction mixture 10 μg/ml in DNA, 100 μM in hexammine cobalt chloride, and 0.5× in the respective buffer of the DNA sample. Each DNA condensate reaction was then allowed to proceed in a test tube at room temperature. 5 μl aliquots of each DNA condensation reaction were then taken out of the test tube at different incubation times (varied from zero to sixty minutes) and deposited on a carbon-coated grid (Ted Pella, Redding, CA). After 10 min incubation time on the grid, an equal volume of 2% uranyl acetate (Ted Pella, Redding, CA) was added to the condensate mixture. After 1 min staining, the grid was rinsed in 95% ethanol and air dried. The reaction time for each DNA condensation reaction was calculated by summing the incubation time in the test tube, the incubation time on the grid and the staining time. To obtain grids of DNA condensate reaction mixtures at total reaction times shorter than 11 min, DNA condensation reactions were initiated as described above, however, they were immediately deposited on the carbon-coated grids for varying incubation times on the grid (varied from one to ten minutes) after which an equal volume of 2% uranyl acetate

was added. The uranyl acetate staining was stopped after 1 min by rinsing the grid in 95% ethanol and air dried. The reaction time for this set of reaction mixtures was calculated by summing the incubation time on the grid and the staining time.

2.2.3. DNA condensate imaging

All the carbon-coated grids were examined with a JEOL-100C transmission electron microscope (TEM). The relative toroid and rod populations in each sample were determined by counting the number of unclustered toroids and rods. The minimum number of total DNA condensates counted for each grid was 500. Finally, images of DNA condensates were recorded on film at 100,000× magnification. TEM negatives were scanned at 300 dpi into an electronic format, and a graphics program was used to measure the size of individual DNA toroids in each sample.

2.3. Results and discussion

2.3.1. Relative rod population decreases with reaction time

We have performed a time study of DNA condensate morphology in the solutions obtained by mixing plasmid DNA with hexammine cobalt as a condensing agent. In the presence of hexammine cobalt, plasmid DNA condenses into several morphologically distinct forms such as toroids, rods, spheres, clusters and morphologically less defined aggregates (13,14,43,56,57,124,125). Toroids and rods have been reported to be the two most prevalent morphological forms with the other forms accounting for less than 1% each. Thus, all the statistics on DNA condensate morphology measured in this study have

been obtained by counting only single (i.e. unclustered) toroids and rods. Toroid and rod populations are reported in terms of the percentage of all counted unclustered particles.

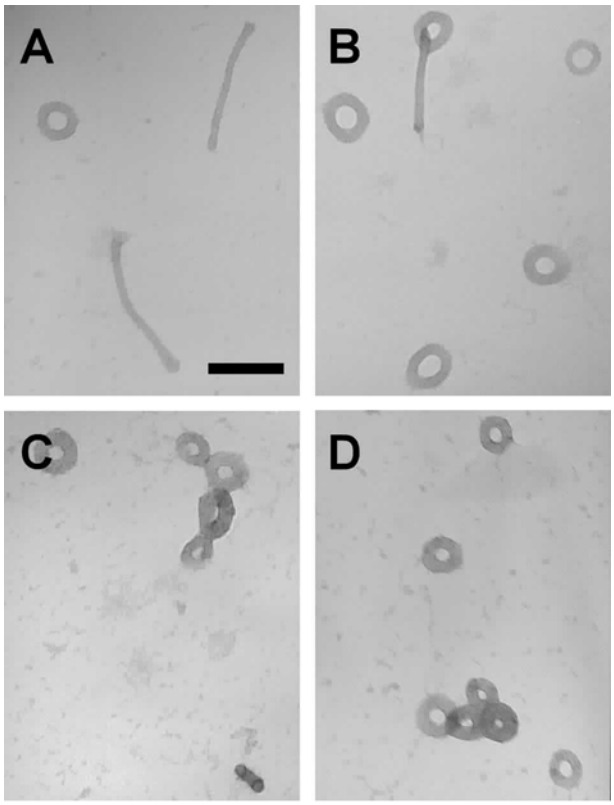

Figure 2.1 Rod population in DNA condensation reaction mixture decreases with reaction time. DNA condensation mixture was prepared by mixing equal volumes of 20 μg/ml *3kbDNA* in 1× TE (10mM Tris, 1mM EDTA, pH 7.8) and 200 μM hexammine cobalt in Millipore water. The condensate morphology at different times was evaluated by transmission electron microscopy (TEM). (A) 2 min reaction time. (B) 16 min reaction time. (C) 41 min reaction time. (D) 71 min reaction time. The scale bar in panel A represents 100 nm.

Linear 2961 base pairs long plasmid DNA (*3kbDNA*) was first condensed at room temperature with hexammine cobalt in a low ionic strength buffer (5 mM Tris, pH 7.8, 0.5 mM EDTA) with the final DNA and hexammine cobalt concentrations equal to 10 μg/ml and 100 μM, respectively. DNA condensates in the reaction mixture were examined for their morphology at different reaction times by visualizing them with

transmission electron microscopy (TEM) (Experimental procedures). After 2 min reaction time, toroids as well as rods were observed (Figure 2.1A) with toroids and rods accounting for 79% and 21% of all single DNA condensates, respectively (498 toroids, 136 rods) (Figure 2.2). Increasing reaction time to 16 min, the toroid to rod morphology ratio changed in favor of toroids (Figure 2.1B), where toroids and rods represented 87% and 13% of all the counted DNA condensates, respectively (622 toroids, 98 rods) (Figure 2.2). A further increase in the reaction time to 41 min produced a sample where toroids constituted a vast majority of the particles (Figure 2.1C), with the relative toroid and rod populations 97% and 3%, respectively (606 toroids, 22 rods) (Figure 2.2). An additional increase in reaction time to 71 min did not produce any further change in DNA condensate morphology (Figure 2.1D), where toroids and rods still represented 97% and 3% of total DNA condensates, respectively (602 toroids, 20 rods) (Figure 2.2). The relative toroid and rod populations remained unchanged even after 3 h reaction time (data not shown). At reaction times longer than 41 min (Figures 2.1C-D), clustering of toroids and rods was observed to occur more often compared to the samples obtained at shorter reaction times (Figures 2.1A-B). Similarly, as in the case of unclustered DNA condensates, an investigation of relative toroid and rod populations within clusters in the sample of condensed *3kbDNA* reveals a steady decrease in relative rod population in clusters of DNA condensates. After 2 min reaction time rods represented 10% of all clustered DNA condensates, whereas after 71 min rods accounted for 2% of all clustered particles.

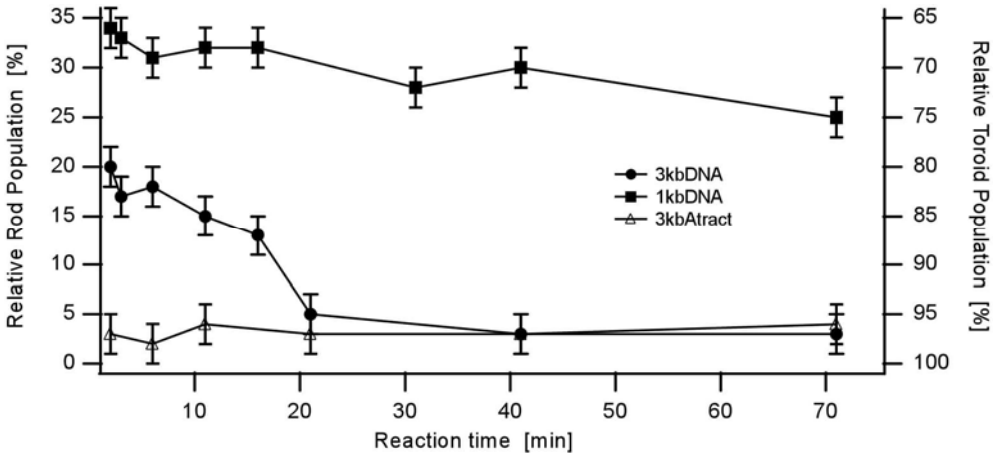

Figure 2.2 Relative rod and toroid populations depend on the reaction time as well as properties of DNA molecules. All DNA condensation reactions were initiated as described in the caption to Figure 2.1. *3kbDNA* is a 2961 base pairs long linearized plasmid DNA. *1kbDNA* is a mixture of short DNA fragments with an average fragment length of 1000 base pairs. *1kbDNA* was obtained with restriction digest of *3kbDNA* (Experimental procedures). *3kbAtract* is 3309 base pairs long linearized plasmid DNA obtained by modifying *3kbDNA* (Experimental procedures).

DNA length has been shown to affect relative toroid and rod populations (55,56). In the samples containing DNA fragments shorter than 1500 base pairs, relative toroid population decreases with relative rod population increasing (55,56). To investigate the effect of reaction time on the relative toroid and rod populations in a sample of short DNA fragments, a time study of DNA morphology in a sample of condensed *1kbDNA* (Experimental procedures) was performed. *1kbDNA* was condensed by hexammine cobalt in a low ionic strength buffer as described above for *3kbDNA*. In agreement with previously published data, the relative toroid population in the solution of condensed *1kbDNA* was consistently lower than in *3kbDNA* sample regardless of the reaction time (Figure 2.2). Furthermore, similarly as in the case of *3kbDNA*, the relative toroid population in *1kbDNA* sample increased with reaction time (Figure 2.2). However, the change in the relative toroid and rod populations was much less pronounced as compared

to what is observed with *3kbDNA* (Figure 2.2). As the reaction time was increased from 2 min to 71 min, the relative toroid population in the sample of condensed *1kbDNA* increased from 66% to 72%, and was accompanied by a decrease in the relative rod population from 34% to 28% (Figure 2.2). Finally, an increase in the reaction time to 3 h did not further change toroid to rod morphology ratio (data not shown).

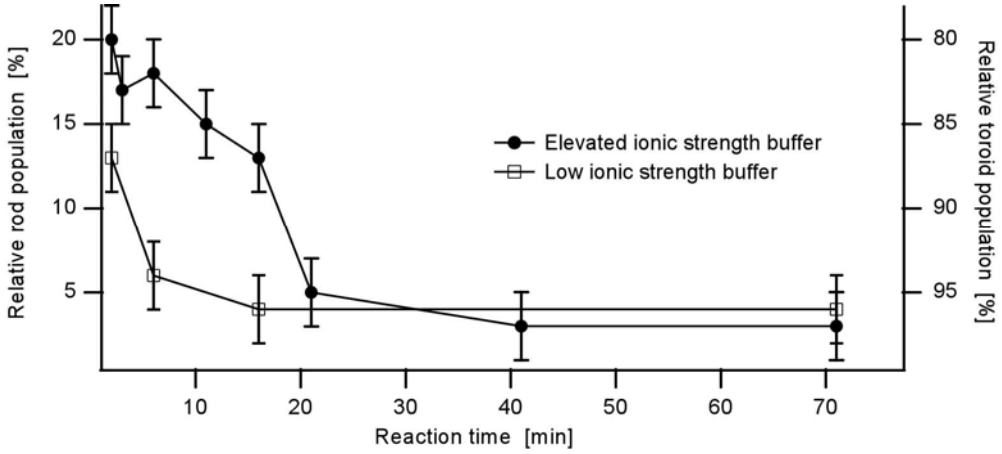

Figure 2.3 The rate the relative rod population decrease depends on the ionic strength of the solution. DNA condensate reaction mixtures were prepared as described in the caption to Figure 2.1. *3kbDNA* was prepared in two different buffers and condensed with hexammine cobalt. The low ionic strength buffer (10 mM Tris, 1mM EDTA, pH 7.8) had a nominal ionic strength of 13 mM. The high ionic strength buffer (10 mM Tris, 7.5 mM NaCl, 1 mM EDTA, pH 7.8) had a nominal ionic strength of 20.5 mM. The final ionic strengths after condensation of *3kbDNA* in the first and second solution were 6.5 mM and 10.25 mM, respectively.

2.3.2. An effect of the ionic strength on condensate morphology

It has been reported previously that thickness of toroid and rods is the same, which led some to suggest that rods convert to toroids by internal looping that results in a fusion of the two ends of the rod. However, the structure of toroids at longer reaction times does not show any indication of the presence of fused rod ends. An alternative mechanism of

rod to toroid conversion could proceed through rod dissociation. The released free DNA would then be able to nucleate more stable toroid morphology or contribute to the growth of the pre-existing toroids. The rate of rod-like condensate dissociation should increase with the ionic strength of the solution due to the electrostatic nature of the interactions stabilizing DNA condensates. An increase in dissociation rate would result in an increase in the rate of rod to toroid morphology shift.

To investigate DNA condensation morphology under an elevated ionic strength conditions, *3kbDNA* was condensed with hexammine cobalt in a high ionic strength buffer (5 mM Tris, 3.75 mM NaCl, 0.5 mM EDTA, pH 7.8) and investigated with TEM (Experimental procedures). The relative toroid population increased from 87% at 2 min reaction time to 96% at 71 min reaction time (Figure 2.3). Independent of the reaction time, the condensation reaction in high ionic strength buffer yielded a sample in which the relative rod population was always smaller than in the low ionic strength buffer (Figure 2.3). Furthermore, the relative rod population in the sample of *3kbDNA* condensates in the high ionic strength buffer stabilizes at earlier reaction times compared to the solution of *3kbDNA* condensates in the low ionic strength buffer (Figure 2.3).

2.3.3. Static DNA loops also affect the rate of rod to toroid morphology conversion

DNA static loops in DNA molecules have been shown to represent a built-in toroid nucleation sites (63,96). Static DNA loops thus represent a kinetic advantage for toroid nucleation.

A static DNA loop can be introduced into a double stranded DNA by incorporation of multiple A-tract sequences (96), which are sequences of four to six A·T

base pairs that create a static bend in the DNA helical axis of approximately 13° per A-tract sequence element (97,126). If A-tract sequences are phased along a DNA molecule with respect to the helical twist of B-form DNA, an accumulative amount of static curvature can be produced. A 3.3 kb DNA plasmid containing static curvature of approximately 360° (i.e. one complete static A-tract loop) over a sequence of 346 bp (i.e. a 37 nm diameter loop) was digested with the restriction enzyme *Hin*dIII so that the static loop was located near one end of the linearized plasmid (*3kbAtract*). *3kbAtract* was condensed with hexammine cobalt in a low ionic strength buffer as described above for *3kbDNA*. After 2 min reaction time, toroids accounted for 97% of all counted single condensates with rods representing the remaining 3% (Figure 2.2), which represented a considerable increase in the initial relative toroid population compared to *3kbDNA* sample, which did not contain static DNA loops (Figure 2.2). This is consistent with the observation that static DNA loops favor toroid formation by offering kinetic advantage for toroid nucleation.

Alternatively, if toroids nucleated by static DNA loops are kinetic traps, the value at which the relative toroid population stabilizes should be higher than the one observed in the absence of static DNA loops (i.e. in the sample of condensed *3kbDNA*). However, an investigation of relative toroid and rod populations in the sample of condensed *3kbAtract* at different reaction times shows that relative toroid population in a *3kbAtract* sample stabilizes at the same value as that observed for a *3kbDNA* sample (Figure 2.2). This result excludes the possibility that the presence of static DNA loops acts as a kinetic trap for toroid morphology.

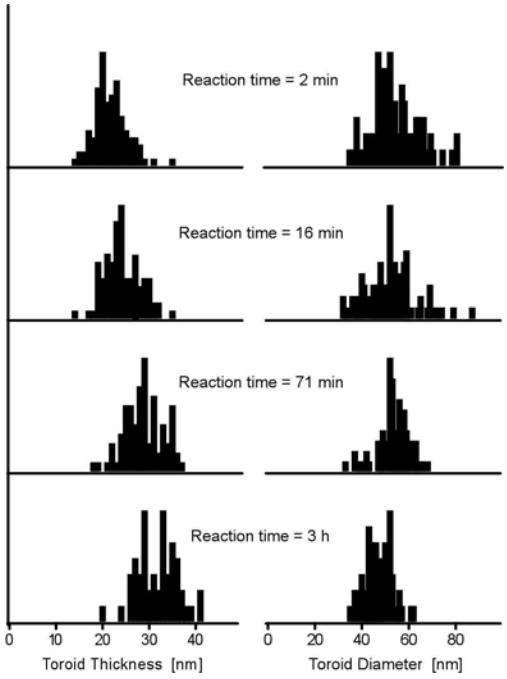

Figure 2.4 Histograms of toroid thickness and average diameter in sample of condensed *3kbDNA* at low ionic strength buffer at different reaction times. For each toroid thickness histogram, the reaction time is indicated to the right. For each toroid average diameter histogram, the reaction time is indicated to the left of the histogram.

2.3.4. DNA condensate growth at low and elevated ionic strengths

The dissociation of rod-like condensates results in the release of free DNA into the solution. As suggested above, released DNA can either nucleate a new condensate or contribute to the growth of a preformed condensate. The fate of released DNA can be investigated by measuring condensate size as a function of reaction time. If free DNA predominately nucleates new condensates, then condensate size distribution should not change with reaction time. On the other hand, if free DNA adds on to pre-existing condensates, then an increase in average condensate size should be observed. Toroid and rod sizes cannot be described in terms of the same dimensions.

Toroid size has been analyzed in the context of several different parameters such as toroid thickness as well as outside, average and inner hole diameter. Rod condensate sizes are usually reported in terms of their length and thickness. However, it has been shown recently that toroid thickness and average diameter (Figure 1.10) are especially useful in analyzing DNA condensate growth.

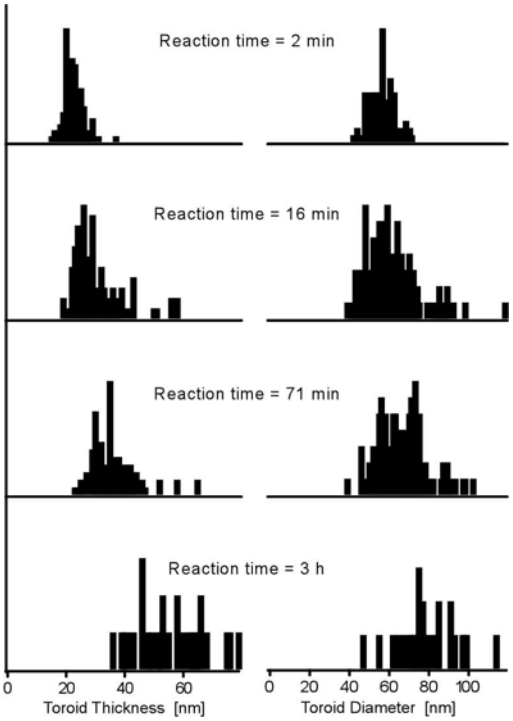

Figure 2.5 Histograms of toroid thickness and average diameter in a sample of condensed 3kbDNA in a high ionic strength buffer at different reaction times. For each toroid thickness histogram, the reaction time is indicated to the right. For each toroid average diameter histogram, the reaction time is indicated to the left of the histogram.

We have analyzed the temporal dependence of toroid thickness and diameter in a sample of *3kbDNA* condensed with hexammine cobalt in a low ionic strength buffer. The mean toroid thickness after 2 min and 16 min reaction time were measured to be 22 ± 4 nm and 25 ± 4 nm, respectively. The increase in mean toroid thickness observed between

2 min and 16 min reaction time did not represent a statistically significant change under the low ionic strength conditions (Figure 2.4). A statistically significant increase in toroid thickness was observed only after 71 min reaction time (Figure 2.4), when the mean toroid thickness increased to 29 ± 4 nm. Finally, a minor increase was observed after 3 h reaction time with the mean toroid thickness rising to 32 ± 4 nm. Toroid diameter did not change appreciably during the time frame of this study (Figure 2.4). After 2 min, 16 min, 71 min, and 3 h reaction time the mean toroid diameter was measured to be 55 ± 12 nm, 53 ± 12 nm, and 54 ± 7 nm, 48 ± 6 nm, respectively.

A temporal dependence of toroid dimensions in a sample of condensed *3kbDNA* in the high ionic strength buffer was investigated next. Under these conditions, the increase in toroid dimensions became apparent at shorter reaction times compared to the low ionic strength conditions (Figure 2.5). After 2 min reaction time, toroid seemed to be of uniform dimensions, whereas after 16 min and 71 min reaction time, the relative amount of appreciably bigger toroids progressively increased (Figure 2.5). The mean toroid thickness after 2 min reaction time was measured to be 23 ± 4 nm. After 16 min reaction time, the mean toroid thickness increased significantly to 31 ± 9 nm, and further increased to 36 ± 8 nm after 71 min reaction time. A dramatic increase in toroid thickness of *3kbDNA* toroids in the high ionic strength buffer was observed after 3 h reaction time with mean toroid thickness measured to be 57 ± 12 nm. In spite of statistically significant increase in the mean toroid thickness, it can be seen from the histograms in Figures 2.6 that a considerable population of thinner toroids still remained even at the reaction time of 71 min. The mean toroid diameters after 2 min, 16 min, 71 min, and 3 h were measured to be 58 ± 7 nm, 62 ± 13 nm, 66 ± 12 nm, 80 ± 14 nm respectively. Similarly as

in the case of toroid thickness in the high ionic strength buffer, a significant population with a higher toroid diameter starts to evolve after 16 min reaction time (Figure 2.5), even though the mean toroid diameter does not change significantly during the first 71 min of condensation reaction (Figure 2.5).

Rod condensate growth shows a similar behavior in the low and high ionic strength buffers. However, due to a much lower relative rod population, the number of rods analyzed for their dimensions never exceeded 30. Thus, we only report the mean lengths and thicknesses and do not present the data in the form of histograms. In the low ionic strength buffer, the mean rod thickness during the first 21 min of condensation reaction did not change significantly. Mean rod thickness after 2 min and 21 min was 18 ± 3 nm and 20 ± 5 nm, respectively. The decrease in relative rod population to 3% prevented a determination of mean rod thickness at reaction times longer than 21 min. Nevertheless, a representative TEM images in Figure 2.6 clearly indicate a considerable increase in rod thickness after 21 min reaction time. In contrast to rod thickness, rod length in the low ionic strength buffer did not change appreciably during the time frame of this study, with all the rod length distributions statistically indistinguishable from each other.

The rods observed in the high ionic strength buffer were observed to be thicker than rods obtained in the low ionic strength buffer. The mean rod thickness after 2 min and 16 min reaction time were measured to be 19 ± 3 nm and 34 ± 12 nm, respectively, which represented a statistically significant increase in rod dimensions. The thickness of rod condensates continued to increase after 16 min reaction time (Figure 2.7). Similar to the results from the low ionic strength buffer experiments, rod length in the high ionic

strength buffer did not change during the time frame of this study with an average rod length after 2 min and 16 min reaction time 248 ± 63 nm and 259 ± 62 nm, respectively.

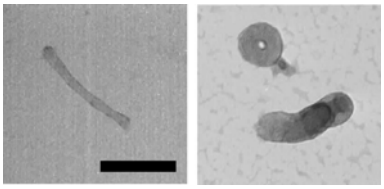

Figure 2.6 Rod grow thicker in the low ionic strength buffer even after 21 min reaction time, when morphology ratio stabilizes at its quasi-equilibrium value. (A) A TEM image of a representative rod obtained after 21 min reaction time. (B) A TEM image of a representative rod obtained after 3 h reaction time. The scale bar in panel A represents 100 nm.

2.3.5. Relative stabilities of toroid and rod morphologies

Toroids and rods are the two most commonly observed morphological forms in solutions of condensed plasmid DNA (13,14). Under typical DNA condensation conditions (i.e. DNA longer than 2000 base pairs, aqueous buffers), it has been reported that toroid and rod morphologies coexist, but with toroids representing the majority of the particles (55-57,63). Our analysis of DNA condensate morphology in the samples of condensed *3kbDNA* has also revealed that toroids account for the majority of particles regardless of reaction time (Figure 2.2). Relative rod population never exceeded 20% of all the condensates counted (Figure 2.2). This is the first report to our knowledge that relative toroid and rod populations in a sample of condensed DNA did not remain constant with reaction time (Figure 2.2). The relative rod population in the sample of condensed *3kbDNA* decreased from 20% at the shortest reaction time to 3% at the longest reaction time of this study (Figure 2.2). A decrease in the relative rod population was observed in

the sample of *1kbDNA*, however, this decrease was not as pronounced as in the case of *3kbDNA* (Figure 2.2).

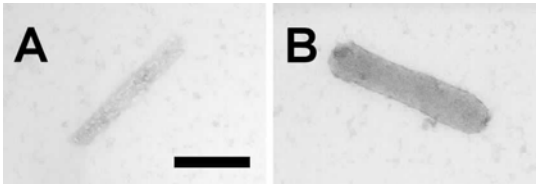

Figure 2.7 Rod thickness in the high ionic strength buffer increases further after the morphology ratio reaches its quasi equilibrium value at 16 min reaction time. (A) A TEM image of a representative rod obtained after 16 min reaction time. (B) A TEM image of a representative rod obtained after 3 h reaction time.

The gradual decrease in relative rod population and concurrent increase in relative toroid population in the solutions of condensed *3kbDNA* and *1kbDNA* suggest that toroids are the thermodynamically favored DNA condensate morphology. However, the rod condensates observed in the sample of condensed *3kbDNA* and *1kbDNA* do not completely disappear from the reaction mixture even after the longest reaction time. Instead, relative rod population in *3kbDNA* sample is maintained constant at 3% ± 2% after initial decrease during the first 40 min of the reaction. In the sample of condensed *1kbDNA*, relative rod populations stabilize at 28% ± 3%. This suggests that both rods and toroids represent equilibrium morphologies with their populations being determined by their relative thermodynamic stabilities. This finding is in contrast to theoretical predictions of toroid as the thermodynamically favored state of a condensed semi-flexible polyelectrolyte such as DNA with rod representing only a metastable state (23,24,60-62,77,85,93,107,121-123). It should be noted that majority of these theoretical studies have considered only a collapse of a single polyelectrolyte chain. Thus, even though an

isolated monomolecular rod condensate could represent a true metastable state that eventually converts to a thermodynamically favored toroidal conformation, a growth of a monomolecular proto-rod in a solution with available free DNA can be kinetically stable enough to prevent the complete conversion of proto-rods into proto-toroids.

Even though the thermodynamic stability of toroid and rod morphologies increases with the growth of condensates, the progressive clustering of individual condensates at reaction times longer than 41 min (Figures 2.1C-D) suggests that neither single toroids nor single rods represent the global thermodynamic minimum of DNA condensates obtained with hexammine cobalt. If the condensation reaction is allowed to proceed in the low ionic strength buffer for 1 day, only large clusters and aggregates can be observed under TEM with no single toroids or rods detected (data not shown). This suggests that single toroids and rods do not represent an equilibrium state of DNA condensates under our solution conditions. Consequently, the relative toroid and rod populations at reaction times longer than 41 min must then represent quasi-equilibrium values.

2.3.6. Stability of rods and the kinetics of DNA condensation

The observed decrease in rod morphology with reaction time (Figures 2.2, 2.3) clearly shows that, initially, toroid and rod populations are not determined exclusively by the equilibrium thermodynamics of DNA condensation. If that was the case, the relative toroid and rod populations should remain constant. Instead, the relative rod population decreases with time, suggesting that both the kinetics and thermodynamics of DNA

condensate nucleation and growth must play a role in determining the quasi-equilibrium populations of both morphologies.

A metastable proto-rod increases its stability by the addition of free DNA molecules that provide additional interstrand contacts. The resulting multimolecular rod can then attain its thermodynamic stability by collecting a critical number of free DNA molecules. The final relative rod population at which multimolecular rods reach their quasi-equilibrium stability could depend on several kinetic factors. In particular, an increase in the number of proto-rods compared to the number of proto-toroids that initially form in the condensation reaction should result in an increase in the final relative rod population. Also, an increase in rod growth rate should also increase the final relative rod population.

The rod condensates in *3kbDNA* samples reach their stable relative populations at 3% ± 2% whereas in *1kbDNA* samples the relative rod population stabilizes at 28% ± 3% (Figure 2.2). A higher final relative rod population in the solution of condensed *1kbDNA* could be due to a higher initial proto-rod population compared to the *3kbDNA* sample, which would implicate an important role of proto-rod and proto-toroid stabilities in determining the final relative rod population. If the final relative rod population was indeed dependent only on the initial proto-rod and proto-toroid stabilities, a decrease in the quasi-equilibrium relative rod population should be observed in the samples with increased ability to form proto-toroids. However, a comparison of the final relative rod populations in the samples of condensed *3kbDNA* and *3kbAtract* contradicts this conclusion. The final relative rod populations in *3kbDNA* and *3kbAtract* samples were

statistically indistinguishable even though the proto-toroids in *3kbAtract* are kinetically favored over proto-rods due to a presence of the static nucleation loops.

2.3.7. Relative rod population decreases due to rod dissociation

The temporal decrease in the relative population of individual rods in the samples of condensed *3kbDNA* and *1kbDNA* (Figure 2.2) could suggest that rods have simply a higher propensity to form clusters. If rods exhibited a higher probability to cluster, the decrease in relative rod population should be accompanied by a concurrent increase in the relative rod population within clusters of DNA condensates. However, an investigation of toroid to rod morphology ratio within clusters in the sample of *3kbDNA* reveals a steady decrease in relative rod population. The observed decrease in the population of clustered rods with reaction time excludes the possibility that a decrease in the relative rod population is due to their higher tendency to cluster. The decrease in the relative rod population with reaction time could, alternatively, imply that rods simply dissociate to release free DNA into solution that could then form thermodynamically more stable toroids or further stabilize pre-existing toroids.

The attraction forces that stabilize the condensed particles of like-charged DNA strands have been proposed to arise from correlated fluctuations of DNA-bound multivalent counterions (26,30,37,42-47,49,50). The strength of these attraction forces has been shown to depend on the multivalent counterion local concentration at the surface of DNA, which decreases with increasing concentrations of competing counterions (29,42,43,98,127). The apparent higher rate of relative rod population decrease in the high ionic strength buffer (Figure 2.3) could therefore suggest that the

decrease in relative rod population could be due to a gradual dissociation of thermodynamically less favored rods to release free DNA into the solution. This conclusion relies on the assumption that the probabilities for toroid and rod nucleation in the high ionic strength buffer are equal to the respective nucleation probabilities in the low ionic strength buffer of this study. These probabilities are determined by the *j*-factor which has been shown to depend on the persistence length of DNA molecule and the number of possible conformations that lead to a nucleation structure (76,128,129). At constant DNA length, the *j*-factor would not be expected to change since the persistence length has been shown to remain constant within the ionic strength range of this study (99-101,130). Consequently, the probabilities to nucleate toroids and rods in the low and high ionic strength buffers are not expected to be appreciably different which would suggest the same rates of toroid and rod nucleation under the different ionic strength conditions of this study.

2.3.8. Toroid growth mechanism depends on the ionic strength

Free DNA that is released upon rod dissociation could either nucleate thermodynamically more stable toroids or provide for further growth of already formed condensates. Even though a considerable increase in toroid thickness and diameter was detected in the low ionic strength buffer (Figures 2.4), toroid growth did not correlate with the decrease in relative rod population. In the low ionic strength buffer, a statistically significant toroid growth was measured only after the rods reached their quasi-equilibrium relative population (Figure 2.8A). This suggests that DNA that is released upon rod dissociation would nucleate new toroids. Toroid growth that becomes appreciable later in

condensation reaction would then alternatively proceed by DNA strand exchange between individual toroid. However, even if all DNA released by rod dissociation deposited on pre-existing toroids, the resulting increase in toroid thickness would be too small to detect it with TEM. For example, assuming a hexagonal close pack of DNA strands in both toroids and rods, a 17% decrease in relative rod population observed in the low ionic strength buffer would result on average in an approximately 1 nm increase in toroid thickness. It is therefore impossible to conclude based on the toroid size measurements alone whether DNA molecules, released by rod dissociation, nucleate new condensates or add onto pre-existing ones.

The observed increase in toroid dimensions that accompanies the decrease in relative rod population in the high ionic strength buffer (Figure 2.5) is considerably higher than would be expected if only DNA released by rod dissociation contributed to the growth of the remaining condensates (Figure 2.8B). It is therefore suggested that the condensate growth mechanisms must be different in the low and high ionic strength buffers. This is in agreement with the results published by Conwell et al., where they propose two distinct mechanisms of toroid formation for low and high ionic strength conditions (63). However, the origin of the observed differences is not clear, and is likely a combination of kinetic and thermodynamic factors.

It has been shown by Conwell et al. that toroid thickness and toroid diameter (Figure 1.10) can be used to analyze the process of toroid formation (63). To analyze the mechanism of toroid growth, a relationship between toroid thickness and diameter was investigated for each sample of condensed *3kbDNA*. Specifically, the slope of a linear fit of toroid diameter versus toroid thickness data can be used to distinguish between

different modes of toroid growth. A zero slope is indicative of toroid formation with an equal outward and inward growth from the nucleation loop (Figure 1.8) (63). On the other hand, a non-zero positive slope indicates a toroid formation with a preferential outward growth in the later stages of DNA condensation (63).

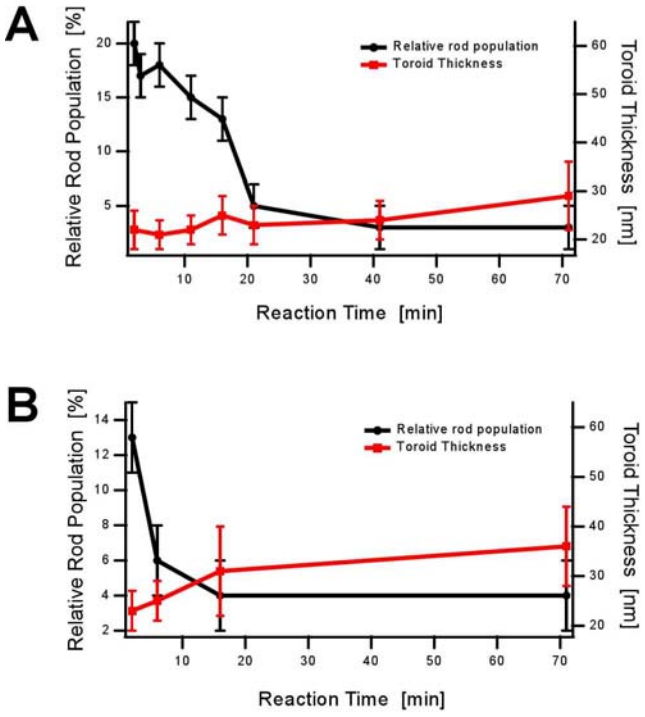

Figure 2.8 A temporal change in morphology of DNA condensates is not correlated with their growth. For low and high ionic strength buffers, relative rod population is plotted to indicate the time frame of DNA condensate morphology change, whereas toroid thickness is plotted to indicate the time frame of DNA condensate growth as detected by TEM. (A) In the low ionic strength buffer, the transition to quasi-equilibrium relative rod population is reached before any statistically significant DNA condensate growth is observed. (B) Similarly, in the high ionic strength buffer, the morphology transition is finished before appreciable DNA condensate growth can be observed.

During the first 71 min of a condensation reaction, toroid thickness and diameter of unclustered toroids of condensed *3kbDNA* in a low ionic strength buffer are not correlated as revealed by the zero slope of rms best-linear fit of toroid thickness and

toroid diameter (Insert of Figure 2.9A). As proposed by Conwell et al., this indicates a toroid growth mechanism in which there is an equal growth inwards and outwards form the nucleation loop (Figure 1.8) (63). The size measurements of unclustered toroids at 3h reaction time exhibit slight correlation indicated by a non-zero slope of the linear best-fit, which suggests a change in toroid growth mechanism. However, a slope of 0.6 for a data set of condensed *3kbDNA* at 3 h reaction time could also be due to a systematic bias that could have been introduced during the toroid size measurements. In the present study, only toroids with a clearly defined hole were measured. A substantial amount of toroids of condensed *3kbDNA* in the low ionic strength buffer grow thick enough after 3 h reaction time to obscure their hole. The exclusion of these particles could have artificially increased the slope of the linear best fit.

Unclustered toroids in the sample of condensed *3kbDNA* in the high ionic strength buffer behave quite differently. Initially, toroid thickness and diameter are not correlated as shown by the zero slope of the linear best-fit at 2 min reaction time (Figure 2.9B). As in the case of *3kbDNA* condensates in the low ionic strength buffer, this is consistent with toroids growing equally outwards and inwards from the nucleation loop (Figure 1.8). If the condensation reaction is allowed to proceed for reaction times longer than 2 min, a correlation between toroid thickness and diameter in the buffer of high ionic strength becomes apparent (Figure 2.9B). Regardless of the reaction time, toroids in the high ionic strength buffer had clearly defined inner holes, which implies that a positive non-zero slope at reaction times longer than 16 min is not an artifact of the systematic bias, which is possible for the data set obtained at 3 h reaction time in the low ionic strength buffer. Rather, a positive non-zero slope for the later stages of condensation reaction in the high

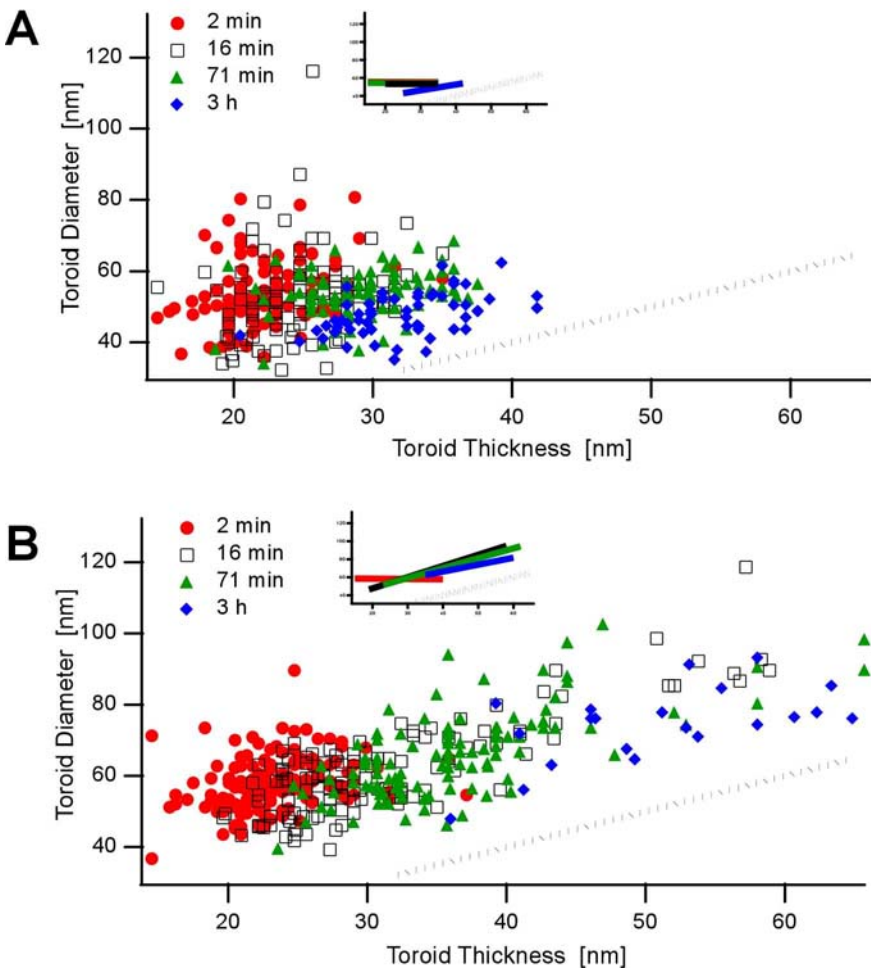

Figure 2.9 The analysis of toroid growth at different reaction times and two different ionic strengths. Toroid diameter is defined as an arithmetic mean of the outside diameter of the toroid and the diameter of the toroid hole. Toroid thickness is defined as the difference between toroid diameter and the diameter of toroid hole. All the data sets were obtained by condensing *3kbDNA* as described in the caption to Figure 2.1. (A) Toroid diameter and thickness measurement for the sample of condensed *3kbDNA* in a low ionic strength buffer and different reaction times. Inset: a plot of linear best-fits for the toroid diameter versus toroid thickness data. (B) Toroid diameter and thickness measurements for the sample of condensed *3kbDNA* in a high ionic strength buffer and different reaction times. Inset: a plot of linear best-fits for the toroid diameter versus toroid thickness data for the sets of measurements.

ionic strength buffer indicates a change in toroid growth mechanism where new DNA is now preferentially adding to the outside of the growing toroid. The kinetic data obtained in the high ionic strength buffer provided additional support for previously proposed model of toroid growth at high ionic strengths (63).

2.3.9. DNA condensation mechanism after initial nucleation and growth

The mechanisms of toroid and rod formation have usually been considered independently (Figures 1.8, 1.11, 1.15). However, the changes in DNA condensate morphology and size observed upon condensation of DNA with hexammine cobalt suggest a more involved mechanism of DNA condensation to account for the observed temporal decrease in relative rod population and growth of DNA condensates.

The proposed model of DNA condensation connects the individual mechanisms of toroid and rod formation by acknowledging free DNA as a common intermediate for both mechanisms (Figure 1.10). The observed decrease in relative rod population and toroid growth can be understood in terms of DNA strand exchange between individual DNA condensates to achieve their thermodynamically more stable state. As discussed in Chapter 1, condensation begins by nucleation of individual DNA condensates and subsequent formation of monomolecular condensates (Figure 2.10). The relative populations of proto-toroids and proto-rod during the first step of DNA condensation have not been determined experimentally. Molecular and Brownian dynamics simulations have suggested that rod nucleation (Step II in Figure 2.10) is kinetically favored over toroid nucleation (Step I in Figure 2.10) (23,61). It has been proposed that the kinetic favorability of rod nucleation is due to a shorter section of DNA polymer required for rod

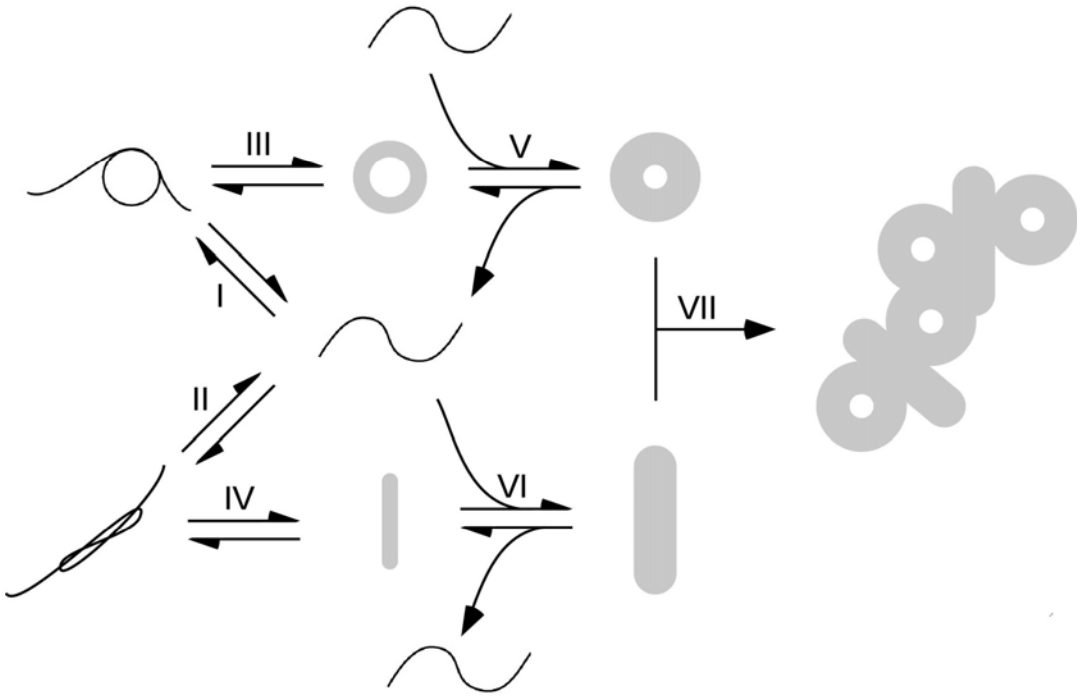

Figure 2.10 Toroid and rod nucleation and growth are part of an interconnected pathway that results in the growth of toroids and disappearance of rod condensates from the reaction mixture. Free DNA plays a central role in this exchange of DNA between two distinct morphological forms. All proposed steps of the mechanism denoted as equilibrium steps. I – Nucleation of a toroid by a nucleation loop. II – Nucleation of a rod by a sharp bend in DNA backbone. III – A formation of a proto-toroid by an intramolecular collapse of the remainder of DNA onto the nucleation loop. IV – A formation of a proto-rod by an intramolecular collapse of DNA. V – A growth of the proto-toroid by the addition of free DNA from the solution. A growing toroid can also decrease in size, releasing a free DNA into solution. VI – A growth of proto-rod by the addition of free DNA from the solution. A growing rod can dissociate to smaller rods by releasing free DNA into the solution. VII – At longer reaction time, individual DNA condensates form clusters and aggregates.

nucleation compared to toroid nucleation (61). Nevertheless, the observed decrease in relative rod population at shorter reaction times (Figure 2.2) suggests that the quasi-equilibrium relative toroid and rod populations are not determined solely by the respective initial nucleation rates. Instead, the growth of toroids and rods (steps V and VI in Figure 2.10, respectively) is counteracted by their dissociation which is indicated by equilibrium arrows in Figure 2.10. The overall increase in relative toroid population with

respect to rod population (Figure 2.2) indicates that rod dissociation rates must be higher than toroid dissociation rates, reflecting the higher thermodynamic stability of toroids that has been suggested by numerous theoretical studies (13,20,24,60,62,77,93). The quasi-equilibrium relative toroid and rod population (97% and 3%, respectively, from Figure 2.2) must then result from nucleation rates as well as rates of toroid and rod growth and dissociation. On the time scale of this study, rods dissociate and release free DNA that can either nucleate new condensates or add on pre-existing toroids and rods (Figure 2.10).

Individual toroids and rods are only transiently stable and have been observed to cluster and aggregate at longer reaction time (Figure 2.1). This is in agreement with the result of previous studies of DNA condensation by hexammine cobalt chloride (54). The gradual decrease in the concentration of individual DNA condensate suggests that neither toroids nor rods represent the thermodynamically stable state of DNA condensed by hexammine cobalt. Instead, larger clusters and aggregates should represent thermodynamically favored state of DNA condensates (Step VII in Figure 2.10). The increased population of clusters of individual condensates as well less morphologically less defined aggregates at longer reaction times suggests that individual condensates under our experimental conditions do not represent a thermodynamically stable state. Thus, quasi-equilibrium condensate structures (i.e. toroids and rods) will ultimately cluster and aggregate to form large particles that tend to precipitate (Figure 2.10).

2.4. Concluding remarks

The results presented demonstrate the dynamic nature of a DNA condensation reaction. Previously, it has been demonstrated that DNA condensate formation proceeds through initial nucleation and subsequent growth of individual condensates (14,63,90,96). In addition to these two basic steps of DNA condensate formation, it is shown here that some of the DNA condensates undergo a morphological change from rods to toroids until a quasi-equilibrium relative rod population is reached. DNA condensates have also been observed to grow considerably which is in agreement with previously published data (54).

Finally, several different origins of toroid size limits have been proposed in the literature (13,14,20,21,36,43,77,87,105,106,131-133). These thermodynamic and kinetic models for the origin of toroid size limits have considered toroid sizes that have been reported in the literature and have been based on measurements of toroids obtained usually within the first 30 min after condensation reaction initiation (3,7,10,29,56,80,104,134). Our toroid size measurements indicate that toroids do not reach their final size after 30 min reaction time. Furthermore, progressive clustering and aggregation at longer reaction times accompany DNA condensate growth which may prevent determination of toroid size limits for experimental conditions similar to ours.

3. THE EFFECT OF DNA FRAGMENT LENGTH ON DNA CONDENSATE MORPHOLOGY AND CONDENSATION MECHANISM

3.1 Introduction

DNA condensation is most commonly defined as the collapse of DNA molecules from solution upon the addition of cations with a charge of three or more (13,14). The two most distinguishing characteristics of DNA condensates are size and morphology. Condensate size has been studied extensively as a function of condensing agent and sample solution conditions, and has recently been shown to depend on the kinetics of condensate nucleation and growth (63,102,106). In the presence of commonly used condensing agents (e.g. hexammine cobalt chloride, spermidine) DNA condensates predominately adopt two morphologically distinct species: toroids and rods (13). Other morphological forms, such as spheroids, have been observed in the presence of highly charged polycations (53,135).

The ratio of toroids to rods formed in a DNA condensation reaction can depend upon the nature of the condensing agent, polarity of the solvent, and DNA length (13,55,56,136). For example, in one study concerning the effect of DNA length on condensate morphology, Marquet et al. reported that 258 and 436 bp DNA fragments condense exclusively into rods, whereas DNA fragments longer than 748 bp favor toroid formation (55). The tendency of shorter DNA fragments to form rods has been attributed

to the limited flexibility of DNA, which has a persistence length of approximately 150 bp. The semi-rigid nature of DNA implies that at some limiting length DNA will disfavor toroid formation, at which point DNA strands would associate exclusively into rod-like bundles. However, experimental and theoretical studies indicate that the 436 bp DNA molecules used by Marquet et al. can still readily form smooth loops at room temperature that are the size of DNA loops within toroidal condensates (128,129,137-140). Thus, it appears that the origin of DNA length effects on condensate morphology has not been adequately explained (43,55,56).

Molecular and Brownian dynamics simulations have shown toroids to be the most thermodynamically stable state of a condensed, long semi-rigid polymer (61,85,93), whereas rod-like structures represent a metastable state (60). However, polymer dynamics simulations indicate that rods can be kinetically favored due to a higher probability of nucleation (61). The distribution of DNA condensates between toroids and rods can therefore depend on both the thermodynamics and kinetics of DNA condensate formation. Although the energetics of toroid and rod formation has been modeled in some detail, theoreticians have not addressed the potential kinetic effects of DNA length on DNA condensate morphology.

The present study was motivated by our search for mechanisms to control DNA condensation and recent theoretical results that indicate condensate morphology is determined during the nucleation stage of condensation (23,61). DNA molecules of different lengths were condensed with hexammine cobalt chloride and the resulting particles were examined by transmission electron microscopy (TEM). We have also studied condensation of the same set of DNA molecules in the presence of static DNA

loops. Our results are consistent with previous reports that a decrease in DNA length causes an increase in rod condensate population. However, the variety of DNA molecules used in this study has allowed for a greater characterization of the effects of DNA length on condensate morphology. We have also found that the addition of DNA static loops largely reverses the trend towards rod formation that is observed for DNA of decreasing length. These results have direct implications concerning the importance of condensate nucleation on the appearance of rod-like condensates.

3.2 Experimental Procedures

3.2.1. DNA Preparation

Bluescript II SK- plasmid DNA (Stratagene) was grown in DH5α (Life Technologies, Rockville, MD) and isolated by using the Qiagen Maxi Prep kit (Valencia, CA). The DNA was eluted with 1× TE (10 mM Tris, pH 7.8, 1 mM EDTA) in the final column purification step. The purified plasmid DNA, referred to as *3kbDNA*, was linearized with *Hin*dIII (New England Biolabs). A Bluescript II SK- plasmid was previously modified by the insertion of two tandem repeats of the multiple phased A-tract sequence 5'-ATCCATCGACC($A_6CG_3CA_6CG_2C$)$_7$A6GCAGTGGAAG-3', which produces approximately one full loop of sequence-directed curvature (96). This A-tract-rich plasmid was grown in Sure2 Supercompetent cells (Stratagene), purified as described above and linearized with *Hin*dIII (referred to as *3kbAtract*). To obtain DNA of shorter lengths, *3kbDNA* and *3kbAtract* were digested with one or two additional restriction enzymes. *3kbDNA* digested with *Sca*I yielded a mixture of 1.1 kb and 1.8 kb fragments (referred to as *1.5kbDNA*). *3kbDNA* was digested with *BspH*I to obtain a mixture of 0.8

kb, 1 kb, and 1.2 kb fragments (referred to as *1kbDNA*). *3kbAtract* digested with *Xba*I (referred to as *3kb_Atract*) produced a 2.9 kb fragment (equivalent to *3kbDNA*) and a 0.4 kb fragment containing the region of A-tract sequence-directed curvature. *Sca*I restriction digestion of *3kbAtract* produced a 1.1 kb fragment and a 2.2 kb fragment containing the sequence-directed curvature (referred to as *1.5kbAtract*). *3kbAtract* digestion with *BspH*I resulted in a mixture of 0.8 kb and 1 kb fragments, with a 1.5 kb fragment containing the sequence-directed curvature (referred to as *1kbAtract*). *3kbAtract* was also double-digested by the enzymes *Xba*I and *BspH*I to obtain a mixture of 0.8 kb, 1 kb and 1.1 kb fragments with a 0.4 kb fragment containing the sequence-directed curvature (referred to as *1kb_Atract*). Restriction enzyme buffers were removed from all DNA samples after digestion by rinsing at least five times with 1× TE using a Microcon YM-30 spin column (Amicon). After the final rinse, DNA samples were resuspended in 1× TE. DNA concentrations were determined spectrophotometrically.

Mixed DNA samples, named *3kbAtract+1kbDNA*, *1.5kbAtract+1kbDNA*, and *1kbAtract+1kbDNA*, were prepared by mixing 2.5 μl of 20 μg/ml of *3kbAtract*, *1.5kbAtract*, and *1kbAtract* with 3.0, 2.3, and 1.5 μl of 20 μg/ml *1kbDNA*, respectively. Mixtures *1.5kbAtract+1kbDNA* and *1kbAtract+1kbDNA* were diluted with 1× TE to obtain the same concentration of sequence-directed curvature as that present in *3kbAtract+1kbAtract*.

3.2.2. DNA Condensate Preparation and Analysis

Each DNA sample was diluted from a stock solution to 20 μg/ml in 1× TE and mixed with an equal volume of 200 μM hexammine cobalt chloride (Sigma) to yield a

condensation reaction mixture 10 μg/ml in DNA, 100 μM in hexammine cobalt chloride, and 0.5× in TE buffer. DNA condensate reactions were allowed to equilibrate at room temperature for 5 min and then deposited on carbon-coated grids (Ted Pella). After 10 min an equal volume of 2% uranyl acetate (Ted Pella) was added to the condensate mixtures on the grids. After 1 min incubation, grids were rinsed in 95% ethanol and air dried. Grids prepared for each of the DNA condensate samples were examined using a JEOL-100C transmission electron microscope (TEM) to analyze DNA condensate morphology. Images of DNA condensates were recorded on film at 100,000× magnification. TEM negatives were scanned at 300 dpi into electronic format, and a graphics program was used to measure the dimensions of individual DNA toroids.

3.3 Results and Discussion

3.3.1. The effect of DNA fragment length on condensate morphology

We have examined the effects of DNA length on the size and morphology of DNA condensates. For a range of solution conditions, hexammine cobalt chloride is known to condense DNA (≥3 kb in length) into toroids and rods, with other morphologies representing only a minor fraction of the condensate population (13,43,56,124,125,136). Similarly, all DNA condensation experiments described in the present study yielded toroids and rods as the two most common morphologies. Other morphologies (e.g. spheres, clusters and aggregates) represented only minor fractions of DNA particles (~1%). Thus, the statistics reported here for condensate morphology are based exclusively on the observed number of toroids and rods.

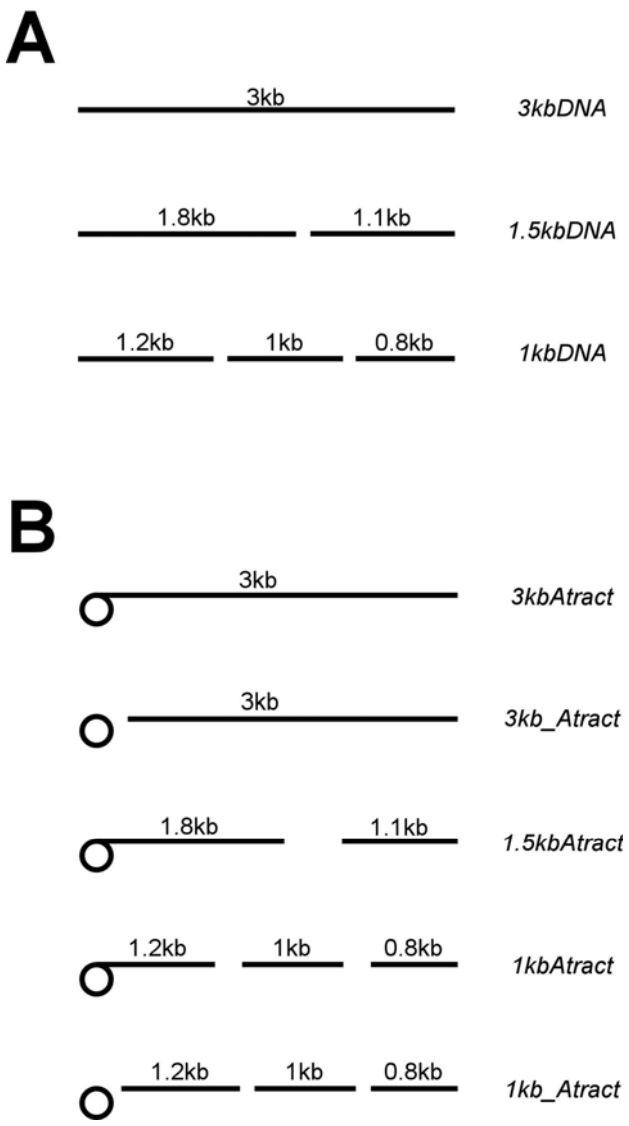

Figure 3.1 Schematic representations of the DNA samples used in this study. Fragments of in each sample are represented by lines that are proportional in length to the DNA fragment in each sample. In all samples, fragments were present in equal molar concentrations. The source DNA plasmids followed by restriction enzymes used to create fragments for each sample are given to the right of each sample scheme. Names given in parentheses are used in text. (A) The three DNA samples obtained by restriction digestion of the 2961 bp plasmid DNA Bluescript II SK- (*3kbDNA*). (B) The five DNA samples obtained by restriction digestion of a 3309 bp plasmid DNA containing one complete static A-tract loop (*Atract30*). The lengths given for fragments with attached loops do not include the length of DNA contributed by the static A-tract loop. All DNA samples where initially digested with the restriction enzyme *Hin*dIII to linearized the circular DNA plasmids.

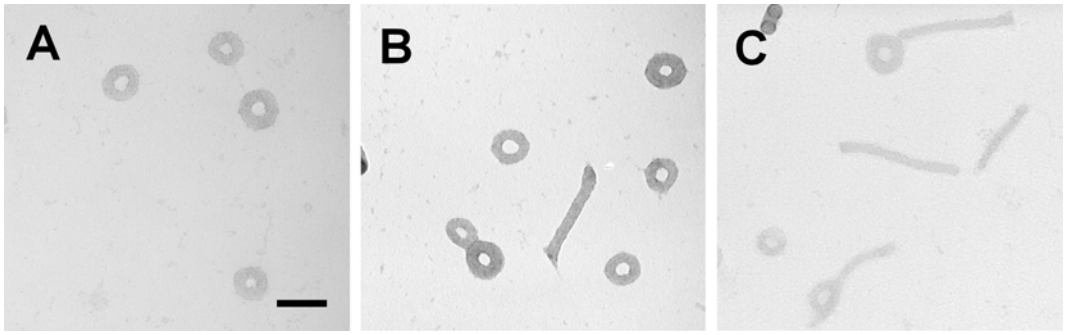

Figure 3.2 Transmission electron microscopy images illustrating the effect of DNA fragment length on DNA condensate morphology. (A) Condensates produced by the sample *3kbDNA*. (B) Condensates produced by the sample *1.5kbDNA*. (C) Condensates produced by the sample *1kbDNA*. Scale bar is 100nm. Magnification is the same for all three images. Complete descriptions of the DNA samples that correspond to the abbreviated names are given in Materials and Methods. All DNA samples were condensed by hexammine cobalt chloride in a condensation reaction mixture of 10 μg/ml DNA, and 100 μM hexammine cobalt chloride in 0.5× TE buffer (5 mM Tris, pH 7.8, 0.5 mM EDTA).

Linear 2961 bp plasmid DNA (*3kbDNA*) was digested with selected restriction enzymes to obtain mixtures of shorter DNA fragments (Materials and Methods). The resulting DNA samples are referred to as *1.5kbDNA* and *1kbDNA*; simplified names that reflect the average length of DNA fragments in the respective samples (Figure 3.1A). All DNA samples were condensed at a DNA concentration of 10 μg/ml by 100 μM hexammine cobalt chloride in a low ionic strength buffer (5 mM Tris, pH 7.8, 0.5 mM EDTA). *3kbDNA* condensed into toroids as well as rods (Figure 3.2A), with toroids and rods representing 89% and 11% of the condensate population, respectively (502 toroids, 60 rods) (Figure 3.3). *1.5kbDNA*, containing 1.1 and 1.8 kb fragments, also produced a mixture of toroids and rods, but with an appreciable increase in relative rod population as compared to *3kbDNA* (Figure 3.2B). In this case, rods represented 20% of the condensate particles (585 toroids, 145 rods) (Figure 3.3). Condensation of *1kbDNA*, a DNA sample containing three fragments each approximately 1 kb in length, produced an even greater

proportion of rods (Figure 3.2C), with the rod population increasing to 37% and the toroid population decreasing to 63% (425 toroids, 250 rods) (Figure 3.3).

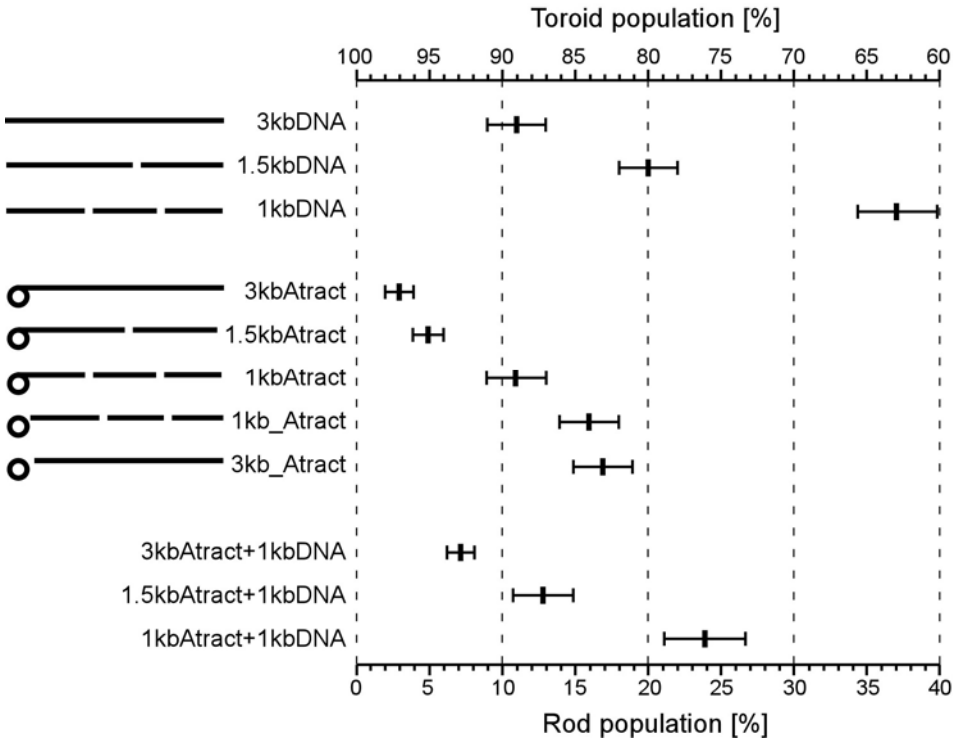

Figure 3.3 Graphical representation of how DNA fragment length and static A-tract loops affect the relative populations of toroids and rods when DNA is condensed by hexammine cobalt chloride. Rod and toroid populations were determined using transmission electron microscopy. The statistics are based only on the number of toroids and rods, as other condensate morphologies (i.e. spheres, clusters, aggregates) accounted for less than 1% of DNA condensates. The total number of toroids and rods counted exceeded 400 for each data point shown. Complete descriptions of the DNA samples that correspond to the abbreviated names are given in Materials and Methods. Error bars are based on at least two independent preparations for each DNA sample.

The observed increase in rod population with decreasing DNA fragment length illustrates the clear dependence of condensate morphology on DNA length. Arscott et al. observed a similar trend, reporting that both 2.7 kb and 1.4 kb DNA lengths condense into rods and toroids, but that the 1.4 kb DNA sample produced a higher relative

population of rods (56). Marquet et al., on the other hand, have reported that DNA fragments longer than 500 bp condensed exclusively into toroids, whereas DNA fragments shorter than 500 bp condensed exclusively into rods. Our results indicate a more gradual increase in the relative population of rods as DNA length is decreased.

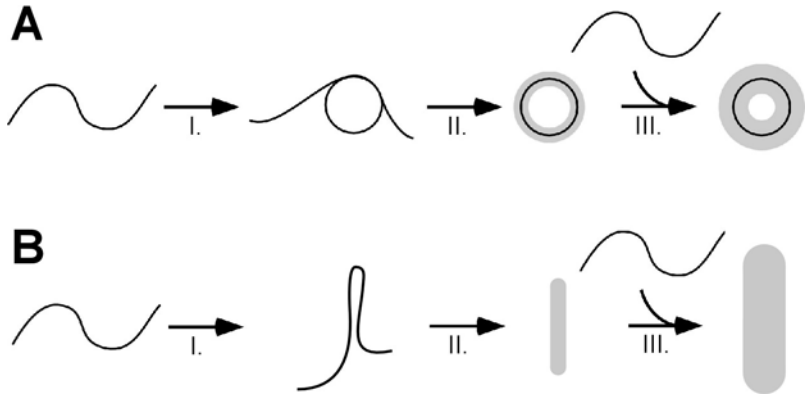

Figure 3.4 Models of the nucleation-growth mechanism for DNA toroid and rod formation. The first two steps represent nucleation of DNA condensation by the formation of a monomolecular condensate, followed by the growth stage in which the condensates grow by intermolecular DNA condensation. (A) I. – Toroid formation is initiated by the spontaneous formation of a *nucleation loop*. II. – This loop acts as a nucleation site for condensation onto which the remainder of DNA fragment condenses to form a monomolecular condensate (i.e. *proto-toroid*). III. – The proto-toroid grows by the addition of free DNA fragments from the solution. (B) I. – Rod formation has been proposed to be initiated by a *sharp bend* in the DNA helical axis (61). II. – The remainder of the DNA fragment condenses onto itself to form a monomolecular condensate (i.e. *proto-rod*). III. – The proto-rod grows by the addition of free DNA fragments from the solution.

3.3.2. DNA fragment length primarily alters condensate nucleation

For both toroid and rod formation, DNA condensation can be described as a nucleation-growth process (Figure 3.4) (13,23,60,63,76,93). It is conceivable that DNA fragment length affects the nucleation stage, the growth stage or even both stages of condensation. As a means of probing the possible role of nucleation in the observed increase in rod

population (and corresponding decrease in toroid population) with reduced DNA length, we introduced static DNA loops into samples of DNA with various fragment lengths. We have recently demonstrated that static loops act as built-in (i.e. kinetically favored) nucleation sites for toroid formation (63,96). Thus, the introduction of static loops represents a potential method to kinetically favor toroid nucleation without necessarily altering the kinetics or thermodynamics of rod formation.

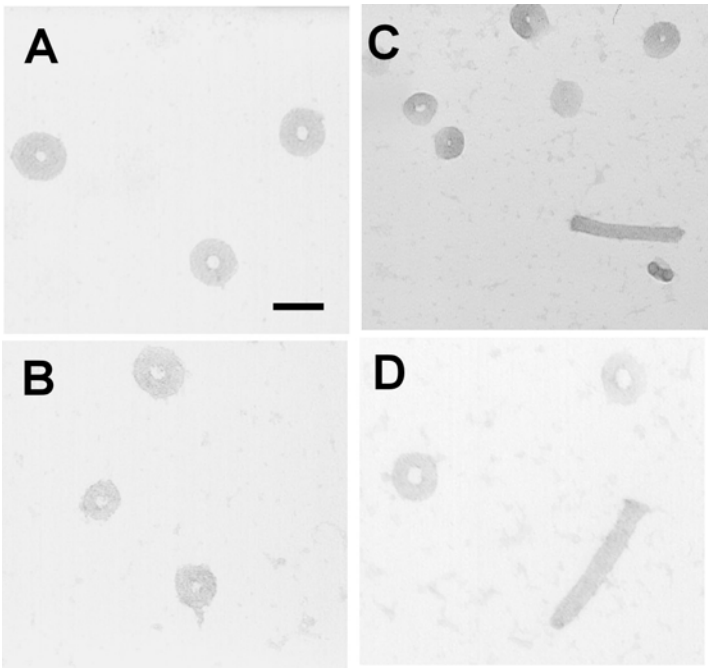

Figure 3.5 Transmission electron microscopy images illustrating the effect of static A-tract loops on DNA condensate morphology for samples with different fragment lengths. (A) Condensates formed by the sample *3kbAtract*. (B) Condensates formed by the sample *1.5kbAtract*. (C) Condensates formed by the sample *1kbAtract*. (D) Condensates formed by the sample *1kb_Atract*. Scale bar is 100 nm. Magnification is the same for all images. Complete descriptions of the DNA samples that correspond to the abbreviated names are given in Materials and Methods. All DNA samples were condensed by hexammine cobalt chloride in a condensation reaction mixture of 10 μg/ml DNA, and 100 μM hexammine cobalt chloride in 0.5× TE buffer (5 mM Tris, pH 7.8, 0.5 mM EDTA).

Static DNA loops were introduced into a 3 kb plasmid DNA by the incorporation of multiple A-tract sequences (96). An A-tract is a sequence of four to six A·T base pairs that creates a static bend in the DNA helical axis of approximately 13° (97,126). If multiple A-tract sequences are phased along a DNA molecule with respect to the helical twist of B-form DNA, an accumulative amount of static curvature can be produced. A 3.3 kb DNA plasmid containing static curvature of approximately 360° (i.e. one complete static A-tract loop) over a sequence of 346 bp (i.e. a 37 nm diameter loop) was digested with the restriction enzyme *Hin*dIII so that the static loop was located near one end of the linearized plasmid (*3kbAtract*). This DNA was further digested to obtain samples with varying average fragment lengths and one fragment containing the static A-tract loop (Figure 3.1B).

When *3kbAtract* was condensed by hexammine cobalt chloride, toroids accounted for 97% of all condensates (682 toroids, 18 rods) (Figures 3.3, 3.5A). The observation of only 3% rod-like condensates for *3kbAtract* is in contrast to the 11% rod population observed for *3kbDNA*, a DNA of essentially the same length but without a static A-tract loop. This reduction in rod population for *3kbAtract* is consistent with an increased kinetic advantage of toroid formation over rod formation due to the presence of a static nucleation loop. Digestion of *3kbAtract* with the restriction enzyme *Sca*I produced a sample referred to as *1.5kbAtract*; a mixture of 1.1 and 1.8 kb fragments with the static loop attached to the 1.8 kb fragment (Figure 3.1B). The *1.5kbAtract* sample produced a condensate population similar to that of the *3kbAtract* sample (Figure 3.5B). Toroids again represented the clear majority of condensates, accounting for 95%, with rods representing only 5% (446 toroids, 25 rods) (Figure 3.3). Furthermore, the static A-tract

loop on the 1.8 kb fragment in the *1.5kbAtract* sample decreased the rod population from 20% to 5%, in comparison to the *1.5kbDNA* sample which had similar DNA fragment lengths but no static A-tract loop (Figure 3.3). *3kbAtract* was further digested to produce the *1kbAtract* DNA sample, in which three fragments of approximately 1 kb were present with the static A-tract loop near the end of one of these fragments (Figure 3.1B). When condensed by hexammine cobalt chloride, the *1kbAtract* sample produced a relative toroid population of 89%, and a rod population of 11% (889 toroids, 110 rods) (Figures 3.3 and 3.5C). The 11% rod population of *1kbAtract* represents a substantial reduction from the 37% rod population observed for *1kbDNA*.

If DNA condensate morphology is determined during nucleation, then toroid formation would be expected to increase in samples containing the static A-tract loops compared to similar fragment length without A-tract loops (63,96). We have clearly shown this is the case. The condensates of DNA samples containing average fragment lengths of 3 kb, 1.5 kb and 1 kb were all consistently lower in relative rod population for the set of DNA samples that contained the static A-tract loop on one of the DNA fragments (Figure 3.3).

The particular fragment in *1kbAtract* that contains a static A-tract loop is expected to nucleate toroids more effectively than the corresponding fragment in *1kbDNA*, which does not contain a static loop. However, if this fragment of *1kbAtract* condensed exclusively into toroids, but did not alter the condensation of the other two fragments, then one would expect a reduction in rod population from that of 37% observed for *1kbDNA* to approximately 24% for *1kbAtract*. Our observation of only 11% rods produced by the *1kbAtract* sample indicates that the fragment with the static A-tract loop

reduces the population of rods produced by all three fragments. This result demonstrates that toroid formation does not become limited thermodynamically as DNA length is decreased to around 1 kb as much as it becomes less kinetically favored. Thus, the appearance of more rods in DNA samples with shorter fragment lengths is apparently due to a reduced likelihood of toroid condensate nucleation, which can be reversed by the introduction of static A-tract loops.

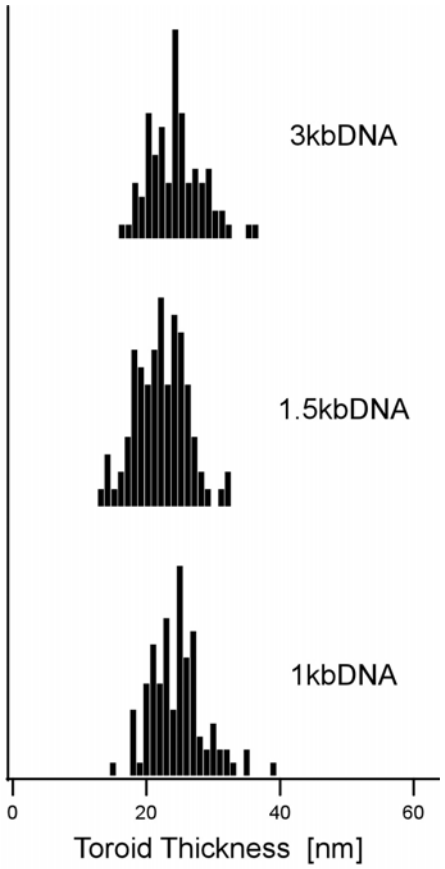

Figure 3.6 DNA sample average fragment length and its effect on toroid thickness. The corresponding abbreviations for DNA samples are given to the right of the histograms. The mean toroid thickness of 25 ± 4 nm, 24 ± 4 nm, and 24 ± 4 nm were measured for *3kbDNA*, *1.5kbDNA*, and *1kbDNA*, respectively. Description of condensation conditions are given in Figure 3.1.

It has been previously demonstrated that suppressing the rate of toroid nucleation causes an increase in toroid thickness (63,102). This phenomenon is easily understood in terms of the nucleation-growth mechanism of toroid formation. Briefly, when DNA condensate nucleation is sufficiently rapid, condensate dimensions are limited by the depletion of uncondensed DNA molecules from solution. Under such reaction conditions, toroid thickness is said to be kinetically limited. Decreasing the rate of toroid nucleation, by increased temperature or ionic strength, can increase toroid size until toroid thickness eventually becomes thermodynamically limited (63,102). In the present study, toroid thickness measurements were used as a means to evaluate the possible effects of DNA fragment length on the kinetics of condensate nucleation. The mean thickness of toroids produced by *3kbDNA*, *1.5kbDNA*, and *1kbDNA* were 25 ± 4 nm, 24 ± 4 nm, and 24 ± 4 nm, respectively. These thickness measurements are the same for all three samples, within experimental error. Furthermore, the distributions of toroid thickness for these samples are statistically indistinguishable (Figure 3.6). These results demonstrate that the decrease in DNA length from 3 kb to 1 kb does not substantially decrease the absolute rate of condensate nucleation (i.e. nucleation of toroids and rods). Thus, the observed increase in rod population with decreasing DNA length illustrates the sensitivity of condensate morphology to a relative change in toroid nucleation with respect to rod nucleation.

3.3.3. The relative impact of loop formation and proto-toroid stability on condensate morphology

The nucleation step of DNA toroid formation can be subdivided into two events: the formation of a nucleation loop along a DNA fragment followed by the intramolecular

condensation of the remaining fragment onto this loop to form a proto-toroid (Scheme 3.4A) (63,102). Once the proto-toroid has formed, the growing toroid increases in size and stability by the addition of other DNA molecules from solution (Scheme 3.4A). For the experiments presented above, proto-toroids would contain between 1 kb and 3 kb of DNA, depending on the length of DNA fragments in a particular sample. The observed increase in rods with decreasing DNA length, and the corresponding decrease in toroids, could result from a decrease in toroid nucleation loop formation or a decrease in proto-toroid stability. We first address the possibility that decreases in toroid populations are due to reduced spontaneous loop formation along shorter DNA fragments.

A comparison of the condensates formed by the sample *1kb_Atract* with those of *1kbDNA* demonstrates the effect of increasing the number of DNA loops present at the time of condensation. The *1kb_Atract* and *1kbDNA* samples contain the same length DNA fragments, except that sample *1kb_Atract* also contains a static A-tract loop, which is detached from the other DNA fragments (Figure 3.1B). The A-tract loop in sample *1kb_Atract* could serve as a toroid nucleation element for the other DNA molecules in the solution, but would not form a stable proto-toroid by itself due to its lack of a linear DNA extension for intramolecular condensation. The condensation of *1kb_Atract* with hexammine cobalt chloride yielded a condensate mixture of 84% toroids and 16% rods (849 toroid, 164 rods) (Figure 3.3). This distribution of rods and toroids is significantly higher in toroids as compared to the condensates of *1kbDNA*, which had a relative population of 63% toroids and 37% rods (Figure 3.3). The production of 84% toroids by *1kb_Atract* is in fact closer to the 89% toroid population observed for *3kbDNA*, and greater than that observed for *1.5kbDNA* (i.e. 80%). Thus, the introduction of detached

static loops into a 1 kb DNA sample almost completely reverses the effect of DNA length on condensate morphology. This result supports a decrease in nucleation loop formation as being the principal reason why toroid populations decrease, and rod populations increase, with decreasing DNA fragment length.

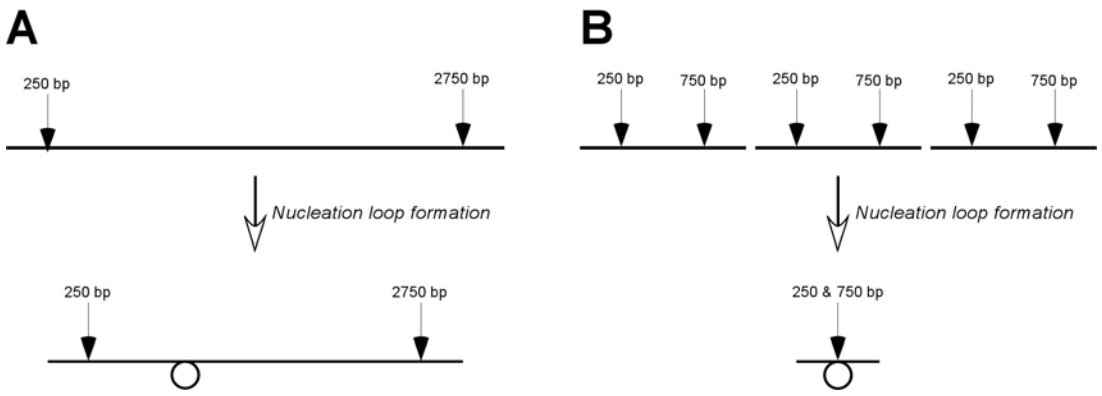

Figure 3.7 The number of conformational states that produce a nucleation loop of a particular size depends directly on the length of the DNA fragment. (A) For a linear 3 kb plasmid DNA, a nucleation loop of 500 bp can be centered at any base pair between the 250th and the 2750th base pair. The total number of possible conformations of a DNA polymer leading to a nucleation loop of 500 bp is proportional to the length of this central region (i.e. 2.5 kb for 3 kb DNA). (B) If the sample 3 kb long DNA plasmid is cut into three 1 kb long DNA fragments, the number of conformations leading to 500 bp nucleation loop decreases significantly. For each resulting 1 kb DNA fragment, a 500 bp long nucleation loop can only be centered between the 250th and 750th base pair. The total number of conformations able to produce a 500 bp long nucleation loop for the three 1 kb DNA fragments is proportional to the combined length of the central regions of the three fragments (i.e. 1.5 kb for three 1 kb fragments). The same conclusions apply to nucleation loops of different sizes.

The origin of reduced toroid nucleation loops with decreasing DNA length is a direct consequence of the semi-ridged nature of DNA. The probability of forming a nucleation loop of a particular size depends on the persistence length of DNA and the number of possible conformations of the DNA polymer that produce a loop of a given

size (10,76,129,137,138,140). The persistence length is an intrinsic property of DNA that does not change with fragment length. However, the number of conformational states of a DNA polymer depends directly on fragment length. For example, a 500 bp loop of DNA can be centered at any of the central 2.5 kb of a 3 kb DNA fragment (Scheme 3.7A). In contrast, if the same 3 kb DNA is cut into three equal pieces, then a 500 bp loop can only be centered within the central 500 bp in each of the three 1 kb fragments (Scheme 3.7B). Thus, for two samples with the same mass concentration of DNA, but with different fragment lengths, the sample with the longer fragments would be expected to have more conformational states that produce loops for toroid nucleation.

We have shown that promoting toroid nucleation by the introduction of static A-tract loops largely reverses the increased rod populations that are observed for DNA samples of decreasing length. We have argued that these results indicate that the well-documented shift in condensate morphology towards rods is due to a reduction in toroid nucleation with DNA length. This proposal assumes that the mechanism for rod nucleation is not enhanced by the shortening of DNA strands, only that toroid nucleation is decreased more than rod formation. In the following section, we present arguments for why rod nucleation is expected to not decrease as readily as toroid nucleation with DNA fragment length.

The population of rods produced by *1kb_Atract* was slightly greater than that produced by *1kbAtract* (Figure 3.3). These two samples differ only in that the A-tract static loop is attached to the end of a 1.2 kb fragment in *1kbAtract*, but not connected to a linear fragment of significant length in *1kb_Atract*. This result indicates that proto-toroid stability also affects the final population of toroids in a condensate reaction, albeit to a

lesser extent than nucleation loop formation. Samples composed from mixtures of the DNA samples described above were designed to specifically probe the effect of proto-toroid stability on toroid and rod populations. Samples *1kbAtract+1kbDNA*, *1.5kbAtract+1kbDNA* and *3kbAtract+1kbDNA* were prepared such that each contained the same concentration of DNA fragments shorter than 1.5 kb and the same concentration of the static A-tract loop (Experimental procedures). The length of linear DNA extending from the A-tract loop in *1kbAtract+1kbDNA*, *1.5kbAtract+1kbDNA* and *3kbAtract+1kbDNA* samples was 1.2 kb, 1.8 kb and 3 kb, respectively. The relative toroid populations of *1kbAtract+1kbDNA*, *1.5kbAtract+1kbDNA* and *3kbAtract+1kbDNA* samples increased as the length of DNA extending from the static A-tract loop increased: 76%, 86% and 93% toroids, respectively (Figure 3.3). Decreasing the length of DNA extending from the static A-tract loop clearly reduces the ability of the static A-tract loop to govern the condensate morphology of other DNA fragments in the solution. This observation can be understood by considering the fact that proto-toroid stability depends on the number of intrastrand contacts in a condensed DNA fragment, which is directly proportional to the length of the DNA fragment (13). As DNA fragment lengths are shortened, the probability increases that a proto-toroid will spontaneously decondense before being stabilized by the addition of other DNA strands. Thus, decreased proto-toroid stability can also result in a decrease in toroid populations.

It should be noted that the results obtained for one DNA sample are not explained by the same logical arguments that explain the results obtained for all other samples. For example, the *3kb_Atract* sample (Figure 3.1B), which has the static A-tract loop detached from a linear 3kb fragment would be expected to yield a relative rod population

intermediate to that of *3kbAtract* and *3kbDNA* (i.e. between 3% and 11%) because the free static A-tract loop would be expected to either increase toroid formation or have little net effect on condensate morphology. However, the relative rod population measured for *3kb_Atract* was 17% (Figure 3.3). The reason for this unexpectedly high relative rod population is currently under investigation.

3.3.4. DNA fragment length and rod nucleation

Unlike toroids, rod morphology has been proposed to nucleate by more than just one proto-rod structure. Folded chain and racket structures have been predicted by theoretical analysis as well as by computer simulations of monomolecular DNA condensation (60,62,141,142). Similar structures have been observed experimentally with atomic force microscopy (143). Regardless of the exact proto-rod structure, their formation has been shown to require one or multiple sharp bends in the DNA helical axis (23) (Figure 3.4B). The 'sharpness' of a bend depends on the length of DNA polymer involved in bending the DNA helical axis; the shorter the polymer length, the sharper the bend in DNA helical axis. The critical length of DNA polymer to consider a bend of a given angle as a '*sharp bend*' has not been strictly defined. In any case, a sharp bend in the DNA duplex should be a much more localized structure than the smooth nucleation loops required for toroid nucleation. This difference in nucleation element size could provide a kinetic advantage for rod nucleation over toroid nucleation as DNA length is suppressed, as rod nucleation sites would be expected to be less sensitive to changes in DNA length. Thus, an absolute decrease in the probability of toroid nucleation, rather than an absolute increase in the probability of rod nucleation, are likely the origin of the observed increase in rod populations with decreased DNA length.

3.4 Concluding Remarks

The morphological distribution of DNA condensates has previously been shown to depend upon several physical parameters. In this report, we have revisited the effect of DNA length on condensate morphology. We have shown that fragment length primarily influences the kinetics of DNA condensate nucleation. Decreasing DNA fragment length reduces the probability of forming toroid nucleation structures and decreases the stability of proto-toroids. These deleterious effects on toroid formation explain the observed increase in the population of rod-like condensates with decreasing DNA length.

Biotechnological applications of *in vitro* DNA condensation (e.g. gene and antisense therapies) require particles to be as small as possible and of uniform morphology (55,56,144). The results presented here provide an additional understanding of the factors that govern DNA condensation *in vitro*, which is necessary if we are to ultimately obtain complete control over the size and shape of DNA condensates. Previously, we have shown that static A-tract loops decrease toroid dimensions (63,96). Here we have demonstrated that the presence of static A-tract loops significantly increase the population of toroids produced by DNA fragments of lengths less than 3 kb. As shown above, static A-tract loops can favor toroid morphology even in solutions of DNA fragments shorter than 1.5 kb, which tend to condense into a mixture of condensates with a high relative rod population. However, for maximum efficiency, static A-tract loops must be attached to a length of DNA long enough to provide sufficient intrastand contacts to stabilize proto-toroid formation. Successful formation of this structure would allow other DNA fragments to collect onto the proto-toroid and promote growth. Static A-tract

loops could thus prove useful in controlling DNA condensate size and morphology for biotechnological applications that require condensed DNA.

4. SPHERICAL DNA CONDENSATE MORPHOLOGY

4.1 Introduction

The preceding two chapters have focused on toroids and rods, the two most commonly observed morphologies of single DNA condensates achieved by condensation with hexamine cobalt, spermidine, or spermine. Other morphologies have usually been reported to represent only a minor fraction of DNA condensates, with spherical particles shown to never exceed 1% of all DNA condensates obtained with hexamine cobalt (14,43). Similarly, toroids and rods have been confirmed by theoretical analysis as well as molecular and Brownian dynamics simulations to be the two most stable morphological forms of a condensed *semi-flexible* polyelectrolyte, such as DNA (24,60-62,77,93,123). This is in agreement with theoretical studies and computer simulations of polyelectrolyte condensation in the presence of general counterions, which predict a spherical morphology only in the case of *flexible* polyelectrolytes (121,123,145). However, in the case of *very long* semi-flexible polyelectrolyte chains, such as λ DNA, spherical morphologies are predicted, presumably due to an increase in importance of the surface energy term relative to the bending energy term with an increase in the chain length (77,146). Indeed, the presence of spherical morphologies with *very long* DNAs has been confirmed experimentally with the condensation of T4 DNA (166 kb) and λ DNA (48 kb) (77). However, the higher relative population of spherical condensates was observed with λ DNA, the shorter of the two, which is not in agreement with the theory proposed by Vasilevskaya and coworkers (77). This discrepancy may be due to the fact

that T4 and λ DNA molecules were condensed in distilled water without any buffer or salt added (77). Under these solution conditions, it has been shown that DNA of approximately 3000 base pairs in length condenses partially into spherical particles or forms aggregates (147).

To investigate the length dependence of the relative population of spherical DNA condensates, we have obtained DNA samples with three different average lengths and condensed them with hexammine cobalt in the presence of a 0.5× TE buffer. Unexpectedly, the results show that spherical morphology becomes appreciable only when DNA length is decreased to an average fragment length of 494 base pairs. It was also noticed that the relative population of spheres increases with reaction time, suggesting that spheres represent the most thermodynamically stable DNA condensate morphology in samples containing short DNA fragments.

4.2. Experimental procedures

4.2.1. DNA preparation

To obtain plasmid-length DNA, Bluescript II SK- DNA (Stratagene, La Jolla, CA) was grown in DH5α cells (Life Technologies, Rockville, MD). The cells were harvested by ultracentrifugation and the plasmid DNA was isolated using the Qiagen Maxi Prep kit (Qiagen, Valencia, CA). DNA was dissolved in 1× TE (10 mM Tris, pH 7.8, 1 mM EDTA) in the final step of isolation. Next, isolated Bluescript II SK- plasmid DNA was linearized with *Hin*dIII (New England Biolabs, Beverly, MA) and will be referred to as *3kbDNA* throughout the text. Next, *3kbDNA* was then digested with the following three restriction enzymes to obtain a mixture of DNA fragments with an average DNA

fragment length of 494 base pairs: *Drd*I, *Acu*I, and *Bsa*I (New England Biolabs, Beverly, MA). 48502 base pair long λ DNA (dam-/dcm-) was purchased from Fermentas (Hanover, Maryland). All DNA samples were purified by rinsing at least five times with 1× TE using a Microcon YM-30 spin column (Amicon, Billerica, MA). After the final rinse, DNA samples were eluted with 1× TE. All DNA samples were diluted from their stock solutions to 20 μg/ml in their respective buffers. DNA concentrations were confirmed spectrophotometrically.

4.2.2. DNA Condensate preparation and analysis

All the DNA samples were diluted from a stock solution to 20 μg/ml in 1× TE. Due to the presence of complimentary 12 base overhangs at 5'-ends, λ DNA is prone to form concatomers in solution. To decrease the probability of concatomer formation prior to initiation of DNA condensation, diluted DNA samples of λ DNA were incubated at 65ºC for 10 min, after which they were immediately put on ice and re-equilibrated to room temperature. DNA condensation reactions were initiated by mixing of 20 μg/ml DNA in 1× TE with an equal volume of 200 μM hexammine cobalt chloride (Sigma-Aldrich) to yield a condensation reaction mixture 10 μg/ml in DNA, 100 μM in hexammine cobalt chloride, and 0.5× in TE buffer. DNA condensate reactions were allowed to equilibrate at room temperature for 5 min and then deposited on carbon-coated grids (Ted Pella). After 10 min, an equal volume of 2% uranyl acetate (Ted Pella) was added to the condensate mixtures on the grids. After 1 min incubation, grids were rinsed in 95% ethanol and air dried. Grids prepared for each of the DNA condensate samples were examined using a JEOL-100C transmission electron microscope (TEM). Images of DNA condensates were

recorded on film at 100,000× magnification. TEM negatives were scanned at 300 dpi into electronic format, and a graphics program was used to measure the dimensions of individual DNA toroids.

4.2.3. Temporal stability of DNA condensate morphology

For samples containing DNA fragments shorter than 700 base pairs, a time study of DNA condensation was performed. The DNA condensation reaction was initiated as described in the previous section for the other DNA samples of this study. 5 μl aliquots of each DNA condensation reaction were then taken out of the test tube at different incubation times (5 min or 60 min) and deposited on a carbon-coated grid (Ted Pella, Redding, CA). After 10 min incubation time on the grid, an equal volume of 2% uranyl acetate (Ted Pella, Redding, CA) was added to the condensate mixture. After 1 min staining, the grid was rinsed in 95% ethanol and air dried. The reaction time for each DNA condensation reaction was calculated by summing the incubation time in the test tube, the incubation time on the grid and the staining time. DNA condensates were examined by TEM as described above.

4.3 Results and discussion

4.3.1. Spherical morphology and DNA fragment length

The most commonly observed DNA condensate morphologies have been toroids and rods. The morphology ratio of toroids to rods in the condensation reaction mixture has been experimentally shown to be affected by various solution factors as well as properties of the condensing agent and DNA molecules (55-58,124). The spherical morphology has

been studied in lesser detail and thus little is known about factors that stabilize spherical morphology or what are the kinetic and thermodynamic factors are that affect the formation of the spherical condensate morphology.

DNA fragment length is one of the best studied factors known to affect morphology ratio of toroids to rods in the condensation reaction mixture (55,56). The effect of DNA fragment length has been evaluated experimentally and theoretically for the spherical morphology as well (77). The results obtained by studying condensation of T4 DNA (166 kb) and λ DNA (49 kb) DNA molecules with hexammine cobalt in distilled water have shown that long DNA molecules have an appreciable ability to condense into spherical particles as predicted by the theory of Vasilevskaya et al. (77). However, a higher relative population in the case of condensed λ DNA compared to T4 DNA is not in agreement with the theory for origin of spherical morphology proposed by the same authors (77). Thus, the appearance of the spherical DNA condensate morphology has not been explained satisfactorily.

We have condensed several DNA samples with different average fragment lengths. All DNA samples were condensed at a DNA concentration of 10 μg/ml by 100 μM hexammine cobalt chloride in a low ionic strength buffer (5 mM Tris, pH 7.8, 0.5 mM EDTA). After mixing equal volumes of DNA sample and hexammine cobalt, the reaction mixture was let to condense for a total reaction time of 16 min (Experimental procedures). First, we analyzed the morphology of condensed 48502 bp long λ DNA. λ DNA was observed to condense into toroids as well as rods (Figure 4.1A), with toroids and rods representing 92% and 8% of the condensate population, respectively. The spherical DNA condensate morphology in the sample of condensed λ DNA could not be

detected. Similarly, condensation of 2961 base pairs long plasmid DNA (*3kbDNA*) resulted in the formation of toroids and rods (Figure 4.1B) with their relative populations 88% and 12%, respectively. The spherical particles represented a negligible percentage of particles in the sample of condensed *3kbDNA* (less than 1% of the entire DNA condensate population). Next, a DNA sample with 494 base pairs average fragment length (*0.5kbDNA*) was condensed under the same solution conditions. The condensation reaction obtained with the sample containing the shortest DNA fragments exhibited the highest diversity in DNA condensate morphology. *0.5kbDNA* condensed into toroids, rods and spheres (Figure 4.1C) with toroids representing only 4% of all the counted DNA condensates, whereas rods and spheres accounted for 52% and 44% of the particles, respectively.

In contrast to previously published reports on λ DNA condensation in distilled water, we have not detected any spherical particles in the sample of condensed λ DNA. In addition, we could not confirm the increase in the population of spherical morphology with an increase in DNA fragment length that is predicted by the theory proposed by Vasilevskaya et al. (77). In fact, we observed the opposite trend. The relative population of spherical morphology was higher in the sample with the shortest DNA fragments (*0.5kbDNA*) compared to the longest DNA fragment (λ DNA) of this study.

4.3.2. A time study of particle morphology in the sample of condensed *0.5kbDNA*

The predictions by Vasilevskaya et al. were based on the thermodynamic consideration on DNA condensate morphology and its dependence on DNA fragment length. To test whether spherical particles observed in the solution of condensed *0.5kbDNA* represented

thermodynamically stable particles, we performed a time study of the stability of DNA condensate morphology.

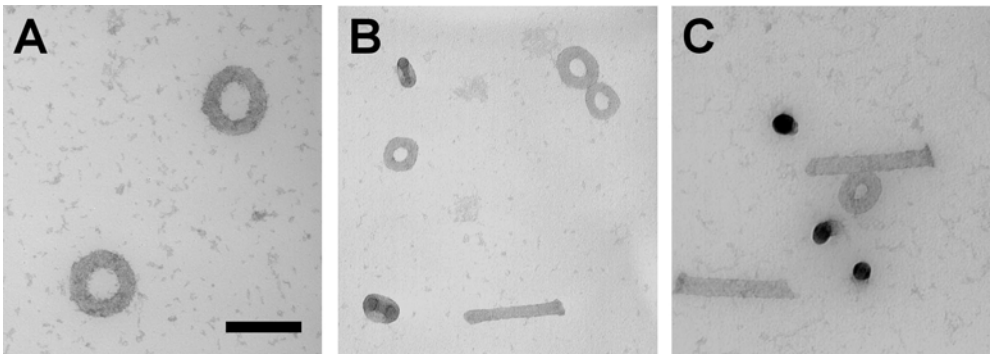

Figure 4.1 Transmission electron microscopy images illustrating the appearance of spherical condensate morphology as the average DNA fragment is decreased from 49 to 0.5 kilobase pairs. (A) Particles obtained by condensing λ DNA (49 kilobase pairs). (B) Condensates produced by *3kbDNA*. (C) Particles observed in the sample of condensed *0.5kbDNA*. Scale bar is 100 nm. Magnification is the same for all three images. All DNA samples were condensed by hexammine cobalt chloride in a condensation reaction mixture with final concentrations of DNA and hexammine cobalt at 10 μg/ml DNA and 100 μM, respectively. All condensation reactions were carried out in 0.5× TE buffer (5 mM Tris, pH 7.8, 0.5 mM EDTA).

A condensation reaction was initiated by mixing equal volumes of *0.5kbDNA* and hexammine cobalt in a low ionic strength buffer as described above. The reaction mixture was allowed to continue to incubate at room temperature for a total of 71 min, when a grid of the sample was prepared for TEM analysis of DNA condensate morphology. Similarly to what was seen after 16 min reaction time, all three major morphological forms of DNA condensates (i.e. toroids, rods and spheres) observed after 16 min reaction time were detected after 71 min (Figure 4.2). Toroids represented 5% of all counted DNA condensates, which did not represent a statistically significant increase in relative toroid population. In contrast, relative sphere and rod populations changed considerably.

Relative rod population decreased to 20%, whereas relative sphere population increased to 75% of all particles counted.

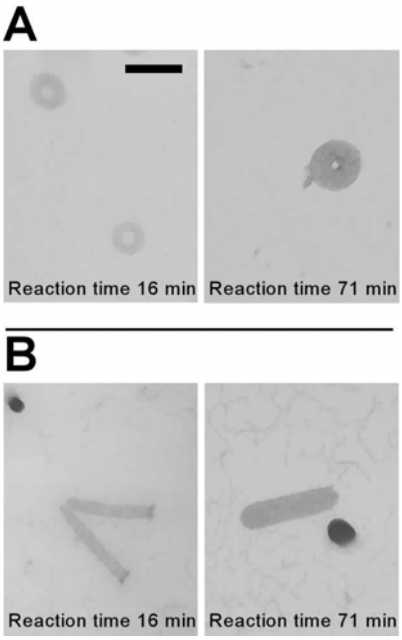

Figure 4.2 Toroids and rods in the sample of condensed *0.5kbDNA* grow between 16 min and 71 min reaction times. (A) A comparison of representative toroids obtained at 16 min (left) and 71 min reaction times (right). (B) A comparison of representative rods obtained at 16 min (left) and 71 min (right) reaction times.

4.3.3. Reaction time and the size of spherical DNA condensates

It was shown in Chapter 2 that DNA condensates grow appreciably between 16 min and 71 min reaction times. Thus, the size of DNA condensates in the reaction mixture of condensed *0.5kbDNA* was also examined. Growth of all three major morphological forms was observed. Due to a small number of toroids at both reaction times, and rods at 71 min reaction time, the average toroid and rod dimensions were not measured. Nevertheless, a qualitative comparison of the representative toroids and rods in condensed *0.5kbDNA* obtained at 16 min and 71 min reaction times shows substantial growth of both minor

morphologies (Figure 4.2). Spherical condensate dimensions were examined quantitatively by measuring the radius of the sphere. Similarly to toroids and rods, spherical condensates grew bigger with an increase in the reaction time. The average spherical condensate radii were measured to be 38 ± 3 nm at 16 min to 68 ± 4 nm at 71 min reaction time (Figure 4.3).

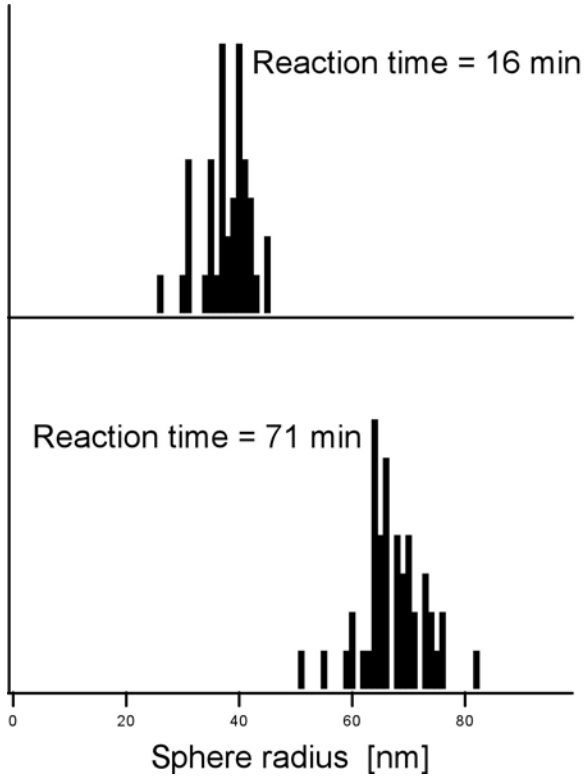

Figure 4.3 Spherical condensates grow with an increase in reaction time. The mean sphere radii of 38 ± 3 nm and 68 ± 4 nm were measured in the sample of condensed *0.5kbDNA* at 16 min and 71 min reaction times, respectively.

4.3.4. The stability of condensate morphology and DNA fragment length

The effect of DNA fragment length on the ratio of toroid to rod morphologies has been acknowledged for many years (55,56). The study presented in Chapter 3 has analyzed this effect in some detail and established that the increase in rod morphology with a decrease in DNA fragment length is due to the effect of DNA fragment length on DNA condensate nucleation. The results presented in this chapter show that a further decrease in DNA fragment length introduces the spherical morphology as one of the major morphological forms in a condensate reaction mixture. Furthermore, spheres were the only morphological form in the sample of condensed *0.5kbDNA* that increased their relative population with reaction time, which suggests that spheres may represent the most thermodynamically stable morphological form in the samples of condensed DNA fragments shorter than 500 base pairs.

Thermodynamic factors governing spherical DNA condensate morphology in the sample of DNA fragments shorter than 500 base pairs have not been analyzed experimentally or theoretically. A thermodynamic model of energy balance between bending and surface energy, as proposed by Vasilevskaya et al., predicts an opposite trend to the one observed in this study (77). As proposed in Chapter 3, DNA morphology is determined by kinetics and thermodynamics of proto-structure formation, the stability of which depends on the bending energy and number of stabilizing contacts between different segments of a DNA polymer (13). The stability of a toroid nucleation structure (i.e. proto-toroid; Figure 1.8) is thus expected to quickly decrease when DNA fragment length is decreased below an average nucleation loop circumference (76). The spherical morphology could represent an alternative to the toroid structure for short DNA

fragments in which bending energy is minimized as the number of inter-segment contacts is maximized. Additional studies of the spherical morphology in the samples of condensed short DNA fragments are necessary to evaluate factors affecting the stability of spherical morphology in greater detail.

4.4 Concluding remarks

The spherical morphology observed in the solution of *0.5kbDNA* condensed with hexammine cobalt is not the only case of spherical DNA condensate structures. A review of the literature reveals that an unexpectedly high proportion of alternative *in vitro* DNA condensation systems yields predominately spherical morphologies (53,58,144). A majority of these systems contain highly charged polycations such as, for example, polylysine. The reason why DNA condenses into spherical rather than toroidal or rod-like structures in the presence of these polycations is also not clear. Caution is needed when analyzing the thermodynamic and kinetic factors promoting the spherical morphology, as they may not necessarily be the same in the reaction mixtures containing different condensing agents (cobalt hexammine versus polycations).

5. FORMATION OF NATIVE-LIKE MAMMALIAN SPERM CELL CHROMATIN WITH FOLDED BULL PROTAMIN

5.1. Introduction

During vertebrate spermiogenesis, chromatin is dramatically reorganized in developing spermatids as histones and other nonhistone-chromosomal proteins are replaced by arginine-rich oligopeptides known as protamines (116,148). DNA packaged by protamines in mature sperm cells is transcriptionally inactive and packed at a density that approaches that of a crystalline state (112,118). The packing, or condensation, of DNA by protamines has been investigated extensively by chemical and physical studies of natural sperm chromatin, as well as by the investigation of protamine–DNA complexes prepared *in vitro* by the mixing of isolated protamines with free DNA (73,112,118,149-160). *In vivo,* protamines condense the DNA of vertebrate sperm cells into thousands of particles that vary in diameter from 50 to 100 nm (81,112,154,161-163). Each protamine–DNA particle is estimated to contain on the order of 50 kb of DNA (81). Few attempts have been made to reconstitute mammalian sperm cell chromatin using purified mammalian protamines, and reported efforts have not yield protamine–DNA complexes with DNA as highly condensed as that found in mature sperm cell chromatin (156).

Some mammalian sperm cells contain two different types of protamine, referred to as protamine I and protamine II. Protamine I is present in all mammalian sperm cells and its amino acid sequence is relatively conserved among mammals. The protamines of other vertebrates, such as fish, are similar to protamine I of mammals. Protamine II is less

conserved and is found only in a subset of mammals, including humans (116). Fish protamines and mammalian protamine I have been the focus of most studies concerning DNA condensation by protamines, primarily because protamine I is more widely distributed than protamine II, and because species from which sperm cells are most readily obtained do not contain protamine II (e.g. salmon, bull).

Mammalian protamine I is typically fifty amino acids in length. Each protamine I sequence has a central arginine-rich domain that binds in the major groove of DNA and is flanked by cysteine-rich domains at both ends (153,157,164). An alignment of mammalian protamine I amino acids sequences reveals a significant degree of conservation of the cysteine residue positions, in comparison to other sequence elements of protamine (164). The formation of intermolecular disulfide bonds between protamines bound to DNA apparently creates a network of cross-linked protamines that accounts for the greater structural stability of mammalian sperm cell chromatin in comparison to the sperm cell chromatin of species with protamines that lack cysteine residues (e.g. salmon protamine) (149). Several models have been presented to explain how protamines package DNA in sperm cells (149,165-168). However, no model has provided a complete explanation for the specific positions of cysteine residues in mammalian protamines, or for the possibility of an active role for the cysteine-rich ends in the condensation of DNA.

We have sought to determine the role of the amino- and carboxy-terminal ends of mammalian protamine I. These end domains are absent from fish protamines, and do not condense DNA as isolated peptide sequences (169). Bull sperm cells use only protamine I, and therefore bull protamine is an ideal model system for the study of DNA packing by protamine I in mammalian sperm cells. Here we report transmission electron microscopy

and light scattering studies of bull protamine–DNA complexes prepared *in vitro*. As part of these investigations, we have condensed DNA with bull protamine in the presence of varying concentrations of salt and the disulfide reducing agent, 2-mercaptoethanol. Bull protamine was found to condense DNA into spherical particles that are within the size range of protamine–DNA complexes observed in bull sperm cell nuclei. We also demonstrate that the *in vitro* formation of disulfide cross-links by bull protamine cysteines produce salt-stable protamine–DNA condensates. A comparison of results with condensates formed by the condensation of DNA with salmon protamine indicates that the cysteine-rich ends of mammalian protamine play an active role in DNA condensation, even before intermolecular disulfide bond formation. Based upon these observations, and previously reported disulfide bond assignments, we sought to determine if folded bull protamine would be expected to bind to DNA in a unique manner that promotes intermolecular disulfide bond formation. A model is presented which illustrates how the native folding of bull protamine is expected to place specific cysteine residues at positions that would allow the formation of an extensive network of intermolecular disulfide bonds in bull sperm chromatin. The ability to prepare native-like mammalian sperm cell chromatin with purified bull protamine, as described in the current work, could prove of value in further studies of protamine function, such as investigations of sperm chromatin reorganization by egg cell extracts.

5.2. Experimental Procedures

5.2.1. DNA and Protamine Preparation

Bluescript II SK- (Stratagene, La Jolla, CA) was grown in DH5α (Life Technologies, Carlsbad, CA), isolated using the Qiagen Maxi Prep kit (Qiagen, Valencia, CA) and linearized by digestion with the restriction enzyme *Hin*d III (New England Biolabs, Beverly, MA) in the buffer supplied by the manufacturer. Following digestion, the DNA buffer was changed to 20 mM sodium cacodylate, 200 μM EDTA (pH 7.5) by washing at least five times on a Microcon YM-30 spin column (Millipore, Billerica, MA). After the final rinse, DNA was resuspended from the spin column membrane in 20 mM sodium cacodylate, 200 μM EDTA (pH 7.5). DNA concentration was verified spectrophotometerically. Bluescript II SK- is 2961 bp in length, and is abbreviated as 3 kb DNA throughout the text.

Bull protamine was isolated from intact bull sperm cells (American Breeders Services, DeForest, WI) following a previously described protocol (170). Briefly, isolated native bull protamine–DNA complex was solubilized in 2.6 M urea, 1.1 M NaCl, 0.9 M guanidine hydrochloride (GuCl) and 150 mM 2-mercaptoethanol. DNA was precipitated from the solution of solubilized sperm chromatin with concentrated HCl. After dialysis of the bull protamine solution against 10 mM HCl, bull protamine was precipitated with trichloroacetic acid, washed in acetone, and dissolved in dH_2O. The bull protamine was then loaded on an equilibrated CM Sephadex C25 cation-exchange column for additional purification. The column was rinsed with water, and then 4 M NaCl. Bull protamine was eluted with 4 M GuCl. The GuCl fraction was collected, dialyzed extensively against 10 mM HCl, freeze-dried and resuspended in dH_2O. The concentration of bull protamine in

the purified stock solution was determined by comparing the intensity of naphtol blue black stained bull protamine bands on an acid urea slab gel (171) against a set of salmon protamine bands of known concentrations. Gel band intensities were determined using an AlphaImager 2200 gel imaging system (Alpha Innotech, San Leandro, CA).

The number of reduced cysteines per molecule of bull protamine in the purified stock solution was determined colorimetrically with the Ellman reagent (Pierce, Rockford, IL) according to the manufacturer's protocol in a reaction buffer containing 6.7 M GuCl and 0.2 M bicine, pH 8.0. The concentration of reduced cysteines in bull protamine stock solution was divided by bull protamine molar concentration to obtain an average number of reduced cysteines per bull protamine molecule. An aliquot of the purified bull protamine stock solution was completely reduced at 4^{o}C in 3.5 M 2-mercaptoethanol, 0.1 M Tris (pH 8), then dialyzed three times against 10 L of 10 mM HCl, and freeze-dried. The average number of reduced cysteines per fully reduced bull protamine was determined using Ellman reagent as described above. The folded state of purified bull protamine was evaluated by gel mobilities of samples of purified and fully reduced bull protamine stock solutions on an acid urea slab gel (151,171).

Salmon protamine sulfate (Sigma, St. Louis, MO) was converted to the chloride salt by dissolving in dH_2O, dialyzing against 10 L of 10 mM HCl three times and freeze-drying. The amount of salmon protamine chloride recovered was determined gravimetrically.

5.2.2. DNA Condensation

All solutions were filtered through Amicon Ultrafree-MC centrifugal filters with 0.22 μm pore diameter (Millipore, Billerica, MA) prior to use in condensation reactions. 7.5 μL of 60 μM DNA (units of base pair moles per L) in 20 mM sodium cacodylate, 200 μM EDTA (pH 7.5) was mixed with an equal volume of 4.5 μM bull protamine or 5.6 μM salmon protamine in dH_2O. The resulting condensation reaction buffer conditions (10 mM sodium cacodylate, 100 μM EDTA, pH 7.5) are referred to in the text as low ionic strength buffer. DNA was allowed to condense at room temperature for varying times (0 to 60 min), and then diluted two-fold by mixing with an equal volume of 10 mM sodium cacodylate, 100 μM EDTA (pH 7.5).

5.2.3. Electron Transmission Microscopy

Protamine–DNA condensate reaction mixtures were deposited on carbon-coated grids (Ted Pella, Redding, CA). After 10 minutes on the grid, 2% uranyl acetate (Ted Pella) was added momentarily to the condensate mixture; the grids were then rinsed in 95% ethanol and air-dried. Images of DNA condensates were recorded on film using a JEOL-100C transmission electron microscope (TEM) at 100,000× magnification. TEM negatives were scanned at 300 pixels per inch and a graphics program was used to measure the size of DNA condensates.

5.2.4. Condensate Structural Stability in High Ionic Strength Solutions

To determine the structural stability of protamine–DNA condensates in the solutions of high ionic strength, particles were prepared as described above except that in the last step,

the condensate reaction solutions were diluted two-fold with 2 M NaCl in 10 mM sodium cacodylate, 100 μM EDTA (pH 7.5). DNA condensates were imaged with TEM as described above. DNA condensate structural stability was also monitored by measuring the average intensity of light scattering of the solutions using a DynaPro MS/X dynamic light scattering instrument (Proterion, Piscataway, NJ) with a laser of wavelength 824.8 nm and a constant scattering collection angle of 90^{o}.

To determine the structural stability of protamine–DNA condensates in the presence of a disulfide bond reducing agent, DNA condensates were prepared as described above except that in the last step, the condensate solutions were diluted two-fold by adding a high salt/urea denaturing solution containing 2.6 M urea, 1.1 M NaCl, 0.9 M GuCl, and varying concentrations of 2-mercaptoethanol. The DNA condensates were monitored with static as well as dynamic light scattering.

5.3. Results and Discussion

5.3.1. Condensation of DNA by Folded Bull Protamine

The principle goal of the present study was to determine if purified bull protamine (BP) is able to condense DNA in vitro in a manner similar to that observed in native mammalian sperm cell chromatin. One of the outstanding features of BP is a high percentage of cysteine residues (Figure 5.1A). In mature bull sperm cells, four of the seven cysteines of BP participate in the formation of two intramolecular disulfide bonds (Cys6-Cys14 and Cys39-Cys47) (149). These native intramolecular disulfides constrain the amino- and carboxy-terminal domains to be folded back towards the central arginine-rich domain

(Figure 5.1B); the remaining three cysteines, Cys5, Cys22 and Cys38, form intermolecular disulfide bonds between neighboring protamine molecules in mature bull

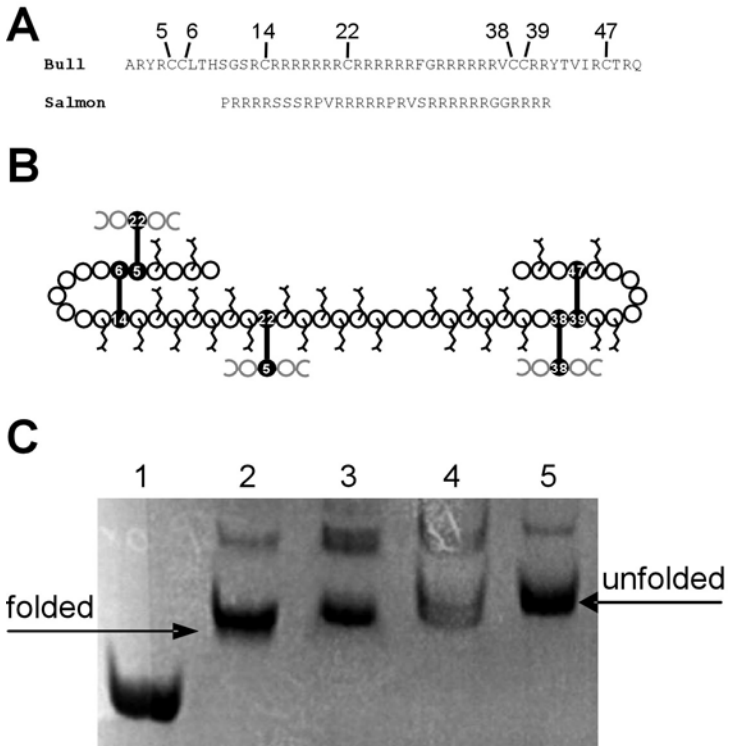

Figure 5.1 Protamine sequences used in this study, and the disulfide bond assignments of bull protamine. (A) Amino acid sequences of bull and salmon protamines. The positions of cysteine residues have been numbered. (B) Intramolecular and intermolecular disulfide bonds of bull protamine in native sperm cell chromatin (adapted from (149)). (C) PAGE analysis of protamine mobilities. Lane 1: salmine, Lane 2: purified bull protamine, Lane 3: purified bull protamine in the presence of 200 μM 2-mercaptoethanol, Lane 4: purified bull protamine in the presence of 1 mM 2-mercaptoethanol, Lane 5: fully reduced bull protamine.

sperm cell chromatin (149). In sperm cells, the intramolecular disulfide bonds are formed while protamines are bound to DNA, and before the formation of the intermolecular disulfide bonds (116). For proteins that contain multiple cysteine residues, correct disulfide bond formation is essential for the protein to fold and function properly, either as an enzyme or in a structural role (172). In order to create native-like sperm cell

chromatin in vitro, we believed it prudent to begin with BP in a folded state with pre-formed intramolecular disulfide bonds. Using BP folded with native intramolecular disulfides would greatly reduce the possibility of unnatural disulfide bond formation in our protamine–DNA condensates, and therefore more likely produce DNA condensates that resemble native sperm cell chromatin.

The folded state of purified *BP* with two intramolecular disulfide bonds was verified by Ellman free thiol analysis and polyacrylamide gel electrophoresis (Experimental Procedures). The purified *BP* stock solution was determined to have, on average, 2.6 free thiols per molecule, which is within experimental error of three free thiols per molecule. This result is consistent with the presence of two disulfide bonds per bull protamine molecule. As a control, the average number of free thiols in a fully reduced *BP* sample was determined to be seven cysteines per molecule. The folded and unfolded (fully reduced) forms of *BP* have been shown to exhibit different electrophoretic mobilities in acid-urea polyacrylamide gels (151). The greater electrophoretic mobility of purified *BP*, with respect to a fully reduced sample (Figure 5.1C), verified that the disulfide bonds in purified *BP* are two intramolecular disulfides bonds. It should be noted that some of our folded *BP* might have participated in intramolecular disulfide bond exchange during the isolation process. However, it has been shown that even completely reduced *BP* will refold to a small number of folded conformers, with the majority closely resembling the native fold of *BP* containing two intramolecular disulfides (151).

Linear 3 kb DNA was mixed with folded *BP* in a low ionic strength buffer (10 mM sodium cacodylate, 100 μM EDTA, pH 7.5) at a charge ratio of 1:1 (DNA

phosphate:*BP* arginine). The absolute concentration of DNA in the final sample was 15 μM in nucleotide base pair. Mixing *BP* with DNA resulted in the formation of spherical DNA condensate particles that showed little tendency for aggregation (Figure 5.2A). Based upon electron microscopy measurements, the average diameter of the DNA condensates obtained with *BP* was 60 nm. A spherical particle of this size corresponds to approximately twenty 3 kb DNA molecules per condensate, based upon the previously measured density of DNA packing by protamines (i.e. hexagonal close-packed with a helix-to-helix spacing of 2.7 nm) (173,174). The smallest particles observed among the *BP*–DNA condensates were approximately 22 nm in diameter (Figure 5.2A), which corresponds to the condensation of a single 3 kb DNA packed at the same density.

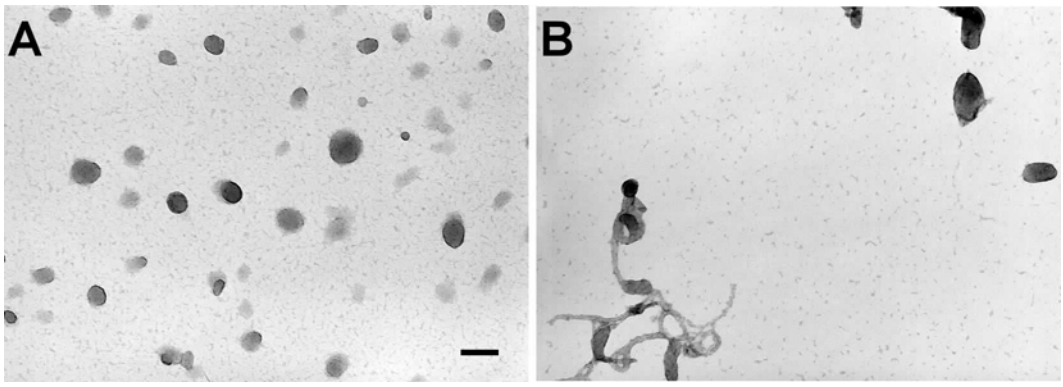

Figure 5.2 Transmission electron micrographs of condensates produced by the mixing of DNA with protamines. (A) 3 kb DNA, 60 μM in base pair, condensed by 4.5 μM folded bull protamine (*BP*). (B) 3 kb DNA, 60 μM in base pair, condensed by 5.6 μM salmon protamine (salmine). EM grids were prepared 60 min after the mixing of equal volume solutions of DNA and protamine. Additional experimental details are given in Experimental Procedures. Scale bar in *A* is 100 nm. Magnification is the same for both images.

The linear 3 kb DNA was also condensed with salmon protamine (salmine) at the same 1:1 charge ratio of DNA phosphate:salmine arginine. Salmine lacks the cysteine-

rich amino- and carboxy-terminal domains of *BP* that are a common feature of mammalian protamine I (Figure 5.1A). Thus, comparison of DNA condensates formed by *BP* and salmine can be employed as a means to investigate the effects of the cysteine-rich amino- and carboxy-terminal ends of mammalian protamines on DNA condensation. DNA condensation by salmine, under the same experimental conditions, resulted in the formation of DNA condensates with a wider diversity of particle morphologies (Figure 5.2B). Spherical particles were still the predominant morphology, however, toroidal condensates were also observed. In contrast to *BP*–DNA condensates, salmine–DNA condensates also vary more in size and exhibit a greater tendency to aggregate (Figure 5.2). The variety of salmine–DNA condensate morphologies observed in the present study is in agreement with previous reports (81,175). The lack of the cysteine-rich domains in salmine, and the similarity between the arginine-rich central domains of salmine and *BP*, suggests that the terminal domains of bull protamine play an active role in controlling particle structure. This result was unexpected, as the cysteine-rich domains of protamine I have typically been considered to provide additional stability to protamine–DNA condensates (116,149), but have not previously been suggested to have a role in controlling DNA condensate particle size or morphology.

5.3.2. Formation of Salt-Stable Bull Protamine–DNA Condensates

The structural stability of mammalian sperm cell chromatin at high salt concentrations is a hallmark of the intermolecular disulfide bonds that exist between protamine molecules, since the arginines of protamines bind to DNA through electrostatic interactions that are subject to competition by salts. High ionic strength solution conditions were used to

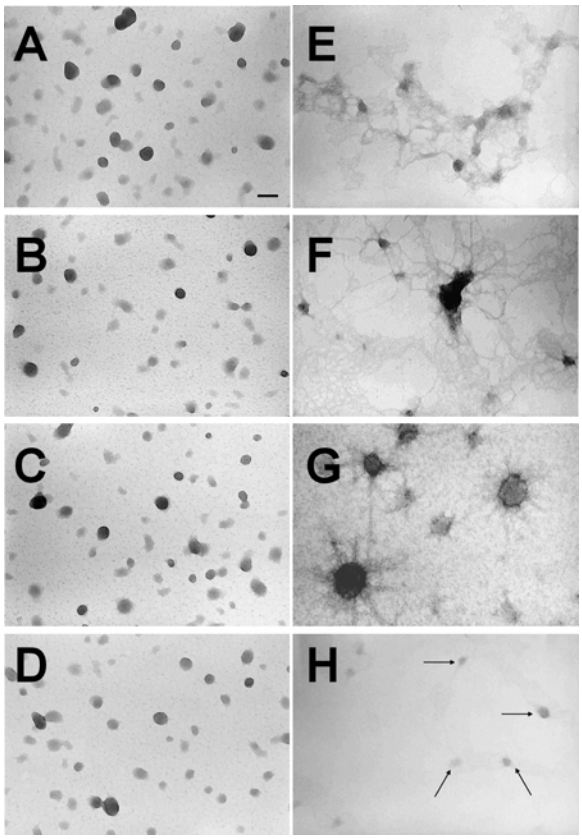

Figure 5.3 Comparison of *BP*–DNA condensates at low and high ionic strength. (A)–(D), DNA was condensed with *BP* in a low ionic strength buffer (10 mM sodium cacodylate, 100 μM EDTA, pH 7.5) and allowed to condense for different lengths of time. Condensation times for (A)–(D): (A), 5 min; (B), 15 min; (C), 30 min; (D), 60 min. (E)–(H), DNA condensed with *BP* in a low ionic strength buffer and allowed to condense for different lengths of time, followed by the addition of NaCl to 1 M. Condensation times for (E)–(H): (E), 5 min; (F), 15 min; (G), 30 min; (H), 60 min. Scale bar in *A* is 100 nm. Magnification is the same for all images.

investigate the formation of intermolecular disulfide bonds within *BP*–DNA condensates prepared *in vitro*. *BP*–DNA condensates produced in low ionic strength buffer were allowed to incubate at room temperature for different condensation times and then the ionic strength of the solution was increased to 1 M by the addition of an equal volume of 2 M NaCl. Prior to the addition of NaCl, the size and morphology of the *BP*–DNA condensates at low ionic strength did not change appreciably with increasing

condensation time (Figure 5.3A–D). However, the structural stability of *BP*–DNA condensates to high ionic strength increased with time between condensation and addition of NaCl (Figure 5.3E–H). In general, for condensation times between 5 to 30 minutes, aggregation and partial decondensation of *BP*–DNA condensates was observed (Figure 5.3E–G). After a condensation time of 60 min (Figure 5.3H), *BP*–DNA condensates were completely stable upon the addition of 1 M NaCl, as particles both maintained their shape and did not aggregate after the substantial increase in ionic strength. *BP*–DNA condensates challenged with 1 M NaCl were not as numerous on EM grids as on those produced under low ionic strength conditions (Figure 5.3). This is likely due to a lower affinity of the *BP*–DNA particles to the TEM grids at high ionic strength.

The time constant for the stabilization of *BP*–DNA condensates in 1 M NaCl was determined more precisely by measuring the average light scattering intensity of condensate solutions after the addition of NaCl to the low salt condensation reaction. As shown in Figure 5.4, the average light scattering intensity of a *BP*–DNA condensate solution in 1 M NaCl increases exponentially with condensation time. Given the 90° detection angle used to detect scattered light, the increase in average light scattering can be attributed to the increase in concentration of densely packed DNA condensates, as well as a decrease in the extent of aggregation of condensate particles (176-178). These light scattering results are perfectly consistent with the *BP*–DNA condensates shown by the TEM images in Figure 5.3. A least-squares best fit of the light scattering data with a single exponential function revealed a time constant for the stabilization of *BP*–DNA condensates to high ionic strength conditions of approximately 7 min.

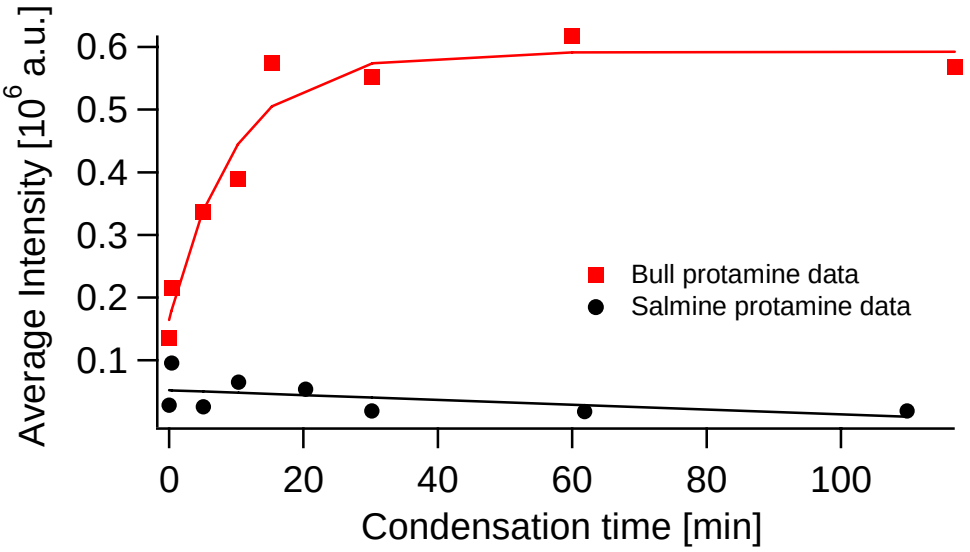

Figure 5.4 The structural stability of protamine–DNA condensates as monitored by light scattering intensity. 3 kb DNA, 60 μM in base pair, was mixed with an equal volume of 4.5 μM bull protamine (*BP*) or 5.6 μM salmine, respectively, in a low ionic strength buffer (10 mM sodium cacodylate, 100 μM EDTA, pH 7.5). The condensation reaction mixtures were allowed to incubate at room temperature for different lengths of time before the protamine–DNA solution was diluted with an equal volume of 2 M NaCl. Following salt addition, light scattering intensity of each sample was measured for 1 h. Average light scattering intensity of *BP*–DNA and salmine–DNA condensate solutions are plotted as a function of condensation time prior to the addition of 2 M NaCl.

To illustrate that the structural stability of *BP*–DNA condensates at high ionic strength was due to the cysteine-rich amino- and carboxy-terminal domains, a similar set of experiments was carried out with salmine. Salmine–DNA condensates were also prepared in the low ionic strength buffer and challenged by the addition of an equal volume of 2 M NaCl after various condensation times. Regardless of the condensation time, a low average light scattering intensity was observed for salmine–DNA solutions (Figure 5.4). Furthermore, no salmine–DNA condensates were observed by TEM (data not shown). Thus, without the cysteine-rich terminal domains, salmine–DNA complexes

prepared *in vitro* were far less resistant to changes in ionic strength than *BP*–DNA complexes prepared in an identical manner.

5.3.3. Effect of Reducing Agents on Salt-Stable Protamine–DNA Complexes

After verification that DNA condensation by *BP* produces salt-stable particles over the course of 60 min, we sought to verify that these *BP*–DNA particles could be dissociated by a protocol similar to that developed to isolate mammalian protamines. The isolation of mammalian protamines from native sperm chromatin requires a reducing agent (e.g. 2-mercaptoethanol) to reduce the intermolecular disulfide bonds of protamines, as well as a high salt/urea denaturing solution, such as 1 M NaCl, 0.8 M guanidine hydrochloride (GuCl) and 2.5 M urea (170). The addition of GuCl and urea to the 1 M NaCl solution used above is more effective than NaCl alone for the removal of protamine molecules from DNA (170). Thus, *BP*–DNA particles prepared *in vitro* should be stable in the high salt/urea denaturing solution, without a reducing agent, only if intermolecular protamine disulfide bonds have formed to an extent that is comparable to that of native sperm cell chromatin. For the next series of experiments, 3 kb DNA was again mixed with *BP* in the low ionic strength buffer at a charge ratio of 1:1 (DNA phosphate:*BP* arginine). The resulting condensates were allowed to incubate for 60 min at room temperature. Condensate reactions were then diluted with an equal volume of the high salt/urea denaturing solution. The 2-mercaptoethanol concentrations in the high salt/urea denaturing solution were varied from 0 to 275 mM for a series of identical condensate reactions. Static and dynamic light scattering were used to monitor the structural stability of *BP*–DNA condensates after the addition of the denaturing solution. For this part of the

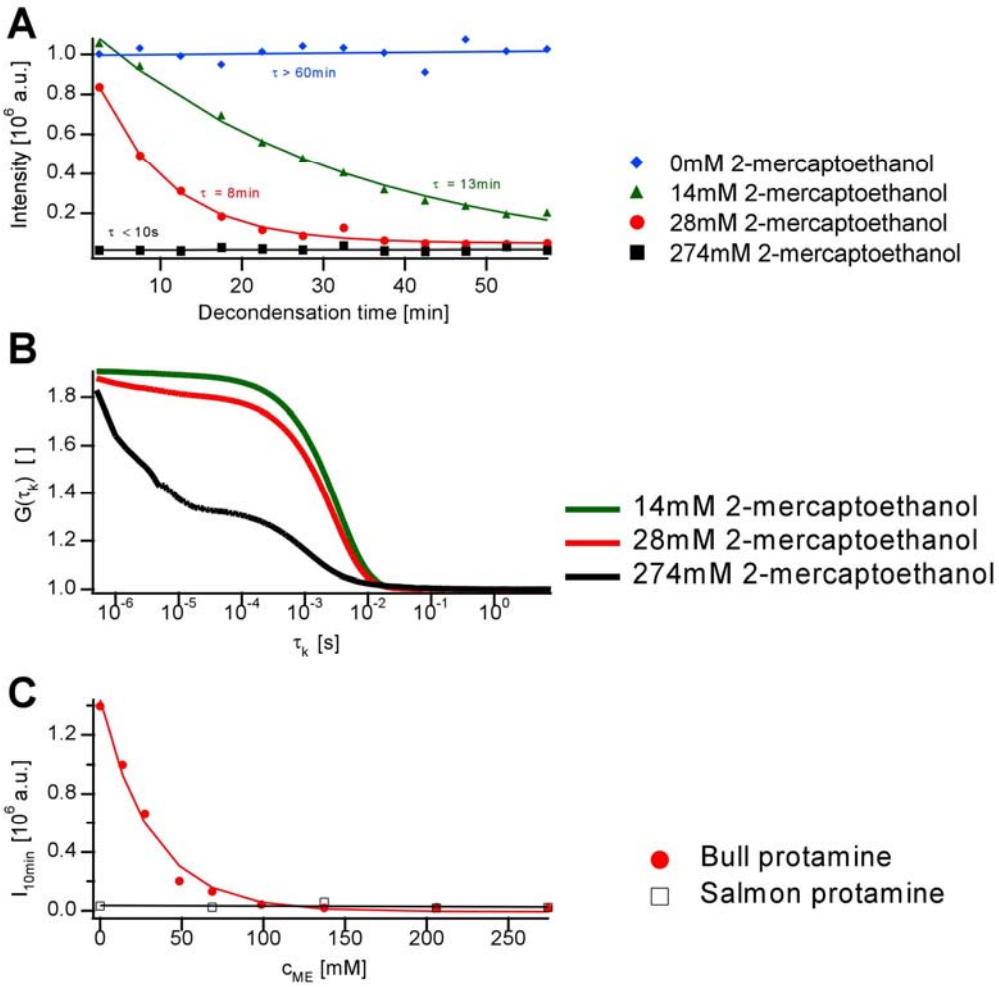

Figure 5.5 Destabilization of bull protamine–DNA (*BP*–DNA) condensates by the action of a disulfide bond reducing agent. 60 μM DNA was mixed with an equal volume of 4.5 μM bull protamine in a low ionic strength buffer (10 mM sodium cacodylate, 100 μM EDTA, pH 7.5), and allowed to condense at room temperature for 60 min, after which the condensing solution was diluted with an equal volume of a high salt/urea denaturing solution (2.6 M urea, 1.1 M NaCl, 0.9 M GuCl, and varying concentrations of 2-mercaptoethanol). (A) Average intensity decays of DNA condenensate in the presence of *BP* after the addition of denaturing solution. Concentrations of 2-mercaptoethanol varied from 0 to 275 mM. The observed time constants of decays in average light scattering intensity of *BP*–DNA condensates for each 2-mercaptoethanol concentration (τ) are given in the figure. (B) Intensity correlation functions for DNA condensate solutions in the presence of bull protamine after the addition of the denaturing solution. Concentrations of 2-mercaptoethanol were varied from 14 to 275 mM. (C) Average light scattering intensity of *BP*–DNA and salmine–DNA condensate solutions as a function of 2-mercaptoethanol concentration in the salt/urea denaturing solution. Light scattering intensity measurements were initiated during the first 10 min after the addition of the denaturing solution.

present study, TEM could not be used to follow the structural stability of *BP*–DNA condensates, as the high salt and urea concentrations of the denaturing solutions interfered with DNA visualization and grid preparation.

Similar to observations in the NaCl-induced decondensation studies described above, the addition of the high salt/urea denaturing solution with no 2-mercaptoethanol did not result in the decondensation of *BP*–DNA particles. This was confirmed by an unchanged high intensity of light scattering signal for over 60 min after the addition of the high salt/urea solution (Figure 5.5A). However, the average light scattering intensity of *BP*–DNA condensate solutions decreased exponentially with time after the addition of the denaturing solution containing the reducing agent (Figure 5.5A), which correlates directly with the decondensation of the *BP*–DNA particles (178). Decondensation of *BP*–DNA condensates by the denaturing solutions containing the reducing agent was also supported by dynamic light scattering experiments where the observed changes in the intensity correlation function demonstrated an initial decrease in diffusion coefficient and an eventual conversion to a two-step intensity correlation function as 2-mercaptoethanol concentration was increased above 200 mM (Figure 5.5B). Conversion to a two-step intensity correlation function suggests a transition to two distinct populations of DNA molecules with different diffusion coefficients (176,179), presumably swollen DNA condensates and completely decondensed DNA (178,180). The time constant for the decondensation of *BP*–DNA condensates was found to depend on the 2-mercaptoethanol concentration in the high salt/urea denaturing solution (Figure 5.5A). The dependence of the structural integrity of *BP*–DNA condensates on the presence of 2-mercaptoethanol

confirms the presence of intermolecular disulfide bonds within *BP*–DNA condensates formed *in vitro*.

For completeness, decondensation experiments using the high salt/urea denaturing solution were also carried out with salmine–DNA condensates. As expected, salmine–DNA condensate solutions gave a low light scattering intensity signal throughout the 2-mercaptoethanol concentration range studied (Figure 5.5C), with complete decondensation of salmine–DNA particles even in the absence of 2-mercaptoethanol.

5.3.4. Bull Protamine–DNA Condensates Resemble the Subunits of Bull Sperm Cell Chromatin

The DNA of bull sperm chromatin is packaged into spheroidal subunits 70 nm in diameter (112,161,181), within which DNA strands are arranged in a hexagonal close-packed lattice (174). Here we have shown that the *in vitro* complexation of folded *BP* with DNA also produces spheroid particles with an average diameter of 60 nm. Furthermore, based on volume calculations of the smallest observed condensates, we have concluded that the packing of DNA *in vitro* by *BP* is at the same density as DNA in native sperm cell chromatin (i.e., hexagonally close-packed). Thus, the morphology and DNA packing of *BP*–DNA condensates in this study are similar to those observed in sperm cell chromatin. We note that a wider variety of condensate morphologies have been previously reported for *BP*–DNA condensates prepared *in vitro* (112), which might be a result of experimental conditions being different from those of the current study (e.g. ionic strength, folded state of *BP*).

The intermolecular disulfide bonds between protamines in mammalian sperm cell chromatin must be reduced before protamines can be separated from DNA upon exposure to a high salt/urea solution (149). Balhorn and co-workers have also reported that disulfide bond-reduced *native* bull sperm chromatin regains resistance to denaturation approximately 120 min after the chromatin is removed from reducing conditions (116). We have found that our *in vitro BP*–DNA condensates are stable when exposed to a high salt/urea solution approximately 60 min after the initiation of condensation. This comparable rate of intermolecular protamine disulfide bond formation further supports our assertion that we have condensed DNA by *BP* in a manner that is very similar to the state of DNA within mature bull sperm cell nuclei (i.e. reconstituted sperm cell chromatin).

Although the *BP*–DNA condensates reported here are similar to the subunits of bull sperm chromatin, the pathway by which *BP*–DNA particles form *in vitro* is likely very different from the pathway taken by protamine and DNA during spermiogenesis. The time course of DNA condensation during spermatogenesis is measured on the order of days, and occurs in parallel with other morphological changes associated with sperm cell maturation (182-190). In contrast, *in vitro* condensation of DNA by multivalent cations is largely completed within milliseconds after a condensing agent is added to DNA in solution (120). Furthermore, the *BP*–DNA condensates of the present study have been prepared at a relatively low ionic strength (ca. 10 mM). These conditions were ultimately chosen because attempts to condense DNA with *BP* near physiological ionic strength resulted in sample aggregation, rather than condensation into discrete, nanometer-scale particles (data not shown).

BP–DNA condensates were observed to be generally smaller and more uniform than those obtained with salmine under the same solution conditions (Figure 5.2). This difference is likely due to the activity of the folded amino- and carboxy-terminal ends of *BP*, as salmine lacks these end regions and the arginine-rich DNA binding regions of *BP* and salmine are quite similar. The time constant for intermolecular disulfide bond formation in *BP*–DNA complexes is on the order of minutes in our study, whereas *in vitro* DNA condensation by multivalent cations takes place on the millisecond time scale (120). Thus, the folded ends of *BP* apparently also have an active role in determining DNA condensate morphology and size that does not involve disulfide bond formation.

5.3.5. A model for the protamine–DNA complex in bull sperm cell chromatin

Based upon the disulfide bond assignments of bull protamine (Figure 5.1B), Balhorn et al. proposed two distinct models for the *BP*–DNA complex in bull sperm cell chromatin (149). In the first model, successive *BP* molecules are wrapped around DNA in a tail-to-tail orientation; in the second model, successive *BP* molecules wrap around DNA in head-to-tail orientation (149). These two models place different restraints on how Cys5-Cys22 and Cys38-Cys38 intermolecular disulfide bonds can be formed between protamines (149). Here we present a 3D model for the tail-to-tail mode of *BP* binding to DNA and show that this model is consistent with the complete formation of intermolecular disulfide bonds within the hexagonal close-packed arrangement of DNA (174). In contrast, the head-to-tail mode of *BP* binding does not appear to be simultaneously compatible with the complete oxidation of *BP* cysteine residues and hexagonal close-packed DNA.

The two intramolecular disulfide bonds of *BP*, Cys6-Cys14 and Cys39-Cys47, maintain the amino- and carboxy-terminal ends in a folded state (Figure 5.6A). The Cys38-Cys38 intermolecular disulfide bond implies that all *BP* molecules are covalently cross-linked into tail-to-tail dimers (Figure 5.6A). The Cys38-Cys38 disulfide bond is more stable to reduction than the other intermolecular disulfide bond, Cys5-Cys22 (149). Additionally, bull sperm cell chromatin will only swell and begin dissolving at high ionic strength after the reduction of the Cys5-Cys22 bond, whereas Cys38-Cys38 cross-linked *BP* dimers can be isolated from chromatin (149). These observations are consistent with the Cys38-Cys38 bond being between two protamine molecules that are wrapped along the same duplex of DNA (i.e. an *intra*strand disulfide bond), whereas the Cys5-Cys22 bond is a cross-link between protamines on different DNA strands (i.e. an *inter*strand disulfide bond) that results in the salt-stable network of protamines and DNA. Given this assignment of inter- and intrastrand disulfide bonds, Cys38-Cys38 linked tail-to-tail dimers of *BP* must wrap around DNA in a manner that presents Cys5 and Cys22 at positions that would enable their complete participation in disulfide bond formation within a hexagonal DNA lattice.

Biophysical studies have shown that in native bull sperm cell chromatin, one protamine molecule is bound per approximately 11 bp of DNA (155). Based upon the helical twist of DNA in solution of 10.5 bp per turn (191), the binding site size for a tail-to-tail dimer of bull protamine is approximately two turns of B-form DNA. If we consider two dimers of *BP* (i.e. four protamines) wrapped around a single DNA helix, the central Cys38-Cys38 disulfide bond of both dimers would be orientated along the same

side of the DNA in order to preserve an overall binding ratio of one protamine dimer per two helical turns of DNA (Figure 5.6B).

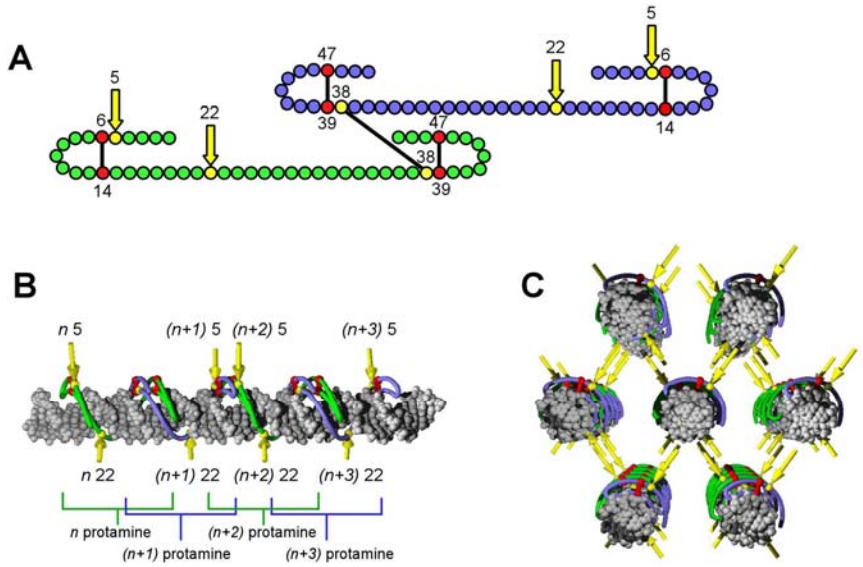

Figure 5.6 A proposed model for the protamine–DNA complex in bull sperm cell chromatin. (A) A dimer of two folded bull protamine monomers covalently linked by the Cys38-Cys38 disulfide bond. Cysteine residues involved in intramolecular disulfide bonds are depicted in red; cysteine residues involved in intermolecular disulfide bonds are depicted in yellow. The positions of Cys5 and Cys22 are emphasized with yellow arrows in all images. (B) Four turns of B-form DNA complexed by two dimers of bull protamine. Each dimer binds to two turns of the major groove of B-form DNA, with the central DNA binding domain deep in the major groove and the folded terminal ends protruding slightly out of the major groove. (C) Seven bull protamine–DNA complexes of 6*B* arranged in a hexagonal close-packed lattice.

The angle and position of the two Cys22 residues of a protamine dimer, with respect to the Cys38-Cys38 bond, can be estimated based upon the number of arginine residues in *BP* that separate Cys22 from Cys38. Poly-L-arginine binds to DNA in the major groove and wraps around the double helix a distance such that every two arginine residues interacts with a base pair of DNA, thereby producing a charge neutral DNA–poly-L-arginine complex (153,166). Salmine has also been shown to bind a length of

DNA defined by the number of arginine residues in the sequence, with the non-arginine residues acting as hinges or looped-out spacers between the runs of arginines (153,166). Here we assume a similar binding mode for *BP* to DNA, and note that residues Cys22 and Cys38 of *BP* are separated by the amino acid sequence $(Arg)_6$-Phe-Gly-$(Arg)_6$-Val (i.e. twelve Arg) (Figure 5.1A). Thus, the two Cys22 residues of a *BP* dimer bound to DNA would each be separated from the Cys38-Cys38 disulfide bond by six base pairs, or approximately 3/5 of a DNA helical turn, up or down stream from the point of protamine dimerization, respectively (Figure 5.6B). The position of Cys14 on DNA-bound bull protamine can be used to estimate the position of Cys5, because Cys14 forms a disulfide bond with Cys6, and Cys6 is adjacent to Cys5 (Figure 5.6A). Cys14 is separated from Cys22 of the same protamine by $(Arg)_7$, which corresponds to an additional 1/3 of a DNA helical turn (i.e. 3.5 bp) from the Cys38-Cys38 disulfide bond. Using this estimated position of Cys14 for that of Cys5, our model predicts that the Cys5 residues of multiple *BP* dimers bound to a DNA helix will be located on one side of the DNA helix, whereas the Cys22 resides will be located on the opposite side of the helix (Figure 5.6B).

Seven copies of our protamine-bound DNA model were combined to create the 3D hexagonal lattice shown in Figure 5.6C. The close proximity of Cys5 and Cys22 residues from protamines of neighboring DNA strands (indicated by yellow arrows) is compatible with the complete formation of Cys5-Cys22 disulfide bonds (73,149,174,181). Although a number of different models have previously been proposed for the packing of DNA by mammalian protamines (149,165-168), we believe that the model presented here is the first to account for complete cysteine oxidation within a hexagonal close-packed lattice of DNA. The proposed model is also consistent with the

high structural stability of the native DNA–bull protamine complex (170), since the protamine molecules wrapped around a particular DNA strand are covalently bound to the protamines of neighboring DNA strands through an extended network of Cys5-Cys22 disulfide bonds. We note that the *in vitro BP*–DNA complexes formed and characterized in the current work may have a less regular arrangement of *BP* along DNA (i.e. both tail-to-tail and head-to-tail) than native sperm chromatin, because the condensation of DNA by *BP in vitro* lacks participation by other sperm cell components that may be required to achieve such a regular structure.

5.4. Concluding Remarks

Protamines are known to exhibit substantial sequence variation even between closely related species (192-194). Nevertheless, the alignment of mammalian protamine I amino acid sequences reveals a relative conservation of the cysteine residue positions with respect to other sequence elements (116,164). This would suggest that similar disulfide bond networks are possible in sperm chromatin of other mammals that contain only protamine I. It remains to be determined if the model proposed accurately describes the disulfide bond network in mammalian sperm cells that also contain protamine II, since the disulfide bond assignment for a species containing protamine II has not yet been determined.

6. SINGLE-ANGLE LIGHT SCATTERING AND DNA CONDENSATION

6.1. Introduction

Light scattering refers to a particular form of an interaction of an electro-magnetic wave with a particle, where an incident light electric field causes changes in the particle polarizabilities that in turn induce dipoles. The fluctuations of the induced dipoles results in the emission of scattered light (176,195,196). There are two major light scattering techniques: static and dynamic light scattering. Static light scattering enables one to determine particle molecular weight by measuring the scattered light intensity emitted from the particle (195). On the other hand, dynamic light scattering is an experimental technique that enables a calculation of particle hydrodynamic radii by measuring time correlations of scattered light intensity (176). Due to its ability to measure particle molecular weight and size, light scattering represents a powerful set of techniques for the kinetic and thermodynamic studies of processes involving particle growth or any other particle conformational transitions that result in a change in its mass and size (e.g. polymerization, crystallization, protein folding, inter-particle interactions, polymer phase transitions, DNA condensation) (197-207).

The interpretation of light scattering data is straightforward in the systems containing monodispersed small particles. Similarly, processes involving a transition from one monodispersed state to another are also readily studied by light scattering. However, the analysis of large and polydispersed particles requires, in principle, a

multiangle static and/or dynamic light scattering. Nevertheless, a careful analysis of single-angle light scattering data in conjunction with complimentary imaging techniques (e.g. atomic force microscopy, transmission electron microscopy) can serve as a suitable alternative (198,203).

6.2. Static light scattering – An analysis of light scattering intensity

Static light scattering measures an average light scattering intensity that is emitted from an ensemble of particles, which can be related to the molecular weight and size of the particles. A clear understanding of the parameters affecting measured light scattering intensity is a prerequisite for a correct analysis of static light scattering data. In the following paragraphs, a discussion of light scattering from different types of particles is presented in order to illustrate all the parameters that can affect the absolute value of light scattering intensity.

6.2.1. Particles in the gas phase

The simplest example of light scattering is observed in a gas phase at low pressure (Figure 6.1). In the case of unpolarized light, a normalized density of light scattering intensity is given by the following equation (195):

$$\frac{i_\Theta}{I_0} = \frac{2\pi^2}{\lambda^4 N_A} \cdot \frac{Mc}{r^2}\left(\frac{dn}{dc}\right)^2 \left(1+\cos^2\Theta\right) \qquad (6.1)$$

where i_Θ is the density of scattered light intensity, I_0 is the density of incident light intensity, λ is the wavelength of incident light, N_A Avogadro number, M is molecular

weight of the particle, *c* is the particle mass concentration, *r* is the distance between the particle and the point of scattered light detection, *n* is refractive index, and Θ is the angle between the direction of the incident light and the line of scattered light detection. It is apparent from the equation 6.1 that molecular weight of the particle can be obtained from a single-angle SLS experiment only if the concentration of the particles is known.

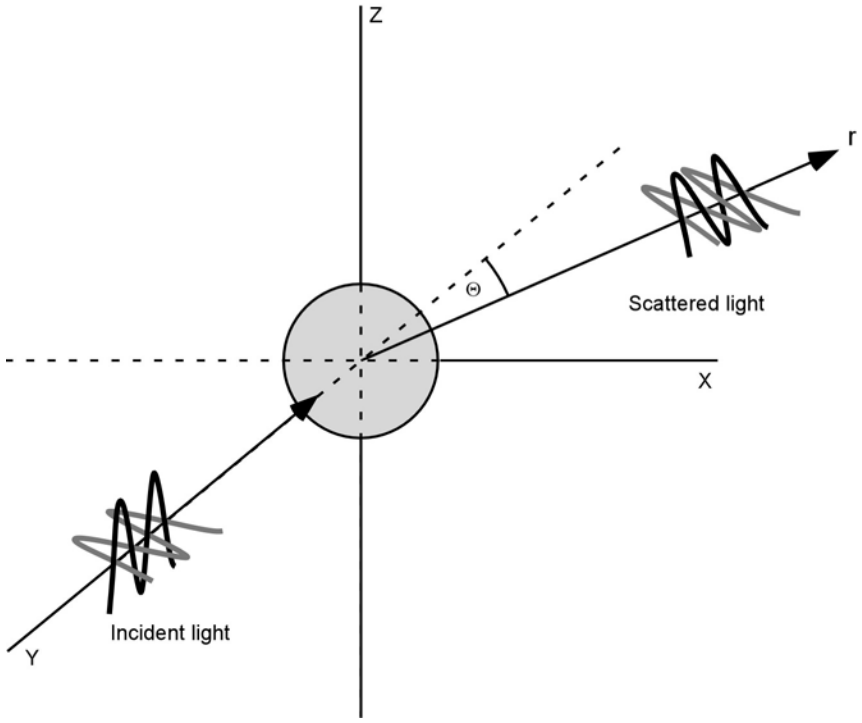

Figure 6.1 Scattering of unpolarized light on a particle in a gas phase. The incident light is coming from the y-direction. The scattered light is emitted in all directions. For clarity, an emission of scattered light in only one direction is shown. The observed light scattering intensity from a given particle depends on the position of the detection point (i.e. *Θ* and *r*).

If the wavelength of the incident light is much bigger than the average spacing in a crystal lattice, light scattering cannot be observed in the case of solids that are

composed of particles arranged in a regular repetitive lattice due to a complete destructive interference between light scattered from different particles (195).

6.2.2 Small solute particles in a two-component solution

In an ideal dilute solution of a single type of solute particles, nonpolarized light scattering intensity from the solute particles can be derived using equation 6.1. By defining a solute excess polarizability in respect to the polarizability of a solvent molecule, the light scattering intensity per unit volume can be described as follows:

$$\frac{i_\Theta}{I_0} = \frac{2\pi^2}{\lambda^4 N_A} \cdot \frac{Mc}{r^2} \cdot n_0^2 \left(\frac{dn}{dc} \right)^2 \left(1 + \cos^2 \Theta \right) \tag{6.2}$$

where n_0 is the solvent refractive index (195). A comparison of light scattering intensity of a particle in the gas phase (equation 6.1) and a solvated particle (equation 6.2) reveals that the refractive properties of the solvent affect the light scattering efficiency of the solute. Any light scattering experiment in a solution thus requires specification of the solvent refractive index.

In polymer science, a modified equation 6.2 is used for non-ideal solutions:

$$\frac{Kc}{R_\Theta} = \frac{1}{M} + 2Bc \tag{6.3}$$

where R_Θ is a Rayleigh ratio that contains all the terms from equation 6.2 related to Θ, i_Θ, and I_0 as well as r; K contains all the remaining constants from equation 6.2; B is the

second viral coefficient (195). Molecular weight of the particle can then be determined with a single-angle light scattering experiment by extrapolating values for Kc/R_Θ to zero solute particle concentration limit.

6.2.3. Light scattering interference on large particles

The equations described in the previous paragraphs for gas and small solute particles in a dilute solution do not describe light scattering from particles with dimensions comparable or greater than the wavelength of the incident light (> λ/20). Due to their relatively large dimensions, the incident light can scatter at multiple locations within the same particle. The relative proximity of scattering events causes interference of scattered light from different locations within one particle, which can affect the total light scattering intensity (Figure 6.2).

It can be seen from Figure 6.2 that at zero scattering angle, no interference is observed. It is thus convenient to define a relative light scattering intensity:

$$P(\Theta) = \frac{i_\Theta}{i_0} \tag{6.4}$$

where $P(\Theta)$ is the relative light scattering intensity at detection angle Θ, and i_0 is the density of scattered light intensity at zero angle of detection. If the angle of detection approaches zero, then, the relative light scattering intensity can be shown to be determined by:

$$P(\Theta) = 1 - \frac{16\pi^2}{3\lambda^2} R_g^2 \sin^2 \frac{\Theta}{2} \tag{6.5}$$

where R_g is the particle radii of gyration (195). In the solution of large particles, light scattering measurements carried out at detection angles below 180^o will then result in intensities that will be lower compared to the intensities scattered from a small particles with the same molecular weight.

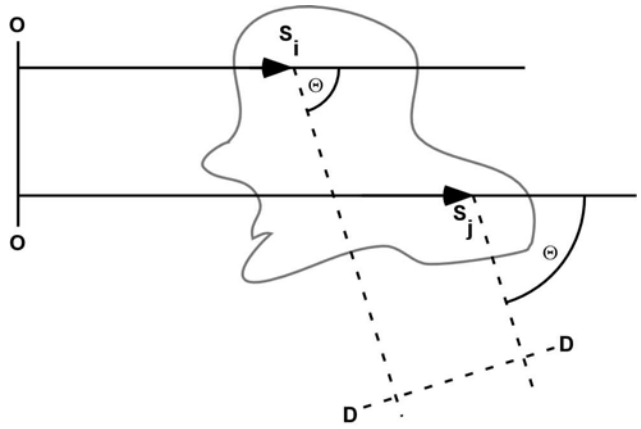

Figure 6.2 Light scattering from a large particle. Two incident light photons *i* and *j* start at the same point of origin (O) with their pathways indicated by the arrows. Photons *i*I and *j* get scattered at points S_i and S_j, respectively, which are located on the same particle. The scattered photons are then detected at point D. A distance traveled by the photon *i* (OS_iD) is not equal to the distance traveled by the photon *j* (OS_jD), which results in the light interference that affects the total light scattering intensity coming from a large particle. The arches indicate the angle of detection Θ that is identical for both scattering points.

Kc/R_Θ ratio for large particles can then be obtained by the following expression (195):

$$\frac{Kc}{R_\Theta} = \left(\frac{1}{M} + 2Bc\right) \cdot \frac{1}{P(\Theta)} = \left(\frac{1}{M} + 2Bc\right)\left(1 + \frac{16\pi^2}{3\lambda^2} R_g^2 \sin^2 \frac{\Theta}{2}\right) \tag{6.6}$$

The molecular weight of a large particle can therefore not be obtained from a dependence of single-angle light scattering intensity on the particle concentration alone. In the case of large particles (i.e. > λ/20), a multi-angle light scattering experiments is required as molecular weight of the particle can be obtained only after extrapolating Kc/R_Θ values to zero particle concentration as well as zero angle of detection on a plot that is known as a Zimm plot (195).

6.2.4. Single-angle static light scattering and DNA condensate solution

Single-angle light scattering techniques have been often applied in the studies of DNA condensation since the addition of a multivalent counterion to a solution of free DNA results in a formation of a condensed particle with an increased light scattering capacity compared to the free DNA. However, the large dimensions of DNA condensates demand a cautious analysis of light scattering intensity measurements.

Most of the light scattering instruments designed for biological applications use a laser source with a wavelength in the visible part of the spectra (400 nm – 780 nm). As has been shown in the previous chapters, particle size usually observed in DNA condensation reaction mixtures on average exceeds the size limit below which interference of scattered light does not have to be considered. Even average dimensions of primary condensed particles (i.e. condensates that form at reaction times shorter than 41 min as shown in Chapter 2) are large enough to bring about a decrease in light scattering intensity due to scattered light interference (54). In the later stages of DNA condensation reaction (i.e. reaction times longer than 41 min; Chapter 2) large clusters and aggregates prevail which should only enhance the effect of the interference of

scattered light. Bloomfield has theoretically evaluated this effect for the case of clustered DNA condensates (177), and shown that at the most common detection angle of 90^{o}, a cluster of 9 DNA condensates will result in a 90% reduction of light scattering intensity relative to 9 unclustered DNA condensates (177). Such a drastic decrease in light scattering intensity can lead to a substantial underestimation of particle size and molecular weight.

An illustrative experimental example of the effect of light scattering interference on DNA condensates is a titration study, where a 2961 bp long plasmid DNA was condensed with a trivalent spermidine at different charge ratios. The light scattering intensity was measured at a single scattering angle of 90^{o}. Figure 6.3A shows average scattered light intensities as a function of spermidine concentration at a constant plasmid DNA concentration. A cooperative increase in light scattering intensity observed at spermidine concentration below 500 μM (Figure 6.3A) indicates an increase in particle scattering potential that suggests the onset of DNA condensation. This would be in agreement with previously published data that suggest an onset of DNA condensation in a similar spermidine concentration range (208,209). However, TEM images of particles obtained with spermidine concentrations at Point 2, and Point 3 suggest that the observed cooperative increase in light scattering intensity is due to a decrease in particle dimensions (i.e. decreased scattered light interference) (Figure 6.3B). Furthermore, the second cooperative transition in the scattered light intensity between Point 4 and Point 5 could be interpreted as decondensation of DNA particles. However, the representative TEM images of condensation reactions obtained with spermidine concentrations at Point 4, Point 5 and Point 6 reveal that the observed decrease in the light scattering intensity

could be due to the increased interference of scattered light on aggregated DNA condensates.

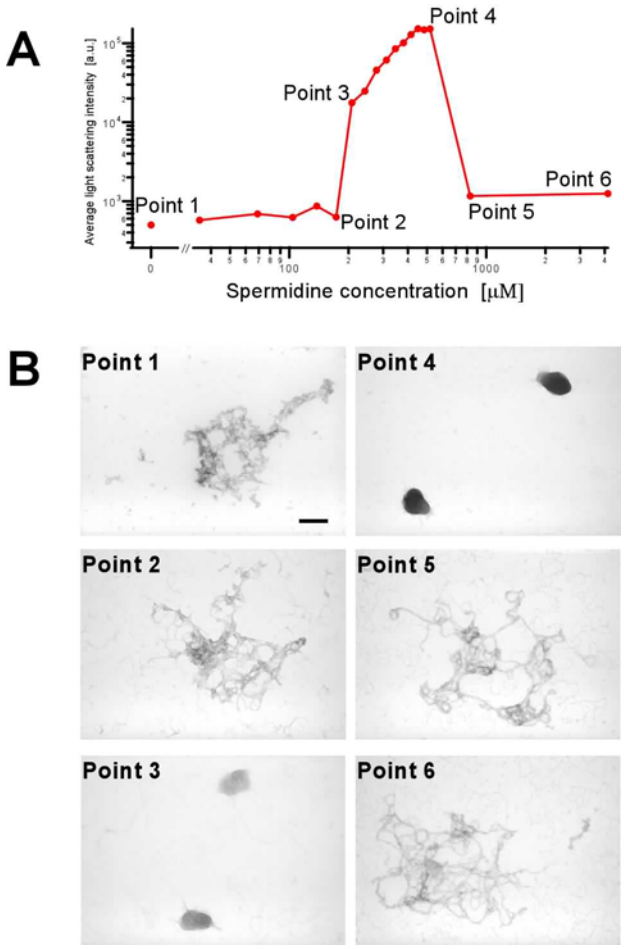

Figure 6.3 Change in the light scattering intensity can be due to DNA aggregation rather than decondensation of particles collapsed DNA. 2691 base pair long plasmid DNA at 10 μg/ml was condensed with spermidine at different concentration of the condensing agent in 1 mM Cacodylate buffer, 100 μM EDTA, pH = 7.0. DNA condensation mixtures were incubated at room temperature for 5 min before investigating them with static light scattering and transmission electron microscopy (TEM). (A) Average light scattering intensity of DNA condensate solutions as a function of spermidine concentration. Two cooperative transitions in the light scattering intensity can be observed: between Point 2 and Point 3 as well as between Point 4 and Point 5. (B) TEM images of DNA condensates obtained in the solutions indicated in panel A. The scale bar in the TEM image for Point 1 in panel B represents 100 nm.

The cooperative transitions in scattered light intensity observed in DNA condensate solutions cannot be interpreted unambiguously as either an onset of DNA condensation or decondensation of DNA particles. As the comparison of single-angle SLS and TEM data in Figure 6.3 shows, a change in scattered light intensity can be due to a change in particle size as predicted by the light scattering theory (177,195). Furthermore, it appears that a combination of single-angle SLS and TEM techniques does not enable an unambiguous determination of the onset of DNA condensation. A TEM image of a solution containing DNA in the absence of spermidine shows large particles (Figure 6.3B). These particles must have formed during the TEM grid preparation as free DNA is expected to be in an uncondensed state in the solution devoid of any multivalent cations. To overcome these shortcomings of single-angle SLS and TEM, a dynamic light scattering is often used to determine particle size in its solution state by analyzing time correlations of scattered light intensity instead of measuring the absolute light scattering intensity (176).

6.3. Dynamic light scattering and particle size

Static light scattering measures the average light scattering intensity of an ensemble of particles, which has been shown above to be unreliable indicator of the onset of DNA condensation due to interference of scattered light on DNA condensates that are comparable in size to the wavelength of incident light. Alternatively, the onset of DNA condensation can be determined by analyzing time correlations of scattered light intensity obtained with dynamic light scattering (DLS).

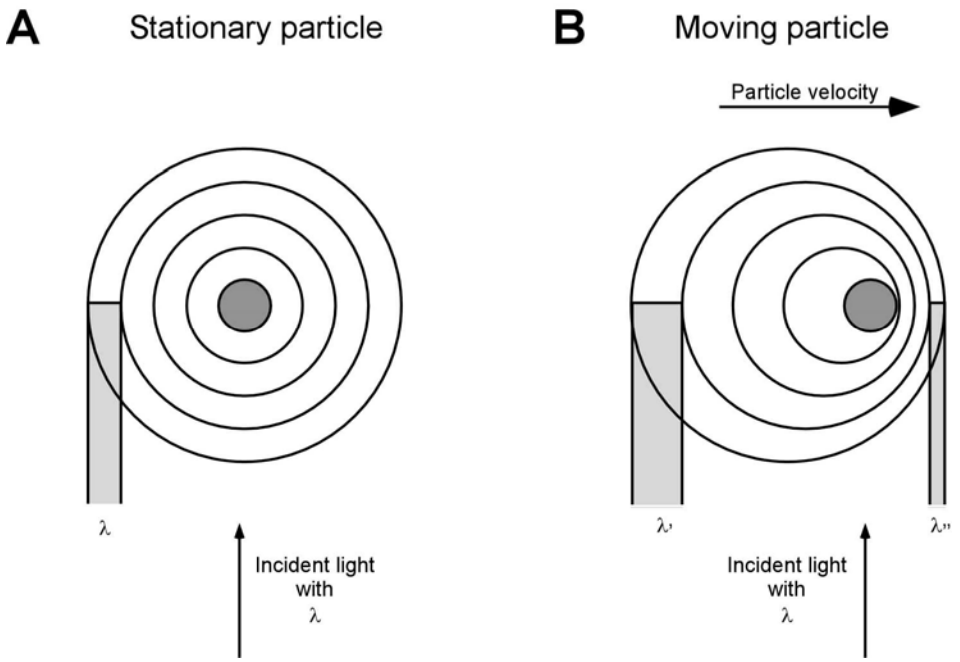

Figure 6.4 Doppler effect in light scattering on a moving particle. (A) The wavelength of the light scattered on a stationary particle is unchanged compared to the wavelength of the incident light. (B) Due to the Doppler effect, scattering of the incident light with a wavelength λ on a moving particle results in a shift in the wavelength. The value of the shift depends on the position of the detector.

6.3.1. Theory of dynamic light scattering

Random Brownian thermal motion of particles affects scattered light in several ways (176,196,199). First, a wavelength shift by the Doppler effect of the scattered light in respect to incident light can be observed due to random thermal motions (Figure 6.4) (199). In addition, fluctuations in light scattering intensity from a small solution volume segment can be observed that are the result of fluctuations in local concentration due to random Brownian thermal motions of particles in and out of the volume segment (Figure 6.5) (196). Brownian thermal motion of particles can thus be studied by measuring either the frequency shift or the fluctuations in scattered light intensity, which enables one to conveniently measure the rate of particle random thermal motion (i.e. diffusion

coefficient) (176,196). The majority of the modern dynamic light scattering instruments measures the diffusion coefficient by analyzing fluctuations in scattered light intensity, as wavelength shifts in scattered light are often too small to be measured accurately (176).

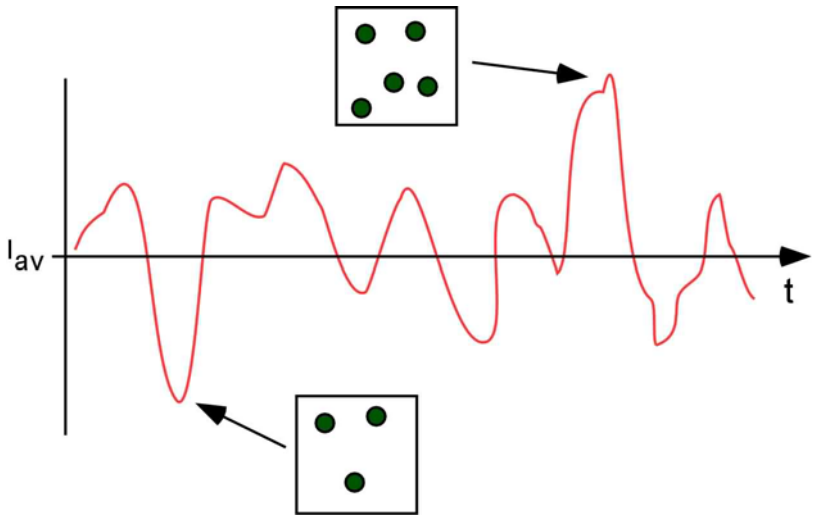

Figure 6.5 Fluctuations in light scattering intensity coming from a small solution volume segment are due to local fluctuations in particle concentration. Light scattering intensity detected in a small solution volume segment fluctuates around its average value, I_{av}. Squares represent the solution volume segment, where particles are freely diffusing in and out by random Brownian thermal motion.

The frequency of fluctuations in scattered light intensity will depend on how fast the solute particles move in and out of a small volume segment. The most common way of analyzing these fluctuations is by autocorrelation analysis, where a deviation of the light scattering intensity from the average light scattering intensity at time *t* is defined as:

$$\Delta I(t) = I(t) - I_{av} \tag{6.7}$$

where $\Delta I(t)$ is the light scattering intensity deviation at time t, $I(t)$ is the absolute light scattering intensity at time t, and I_{av} is the average light scattering intensity. The final result of the autocorrelation analysis is an autocorrelation function, $G(\tau)$, which evaluates correlations between light scattering deviations at different times t that are separated by the same value of correlation time τ:

$$G(\tau) = \int_0^\infty \Delta I(t) \cdot \Delta I(t+\tau) dt \tag{6.8}$$

At large τ values, the value of $G(\tau)$ converges to zero because the product $\Delta I(t) \cdot \Delta I(t+\tau)$ will be positive as often as negative. At short τ values, the $G(\tau)$ will be positive, because $\Delta I(t)$ and $\Delta I(t+\tau)$ will usually be of the same sign. Alternatively, scattered light intensities rather than their diviations from the average value can be correlated. The resulting autocorrelation function can be expressed by an equation similar to equation 6.8; however, it is usually normalized to converge to a value of 1 at longer correlation times. An example of such an autocorrelation function of a sample containing nanoscale particles is given in Figure 6.6. The function has a characteristic sigmoid shape. At short correlation times, the autocorrelation coefficient has a value close to 2, indicating a strong correlation of scattered light intensities. The region of strong correlation is followed by a region of decreased correlation, where the cooperative decrease in autocorrelation coefficient takes place. Finally, the value of the autocorrelation coefficient decreases to the value of 1 at long enough correlation times, where scattered light intensities are no longer correlated.

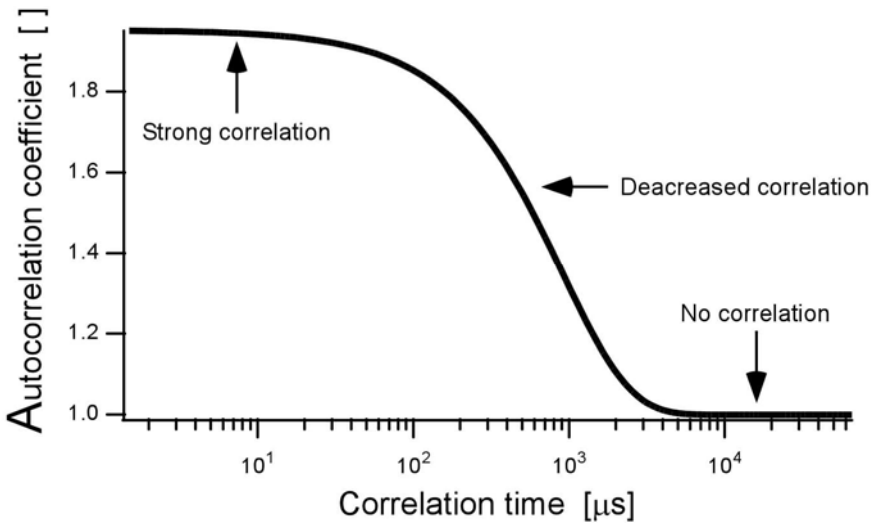

Figure 6.6 An example of a typical scattered light autocorrelation function for a nanoscale particle. Regions of strong, decreased and no correlation are indicated.

Regardless of the way by which the light scattering intensity autocorrelation function is obtained, it can be shown that the $G(\tau)$ value decays exponentially with τ. The decay rate depends on the diffusion coefficient of the particle:

$$\ln G(\tau) = \ln G_0 - \left(\frac{8\pi^2 n^2}{\lambda^2} \sin^2 \frac{\Theta}{2} \right) D\tau \tag{6.9}$$

where D is particle diffusion coefficient. It follows from equation 6.9 that the mid point of the cooperative decrease in autocorrelation coefficient (Figure 6.6) depends on the diffusion coefficient of the particle. In the dynamic light scattering experiment, the diffusion coefficient is obtained by fitting the experimental autocorrelation function to equation 6.9. In case of a spherical particle, the hydrodynamic radius can then be calculated using the Stokes-Einstein equation:

$$R_h = \frac{kT}{6\pi\eta D} \tag{6.10}$$

where R_h is spherical particle hydrodynamic radius, k is Boltzman constant, T is absolute temperature, η is the solvent viscosity.

Sometimes, a two-step autocorrelation function can be observed. An example of such a function is shown in Figure 5.5 in Chapter 5. This is indicative of a sample with structures of appreciably different diffusion coefficients. The autocorrelation function of such a sample can be written as a sum of weighted autocorrelation functions of individual structures (179). The height of an individual step in the two-step autocorrelation function depends on the size as well as the concentration of the particles that give rise to a particular step in the autocorrelation function (179).

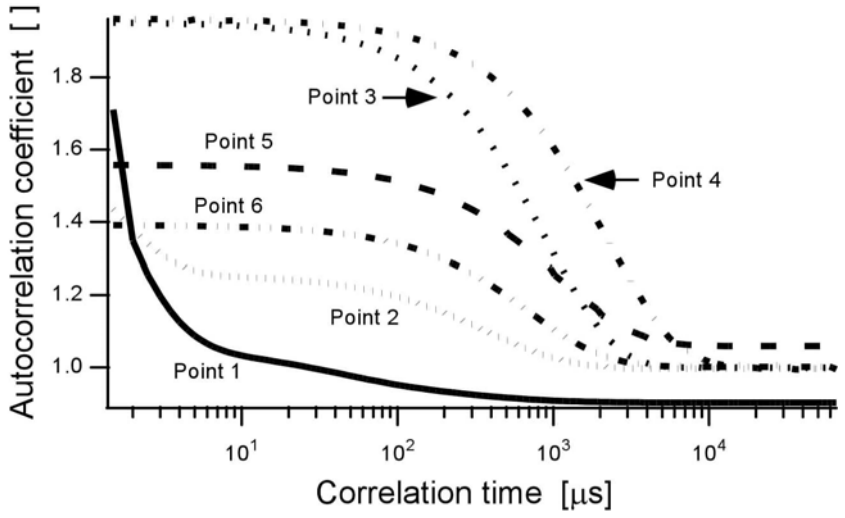

Figure 6.7 Light scattering intensity autocorrelation functions for free DNA and DNA condensate solutions. The autocorrelation functions are marked with abbreviations abbreviations for free DNA and DNA condensate solutions (i.e. Point 1, Point 2, Point 3, Point 4, Point 5, and Point 6) that are identical to corresponding reaction mixtures in Figure 6.3. Dynamic light scattering data was obtained by measuring light scattering intensities at detection angle of 90o with a wavelength of the incident light 824.8nm.

6.3.2. Investigation of DNA condensation with dynamic light scattering

As discussed above, dynamic light scattering enables a determination of particle hydrodynamic radii based on fluctuations in scattered light intensity. This provides an experimental determination of the DNA state in the presence of the condensing agent more accurately in the sample of low light scattering intensity (e.g. low spermidine concentration range; Point 2 in Figure 6.3) as well as samples where TEM grid preparation may interfere with DNA state (e.g. solution of free DNA; Point 1 in Figure 6.3).

The position of the cooperative transition in the free DNA autocorrelation function (the curve marked 'Point 1' in Figure 6.7) suggests that particles in the solution of free DNA do not exceed a few nanometers. This low hydrodynamic radius of plasmid length DNA is much smaller than the calculated value of approximately 90 nm (54). The inability of single-angle DLS at 90^{o} to accurately measure R_h of free DNA is not unexpected, as the diffusion coefficient of free DNA is difficult to measure except at low scattering angles due to the contributions of internal motions (210,211). Nevertheless, free DNA autocorrelation function is indicative of an absence of any solid particles (e.g. DNA condensates) and clearly shows that the low average light scattering intensity measured for free DNA (Point 1 in Figure 6.3A) is indeed due to uncondensed DNA. The aggregates observed in the sample of free DNA when investigated by TEM images ('Point 1' image in Figure 6.3B) results during the process of TEM grid preparation which includes uranyl acetate staining and a final wash in ethanol, that are factors that contribute to DNA condensation.

DLS, SLS and TEM do not necessarily give contradicting results for most experiments. For example, the presence of aggregates in the case of DNA condensation with 173 μM spermidine as indicated by static light scattering and TEM (Point 2 in Figure 6.3A and 'Point 2' image in Figure 6.3B) is confirmed by the observed cooperative transition in autocorrelation function of the same solution (curve marked 'Point 2' in Figure 6.7). Similarly, an agreement between the three techniques can be seen in the case of DNA condensate reaction mixtures marked Point 3 – Pont 6 in Figure 6.3, and 6.7.

It should be noted that the dynamic light scattering technique is not entirely immune to the effect of the scattered light interference in large particles. A comparison of the positions of the cooperative transition in the value of the autocorrelation coefficient would suggest that the particles in DNA condensation mixtures with 830 μM spermidine (curve marked 'Point 5' in Figure 6.7) are smaller than the particles in DNA condensation mixture with 512 μM spermidine. A comparison with the respective TEM images contradicts this conclusion. This underestimation of particle dimensions by dynamic light scattering is predicted by a theoretical analysis of the dynamic light scattering signal by Bloomfield (177).

6.4. Concluding remarks

Single-angle light scattering techniques have been discussed in this chapter. It has been shown that an investigation of DNA condensation by a single technique does not necessarily allow one to analyze the system completely. Thus, in principle, a combination of single-angle static and dynamic approach accompanied by a microscopic technique

such as TEM is the most appropriate way to study a transition from a free to a condensed DNA state.

Most of the work reported in the previous chapters has involved analysis of DNA condensate size and morphology by TEM alone (Chapters 2, 3, 4, 5). For these and similar studies, a microscopy technique is still the most appropriate experimental tool as DNA condensate size and morphology are not accurately evaluated by either of the light scattering techniques. However, single-angle static and dynamic light scattering in the studies of DNA condensate size and morphology were used to confirm the initial onset of DNA condensation as a function of an independent experimental variable (e.g. condensing agent concentration, temperature, and ionic strength).

7. CONCLUSIONS AND FUTURE WORK

7.1. Misbehavior of DNA condensation model system

Various model systems have been used to study *in vitro* DNA condensation experimentally (13,14,43), and condensation of plasmid DNA in the presence of the trivalent counterion hexammine cobalt has been one of the most commonly used. We have used hexammine cobalt to study the mechanism of DNA condensation by examining DNA condensate size and morphology as a function of reaction time and solution conditions, as well as DNA length and structure. One of the major conclusions of the work presented in this dissertation is that DNA condensate morphology and size were previously not studied under equilibrium conditions. Temporal studies of DNA condensate morphology and size have shown that neither of these major characteristics reaches their equilibrium states within minutes, but rather on the order of hours. In addition, relative equilibrium populations of particular morphologies and condensate size have been shown to depend on thermodynamic as well as kinetic factors governing DNA condensate nucleation and growth.

The results presented in this dissertation have implications regarding the experimental evaluation of any theory on polyelectrolyte condensation involving *in vitro* DNA condensation as a model system, since most of the theories have treated condensation as either strictly under kinetic or strictly under thermodynamic control (13,21,75,77). Consequently, using DNA condensation solution data to evaluate

exclusively thermodynamic or kinetic theoretical models describing DNA condensation equilibrium can potentially be misleading.

Condensation of DNA of varying fragment lengths was used to analyze qualitatively the effect of nucleation kinetics and thermodynamics on the condensate morphology. It has been shown that the kinetics of nucleation as well as monomolecular condensate stability play a role in determining the relative populations of the two most commonly observed morphological forms (i.e. toroids and rods). Furthermore, it has been shown that an appreciable number of particles adopted a spherical morphology in the sample of DNA fragments shorter than 700 base pairs. This result was unexpected as the only appreciable morphology previously reported at such DNA lengths has been the rod morphology. Furthermore, the occurrence of a spherical morphology in the samples of this study with the shortest DNA fragment is not in predicted by the theory based on the thermodynamic considerations of toroid and sphere stability, which proposed spherical morphology to become more stable with an increase in DNA fragment length (77). Thus, the theoretical treatment of spherical condensate morphology is inadequate and further studies are required to understand the factors governing the formation of this morphology.

7.2. The structure of sperm cell chromatin and spermatogenesis

As an example of DNA packing by naturally occurring condensing agents, we have studied the condensation of DNA by bull sperm cell protamines. The results of a modeling study suggest a high level of regularity in the local arrangement of condensed genomic DNA in the presence of bull protamines. An inspection of the proposed model

of bull sperm cell chromatin local structure suggests that the experimentally observed structural stability of mammalian sperm cell chromatin might not derive only from the ability of bull protamine to form intermolecular disulfide bonds to its neighbors. Rather, the arrangement of individual bull protamine molecules on a DNA strand relative to bull protamine molecules bound on the neighboring DNA strands in the chromatin should enable the formation of an extended network of bull protamines.

As noted above, our study of *in vitro* DNA condensation model systems demonstrated that condensate morphology and size are governed at all stages of DNA condensation by various kinetic as well as thermodynamic factors. Thus, it comes as no surprise that naturally observed DNA condensation processes are controlled by many different proteins, ensuring that packing and repacking of genomic DNA proceeds undisturbed and yields consistently the same chromatin structure (16,113,114,118,160,182,183,186,189,190,212-214). For example, the proposed local structure of the mature bull sperm cell chromatin results from a complicated process of spermatogenesis, during which histones are displaced by protamines. A number of modification events, most likely possessing, priming or modulating function, accompany this displacement. These include amongst others: acetylation, ubiquitinization, ADP-ribosylation, phosphorylation, and methylation of histones, and the phosphorylation and ADP-ribosylation of protamines (189).

7.3. Future Work: A quantitative study of DNA condensation

Experimental investigations of DNA condensate formation mechanisms remain at a mostly qualitative stage (63,96,102). We have now compiled considerable evidence that

condensate size and morphology can be either kinetically or thermodynamically limited, depending upon the specific conditions of condensation. However, we are still lacking a quantitative and thermodynamically rigorous description of DNA toroid formation.

There have been a number of excellent quantitative experimental studies reported on the thermodynamics and kinetics of DNA condensation (54,91,94,215). However, most of these measurements have required DNA concentrations that are too high to allow formation of discrete DNA toroids (31,32,39), and therefore must constitute measurements of DNA aggregation thermodynamics rather than the thermodynamics of toroid formation. Even though the fundamental energetic factors responsible for the attractive potential between individual strands in DNA condensates may be independent of DNA concentration (215), the thermodynamics of individual steps of toroid formation (i.e. nucleation and subsequent toroid growth) cannot be obtained at high DNA concentrations where aggregation prevails and proceeds through a potentially different pathway.

The combination of thermodynamic/kinetic studies of DNA growth with single molecule techniques that use solution conditions known to promote DNA condensate formation could provide the quantitative picture that is still lacking. Single molecule studies have already proven extremely useful for understanding the nucleation and growth kinetics of intramolecular condensate formation (19,90,91,94,169,216,217). The application of similar techniques to the study of DNA condensate growth under conditions that allow for multimolecular condensate formation could be equally revealing. Furthermore, the analysis of experimental data on DNA condensation mechanisms by rigorous theoretical models for toroid nucleation and growth should

continue to prove very enlightening. The realization of a qualitative understanding of DNA toroid formation will likely be of great utility in our quest to achieve complete control over DNA assembly *in vitro*, which is believed to be essential for optimizing applications that require DNA condensation (e.g. gene therapy). Finally, a deeper understanding of DNA toroid formation *in vitro* should provide valuable insights into organisms that package DNA in a toroidal morphology (218,219).

7.3.1. DNA condensate nucleation

The temporal studies presented here of DNA condensate morphology demostrated, that the relative rod population is initially higher than its quasi-equilibrium value. The opposite being true for relative toroid population. It is important to determine the initial relative population not only to quantitatively understand the kinetics and thermodynamics of DNA condensate nucleation, but also to be able to evaluate the validity of recent theories on the relative stabilities of proto-toroid and proto-rod structures (23,142).

DNA condensation starts by an intramolecular collapse to form monomolecular proto-structures. Molecular and Brownian dynamics simulations as well as AFM studies have shown that proto-toroid and proto-rod structure are quiet different (23,61,93,142,143). Proto-toroid formation is initiated by nucleation loop formation along a DNA polymer, which results in a spool-like structure of a proto-toroid. On the other hand, a proto-rod structure may be most appropriately described as a collapsed proto-toroid structure.

Due to the nature of sample preparation, transmission electron microscopy (TEM) cannot be used to probe reaction times shorter than 2 min. This limitation prevents us

from investigating the initial rod and toroid populations (i.e. before the formation of multimolecular condensates) by TEM. Tapping-mode atomic force microscopy (AFM) under fluid can visualize monomolecular complexes (220,221), and could be used to investigate monomolecular condensates. The analysis of monomolecular condensate morphologies and the ratio between spooled and collapsed-spooled structures could then be used to assess the initial toroid and rod populations. Experimental investigation of monomolecular condensate morphology with AFM would also enable us to quantitatively study solution and other effects on DNA condensate morphology and stability directly rather then indirectly through investigation of multimolecular condensates.

7.3.2 DNA Condensate Growth

The kinetics and thermodynamics of DNA condensation growth have been poorly investigated as well. Besides Bloomfield and coworkers (54), there have been only a few kinetic studies of condensate growth reported in the literature. Recently, a stopped-flow flourimetry has been applied to kinetic studies of DNA condensation (120). Nevertheless, even though Tecle et al. could measure two rate constants associated with DNA condensation, they could not be related to any of the specific steps in the mechanism of DNA condensation.

7.3.2.1. Thermodynamic limit of toroid size

The factors governing toroid size limits have been a subject of intense research. Even though theoretical studies of DNA condensation has analyzed the kinetic as well as thermodynamic factors governing the formation of DNA condensates, it has been

impossible to separate experimentally these parametersin. In spite of this, experimental toroid sizes have been used to evaluate different theoretical models. However, it is necessary to first obtain thermodynamic toroid size limit to be able to evaluate any theoretical analysis of thermodynamic factors governing toroid formation.

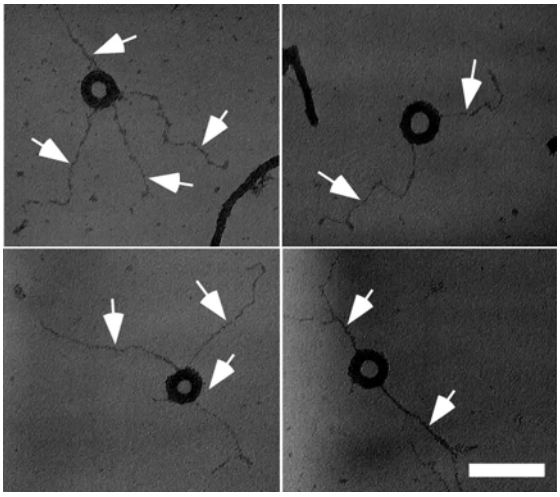

Figure 7.1 Representative TEM images of uncondensed DNA protruding from toroids after 2 min reaction time. Equal volumes of plasmid DNA and hexammine cobalt were mixed in a low ionic strength buffer (5 mM Tris, 0.5 mM EDTA, pH 7.6) at 10 μg/mL, and 100 μM final concentrations of DNA and hexammine cobalt, respectively. The reaction mixture was allowed to condense for 2 min before TEM grid preparation. All four TEM images were obtained with the same sample. Uncondensed DNA is indicated with white arrows. The scale bar represents 100 nm. All TEM images are at the same magnification.

It is now clear that toroid sizes usually measured in a condensation reaction are determined by the kinetics as well as the thermodynamics of the reaction. Thus, a true thermodynamic limit of toroid size has been hard to evaluate experimentally. Nevertheless, different experimental approaches have been used in attempts to determine a thermodynamic limit to toroid size (102,104-106). Very large toroids were obtained by

Lambert et al. by injection of DNA from multiple viral capsids into a liposome; however, the toroid size was not completely under thermodynamic control as the size of the liposomes also influenced the toroid maximum size. Some groups have attempted to identify toroids that reached their thermodynamically limited size by the presence of uncondensed DNA protruding from the surface of the particle (102,104,105). Our recent data shows that similar structures with the free uncondensed DNA protruding from the surface of toroids can be observed in a low ionic strength buffer after a 2 min reaction time, when toroids still have not reached their equilibrium size (Figure 7.1). This implies that the uncondensed DNA protruding from the structure can either be DNA that could not add to the condensed particle anymore (thermodynamic interpretation) or uncondensed DNA that was ethanol precipitated during its deposition onto a growing toroid (kinetic interpretation).

Our data show that we can increase condensate growth rate relatively to their aggregation by condensing free DNA in the presence of pre-condensed DNA that serve as nucleation sites, similar to the seeding process in crystallization protocols (Figure 7.2). It should be possible to optimize this protocol until one that yields condensates that are thermodynamically limited. Optimization of this protocol could include determination of the optimum time point at which to inject free DNA into a solution of preformed condensates. Also, an optimum number of free DNA additions should be determined as each addition would dilute the reaction mixture, thus, decreasing the concentration of nucleation sites (i.e. preformed toroids). Inevitably, since DNA condensation would still be partly under a kinetic control, there will be a distribution of toroid sizes present;

however, the largest condensates would be expected to increase with each addition of free DNA.

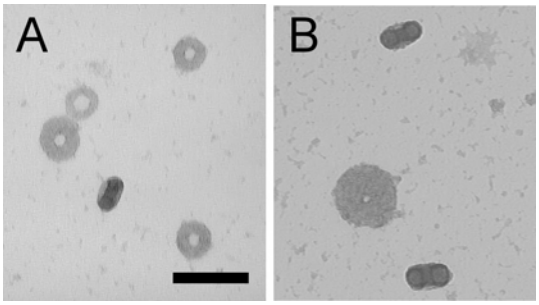

Figure 7.2 Toroids dimensions depend on the order of solution mixing in the absence of divalent ions as well. (A) Equal volumes of plasmid DNA and hexammine cobalt were mixed in a low ionic strength buffer (5 mM Tris, 0.5 mM EDTA, pH=7.6) at 10 μg/mL, and 100 μM final concentrations of DNA and hexammine cobalt, respectively. (B) The solution of pre-formed DNA condensates from panel A was supplied with fresh DNA and hexammine cobalt under the solution conditions to maintain final DNA and hexammine cobalt concentrations as well as ionic strength of the solution the same as in panel A. The solution of pre-formed DNA condensates was supplied fresh DNA and hexammine cobalt in total five times at intervals of 1 min. The scale bar in panel A represents 100 nm. Both TEM images are at the same magnification.

7.3.2.2. Free DNA and kinetics of DNA condensation reaction

Apart from equilibrium studies of free DNA concentration in DNA condensation reactions, there have been no kinetic studies reported that reveal the role of free DNA in the growth of DNA condensates. According to the current model of DNA condensation mechanism, free DNA should be an important driving force for DNA condensate growth. Growth kinetics would thus be expected to depend on the concentration of free DNA in solution. In addition, DNA condensate growth does not have to occur exclusively through collecting free DNA in solution. Our results suggest that condensate growth could also occur through DNA strand exchange between individual condensate (Figure 7.3). A

kinetic analysis of the free DNA concentration in DNA condensation reaction mixture should thus help us understand the (preferential) mode of DNA condensate growth.

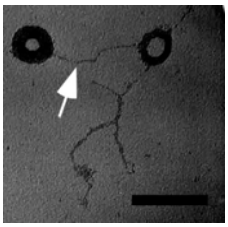

Figure 7.3 An example of two toroid DNA condensates sharing DNA, which is indicated by a white arrow. The scale bar represents 100 nm.

Equilibrium studies of DNA condensate resolubilization have applied centrifugation to separate condensed from uncondensed DNA (5,8,9). It should be possible to adopt similar protocols, that would allow one to analyze free DNA concentration within the time frame similar to the TEM studies reported above (> 2min). This would enable one to detect any correlation of DNA condensate growth and concentration of free DNA. Method of free DNA detection will depend on free DNA concentrations. For higher concentration ranges of free DNA, UV spectroscopy could be used, whereas in the lower concentration ranges detection by radioactive labeling of DNA could be used.

REFERENCES

1. Haynes, M., Garrett, R.A. and Gratzer, W.B. (1970) *Biochemistry*, 9, 4410-4416.

2. Evdokimov, Y.M., Platonov, A.L., Tikhonenko, A.S. and Varshavsky, Y.M. (1972) *FEBS Lett.*, 23, 180-184.

3. Gosule, L.C. and Schellman, J.A. (1976) *Nature*, 259, 333-335.

4. Burak, Y., Ariel, G. and Andelman, D. (2004) *Curr. Opin. Coll. Int. Sci.*, 9, 53-58.

5. Pelta, J., Livolant, F. and Sikorav, J.L. (1996) *J. Biol. Chem.*, 271, 5656-5662.

6. Post, C.B. and Zimm, B.H. (1979) *Biopolymers*, 18, 1487-1501.

7. Post, C.B. and Zimm, B.H. (1982) *Biopolymers*, 21, 2123-2137.

8. Raspaud, E.M., Olvera de la Cruz, M., Sikorav, J.L. and Livolant, F. (1998) *Biophys. J.*, 74, 381-393.

9. Saminathan, M., Antony, T., Shirahata, A., Sigal, L.H., Thomas, T. and Thomas, T.J. (1999) *Biochemistry*, 38, 3821-3830.

10. Widom, J. and Baldwin, R.L. (1980) *J. Mol. Biol.*, 144, 431-453.

11. Yoshikawa, K., Takahashi, M., Vasilevskaya, V.V. and Khokhlov, A.R. (1996) *Phys. Rev. Lett.*, 76, 3029-3031.

12. Nguyen, T.T., Rouzina, I. and Shklovskii, B.I. (2000) *J. Chem. Phys.*, 112, 2562-2568.

13. Bloomfield, V.A. (1991) *Biopolymers*, 31, 1471-1481.

14. Bloomfield, V.A. (1996) *Curr. Opin. Struct. Biol.*, 6, 334-341.

15. Cerritelli, M.E., Cheng, N.Q., Rosenberg, A.H., McPherson, C.E., Booy, F.P. and Steven, A.C. (1997) *Cell*, 91, 271-280.

16. Balhorn, R., Cosman, M., Thornton, K., Krishnan, V.V., Corzett, M., Bench, G., Kramer, C., Lee, J., IV, Hud, N.V., Allen, M. *et al.* (1999) In Gagnon, C. (ed.), *The Male Gamete: From Basic Knowledge to Clinical Applications*. Cache River Press, Vienna, IL, pp. 55-70.

17. Mahato, R.I., Takakura, Y. and Hashida, M. (1997) *Crit. Rev. Ther. Drug Carr. Syst.*, 14, 133-172.

18. Ubbink, J. and Odijk, T. (1995) *Biophys. J.*, 68, 54-61.

19. Takahashi, M., Yoshikawa, K., Vasilevskaya, V.V. and Khokhlov, A.R. (1997) *J. Phys. Chem. B*, 101, 9396-9401.

20. Park, S.Y., Harries, D. and Gelbart, W.M. (1998) *Biophys. J.*, 75, 714-720.
21. Ha, B.Y. and Liu, A.J. (1999) *Europhys. Lett.*, 46, 624-630.

22. Ivanov, V.A., Stukan, M.R., Vasilevskaya, V.V., Paul, W. and Binder, K. (2000) *Macromol. Theory Simul.*, 9, 488-499.

23. Sakaue, T. and Yoshikawa, K. (2002) *J. Chem. Phys.*, 117, 6323-6330.

24. Montesi, A., Pasquali, M. and MacKintosh, F.C. (2004) *Phys. Rev. E*, 69.

25. Lerman, L.S. (1971) *Proc. Natl. Acad. Sci. USA*, 68, 1886-1890.

26. Oosawa, F. (1971) *Polyelectrolytes*. Marcel Dekker, New York.

27. Manning, G.S. (1977) *Biophys. Chem.*, 7, 95-102.

28. Manning, G.S. (1978) *Biophys. Chem.*, 9, 65-70.

29. Wilson, R.W. and Bloomfield, V.A. (1979) *Biochemistry*, 18, 2192-2196.

30. Marquet, R. and Houssier, C. (1991) *J. Biomol. Struct. Dyn.*, 9, 159-167.

31. Leikin, S., Rau, D.C. and Parsegian, V.A. (1991) *Phys. Rev. A*, 44, 5272-5278.

32. Rau, D. and Parsegian, V. (1992) *Biophys. J.*, 61, 260-271.

33. Podgornik, R., Rau, D.C. and Parsegian, V.A. (1994) *Biophys. J.*, 66, 962-971.

34. Odijk, T. (1994) *Macromolecules*, 27, 4998-5003.

35. Wissenburg, P., Odijk, T., Cirkel, P. and Mandel, M. (1994) *Macromolecules*, 27, 306-308.

36. Ray, J. and Manning, G. (1994) *Langmuir*, 10, 2450-2461.

37. Lyubartsev, A.P. and Nordenskjld, L. (1995) *J. Phys. Chem.*, 99, 10373-10382.

38. Patel, M.M. and Anchordoguy, T.J. (2005) *Biophys. J.*, 88, 2089-2103.

39. Rau, D. and Parsegian, V. (1992) *Biophys. J.*, 61, 246-259.

40. Podgornik, R., Strey, H.H., Rau, D.C. and Parsegian, V.A. (1995) *Biophys. Chem.*, 57, 111-121.

41. Wissenburg, P., Odijk, T., Cirkel, P. and Mandel, M. (1995) *Macromolecules*, 28, 2315-2328.

42. Rouzina, I. and Bloomfield, V.A. (1996) *J. Phys. Chem.*, 100, 9977-9989.

43. Bloomfield, V.A. (1997) *Biopolymers*, 44, 269-282.

44. Ha, B.Y. and Liu, A.J. (1997) *Phys. Rev. Lett.*, 79, 1289-1292.

45. Strey, H.H., Podgornik, R., Rau, D.C. and Parsegian, V.A. (1998) *Curr. Opin. Struc. Biol.*, 8, 309-313.

46. Arenzon, J.J., Stilck, J.F. and Levin, Y. (1999) *Eur. Phys. J. B*, 12, 79-82.

47. Shklovskii, B.I. (1999) *Phys. Rev. E*, 60, 5802-5811.

48. Shklovskii, B.I. (1999) *Phys. Rev. Lett.*, 82, 3268-3271.

49. Gelbart, W.M., Bruinsma, R.F., Pincus, P.A. and Parsegian, V.A. (2000) *Phys Today*, 53, 38-44.

50. Deserno, M., Arnold, A. and Holm, C. (2003) *Macromolecules*, 36, 249-259.

51. GronbechJensen, N., Mashl, R.J., Bruinsma, R.F. and Gelbart, W.M. (1997) *Phys. Rev. Lett.*, 78, 2477-2480.

52. Besteman, K., Zevenbergen, M.A.G., Heering, H.A. and Lemay, S.G. (2004) *Phys. Rev. Lett.*, 93, 170802.

53. Park, S. and Healy, K.E. (2003) *Bioconjugate Chem.*, 14, 311-319.

54. He, S.Q., Arscott, P.G. and Bloomfield, V.A. (2000) *Biopolymers*, 53, 329-341.

55. Marquet, R., Wyart, A. and Houssier, C. (1987) *Biochim. Biophys. Acta*, 909, 165-172.

56. Arscott, P.G., Li, A.Z. and Bloomfield, V.A. (1990) *Biopolymers*, 30, 619-630.

57. Arscott, P., Ma, C., Wenner, J. and Bloomfield, V. (1995) *Biopolymers*, 36, 345-364.

58. Sarkar, T., Conwell, C.C., Harvey, L.C., Santai, C.T. and Hud, N.V. (2005) *Nucleic Acids Res.*, 33, 143-151.

59. Stevens, M.J. (1999) *Phys Rev Lett*, 82, 101-104.

60. Schnurr, B., MacKintosh, F.C. and Williams, D.R.M. (2000) *Europhys. Lett.*, 51, 279-285.

61. Stevens, M.J. (2001) *Biophys. J.*, 80, 130-139.

62. Schnurr, B., Gittes, F. and MacKintosh, F.C. (2002) *Phys Rev E*, 65, 061904.

63. Conwell, C.C., Vilfan, I.D. and Hud, N.V. (2003) *Proc. Natl. Acad. Sci. U. S. A.*, 100, 9296-9301.

64. Marx, K. and Rubin, G. (1983) *Nucleic Acids Res.*, 11, 1839-1854.

65. Marx, K.A. and Ruben, G.C. (1984) *J. Biomol. Struct. Dyn.*, 1, 1109-1132.

66. Hud, N. (1995) *Biophys. J.*, 69, 1355-1362.

67. Keller, D. and Bustamante, C. (1986) *J. Chem. Phys.*, 84, 2972-2981.

68. Schellman, J.A. and Parthasarathy, N. (1984) *J. Mol. Biol.*, 175, 313-329.

69. Gabashvili, I.S., Agrawal, R.K., Spahn, C.M.T., Grassucci, R.A., Svergun, D.I., Frank, J. and Penczek, P. (2000) *Cell*, 100, 537-549.

70. Zhou, Z.H., Dougherty, M., Jakana, J., He, J., Rixon, F.J. and Chiu, W. (2000) *Science*, 288, 877-880.

71. Bottcher, B., Endisch, C., Fuhrhop, J.-H., Catterall, C. and Eaton, M. (1998) *J. Am. Chem. Soc.*, 120, 12-17.

72. Hud, N.V. and Downing, K.H. (2001) *Proc. Natl. Acad. Sci. U. S. A.*, 98, 14925-14930.

73. Suwalsky, M. and Traub, W. (1972) *Biopolymers*, 11, 2223-2231.

74. Maniatis, T., Venable, J.J. and Lerman, L. (1974), 84, 37-64.

75. Manning, G.S. (1980) *Biopolymers*, 19, 37-59.

76. Hud, N.V., Downing, K.H. and Balhorn, R. (1995) *Proc. Natl. Acad. Sci. U. S. A.*, 92, 3581-3585.

77. Vasilevskaya, V.V., Khokhlov, A.R., Kidoaki, S. and Yoshikawa, K. (1997) *Biopolymers*, 41, 51-60.

78. Laemmli, U.K. (1975) *Proc. Natl. Acad. Sci. USA*, 72, 4288-4292.

79. Hsiang, M.W. and Cole, R.D. (1977) *Proc. Natl. Acad. Sci. USA*, 74, 4852-4856.

80. Chattoraj, D.K., Gosule, L.C. and Schellman, J.A. (1978) *J. Mol. Biol.*, 121, 327-337.

81. Hud, N.V., Allen, M.J., Downing, K.H., Lee, J. and Balhorn, R. (1993) *Biochem. Biophys. Res. Commun.*, 193, 1347-1354.

82. Park, S.Y., Bruinsma, R.F. and Gelbart, W.M. (1999) *Europhys. Lett.*, 46, 454-460.

83. Messina, R., Gonzalez-Tovar, E., Lozada-Cassou, M. and Holm, C. (2002) *Europhys. Lett.*, 60, 383-389.

84. Levin, Y. and Arenzon, J.J. (2003) *J Phys A- Math Gen*, 36, 5857-5863.

85. Kuznetsov, Y.A., Timoshenko, E.G. and Dawson, K.A. (1996) *J. Chem. Phys.*, 105, 7116-7134.

86. Ha, B.-Y. and Liu, A.J. (1998) *Phys Rev Lett*, 81, 1011-1014.

87. Pereira, G.G. and Williams, D.R.M. (2000) *Europhys. Lett.*, 50, 559-564.

88. Nguyen, T.T. and Shklovskii, B.I. (2002) *Phys Rev E*, 65, Art. No. 031409.

89. Stilck, J.F., Levin, Y. and Arenzon, J.J. (2002) *J. Stat. Phys.*, 106, 287-299.

90. Yoshikawa, K. and Matsuzawa, Y. (1996) *J. Am. Chem. Soc.*, 118, 929-930.

91. Brewer, L.R., Corzett, M. and Balhorn, R. (1999) *Science*, 286, 120-123.

92. Baumann, C.G., Bloomfield, V.A., Smith, S.B., Bustamante, C. and Wang, M.D. (2000) *Biophys. J.*, 78, 1965-1978.

93. Noguchi, H. and Yoshikawa, K. (2000) *J. Chem. Phys.*, 113, 854-862.

94. Su, T.J., Theofanidou, E., Arlt, J., Dryden, D.T.F. and Crain, J. (2004) *J. Fluoresc.*, 14, 65-69.

95. LaMer, V.K. and Dinegar, R.H. (1950) *J. Am. Chem. Soc.*, 72, 4847-4854.

96. Shen, M.R., Downing, K.H., Balhorn, R. and Hud, N.V. (2000) *J. Am. Chem. Soc.*, 122, 4833-4834.

97. Rivetti, C., Walker, C. and Bustamante, C. (1998) *J. Mol. Biol.*, 280, 41-59.

98. Rouzina, I. and Bloomfield, V.A. (1996) *J. Phys. Chem.*, 100, 4292-4304.

99. Porschke, D. (1986) *J. Biomol. Struct. Dyn.*, 4, 373-389.

100. Hagerman, P.J. (1988) *Annu. Rev. Biophys. Biophys. Chem.*, 17, 265-286.

101. Lu, Y.J., Weers, B. and Stellwagen, N.C. (2001) *Biopolymers*, 61, 261-275.

102. Conwell, C.C. and Hud, N.V. (2004) *Biochemistry*, 43, 5380-5387.

103. Conwell, C.C. and Hud, N.V. (2003) *J. Clust. Sci.*, 14, 115-122.

104. Allison, S.A., Herr, J.C. and Schurr, J.M. (1981) *Biopolymers*, 20, 469-488.

105. Yoshikawa, Y., Yoshikawa, K. and Kanbe, T. (1999) *Langmuir*, 15, 4085-4088.

106. Lambert, O., Letellier, L., Gelbart, W.M. and Rigaud, J.L. (2000) *Proc. Natl. Acad. Sci. USA*, 97, 7248-7253.

107. Kuznetsov, Y.A. and Timoshenko, E.G. (1999) *J. Chem. Phys.*, 111, 3744-3752.

108. Voet, D. and Voet, J.G. (1995) *Biochemistry*. 2nd ed. John Wiley & Sons, New York City.

109. Tzlil, S., Kindt, J.T., Gelbart, W.M. and Ben-Shaul, A. (2003) *Biophys. J.*, 84, 1616-1627.

110. Ali, I., Marenduzzo, D. and Yeomans, J.M. (2004) *J. Chem. Phys.*, 121, 8635-8641.

111. Purohit, P.K., Inamdar, M.M., Grayson, P.D., Squires, T.M., Kondev, J. and Phillips, R. (2005) *Biophys. J.*, 88, 851-866.

112. Allen, M.J., Lee, C., Lee, J.D., Pogany, G.C., Balooch, M., Siekhaus, W.J. and Balhorn, R. (1993) *Chromosoma*, 102, 623-630.

113. Kornberg, R.D. and Lorch, Y.L. (1999) *Cell*, 98, 285-294.

114. Struhl, K. (1999) *Cell*, 98, 1-4.

115. Holmes, V.F. and Cozzarelli, N.R. (2000) *Proc. Natl. Acad. Sci. U. S. A.*, 97, 1322-1324.

116. Balhorn, R. (1989) In Adolph, K. W. (ed.), *Molecular Biology of Chromosome Function*. 1 ed. Springer-Verlag, New York, pp. 366-395.

117. Tovich, P.R. and Oko, R.J. (2003) *J. Biol. Chem.*, 278, 32431-32438.

118. Santi, S., Rubbini, S., Cinti, C., Squarzoni, S., Matteucci, A., Caramelli, E., Guidotti, L. and Maraldi, N.M. (1994) *Biol. Cell*, 81, 47-57.

119. Vijayanathan, V., Thomas, T., Shirahata, A. and Thomas, T.J. (2001) *Biochemistry*, 40, 13644-13651.

120. Tecle, M., Preuss, M. and Miller, A.D. (2003) *Biochemistry*, 42, 10343-10347.

121. Doye, J.P.K., Sear, R.P. and Frenkel, D. (1998) *J. Chem. Phys.*, 108, 2134-2142.

122. Kolinski, A., Skolnick, J. and Yaris, R. (1986) *J. Chem. Phys.*, 85, 3585-3597.

123. Noguchi, H. and Yoshikawa, K. (1998) *J. Chem. Phys.*, 109, 5070-5077.

124. Deng, H. and Bloomfield, V.A. (1999) *Biophys. J.*, 77, 1556-1561.

125. Schnell, J.R., Berman, J. and Bloomfield, V.A. (1998) *Biophys. J.*, 74, 1484-1491.

126. Hud, N.V. and Plavec, J. (2003) *Biopolymers*, 69, 144-159.

127. Rouzina, I. and Bloomfield, V.A. (1997) *Biophys. Chem.*, 64, 139-155.

128. Podtelezhnikov, A.A. and Vologodskii, A.V. (2000) *Macromolecules*, 33, 2767-2771.

129. Shimada, J. and Yamakawa, H. (1984) *Macromolecules*, 17, 689-698.

130. Baumann, C.G., Smith, S.B., Bloomfield, V.A. and Bustamante, C. (1997) *Proc. Natl. Acad. Sci. USA*, 94, 6185-6190.

131. Stukan, M.R., Ivanov, V.A., Grosberg, A.Y., Paul, W. and Binder, K. (2003) *J. Chem. Phys.*, 118, 3392-3400.

132. Golo, V.L., Evdokimov, Y.M. and Kats, E.I. (1997) *J. Exp. Theor. Phys.*, 85, 1180-1186.

133. Ubbink, J. and Odijk, T. (1996) *Europhys. Lett.*, 33, 353-358.

134. Widom, J. and Baldwin, R.L. (1983) *Biopolymers*, 22, 1595-1620.

135. Vilfan, I.D., Conwell, C.C. and Hud, N.V. (2004) *J. Biol. Chem.*, 279, 20088-20095.

136. Arscott, P.G., Ma, C.L., Wenner, J.R. and Bloomfield, V.A. (1995) *Biopolymers*, 36, 345-364.

137. Shore, D., Langowski, J. and Baldwin, R.L. (1981) *Proc. Natl. Acad. Sci. U. S. A.*, 78, 4833-4837.

138. Cloutier, T.E. and Widom, J. (2004) *Molecular Cell*, 14, 355-362.

139. Yan, J. and Marko, J.F. (2004) *Phys. Rev. Lett.*, 93.

140. Wiggins, P.A., Phillips, R. and Nelson, C.N. (2005) *Phys. Rev. E*, 71, Art. No. 021909.

141. Noguchi, H., Saito, S., Kidoaki, S. and Yoshikawa, K. (1996) *Chem. Phys. Lett.*, 261, 527-533.

142. Ou, Z. and Muthukumar, M. (2005) *J. Chem. Phys.*, In press.

143. Martin, A.L., Davies, M.C., Rackstraw, B.J., Roberts, C.J., Stolnik, S., Tendler, S.J.B. and Williams, P.M. (2000) *FEBS Lett.*, 480, 106-112.

144. Dauty, E., Remy, J.S., Blessing, T. and Behr, J.P. (2001) *J. Am. Chem. Soc.*, 123, 9227-9234.

145. Stevens, M.J. and Kremer, K. (1995) *J. Chem. Phys.*, 103, 1669-1690.

146. Ivanov, V.A., Paul, W. and Binder, K. (1998) *J. Chem. Phys.*, 109, 5659-5669.

147. Conwell, C.C. (2004), Georgia Institute of Technology, Atlanta.

148. Lewis, J.D., Song, Y., de Jong, M.E., Bagha, S.M. and Ausio, J. (2003) *Chromosoma*, 111, 473-482.

149. Balhorn, R., Corzett, M., Mazrimas, J. and Watkins, B. (1991) *Biochemistry*, 30, 175-181.

150. Da Silva, L.B., Trebes, J.E., Balhorn, R., Mrowka, S., Anderson, E., Attwood, D.T., Barbee, T.W., Brase, J., Corzett, M., Gray, J. *et al.* (1992) *Science*, 258, 269-271.

151. Balhorn, R., Corzett, M. and Mazrimas, J.A. (1992) *Arch. Biochem. Biophys.*, 296, 384-393.

152. Bianchi, F., Rousseauxprevost, R., Bailly, C. and Rousseaux, J. (1994) *Biochem. Biophys. Res. Commun.*, 201, 1197-1204.

153. Hud, N.V., Milanovich, F.P. and Balhorn, R. (1994) *Biochemistry*, 33, 7528-7535.

154. Allen, M.J., Bradbury, E.M. and Balhorn, R. (1995) *J. Struct. Biol.*, 114, 197-208.

155. Bench, G.S., Friz, A.M., Corzett, M.H., Morse, D.H. and Balhorn, R. (1996) *Cytometry*, 23, 263-271.

156. Allen, M.J., Bradbury, E.M. and Balhorn, R. (1997) *Nucleic Acids Res.*, 25, 2221-2226.

157. Prieto, M.C., Maki, A.H. and Balhorn, R. (1997) *Biochemistry*, 36, 11944-11951.

158. Quintanilla-Vega, B., Hoover, D., Bal, W., Silbergeld, E.K., Waalkes, M.P. and Anderson, L.D. (2000) *Am. J. Ind. Med.*, 38, 324-329.

159. Balhorn, R., Brewer, L. and Corzett, M. (2000) *Mol. Reprod. Dev.*, 56, 230-234.

160. Gimenez-Bonafe, P., Ribes, E., Sautiere, P., Gonzalez, A., Kasinsky, H., Kouach, M., Sautiere, P.E., Ausio, J. and Chiva, M. (2002) *Eur. J. Cell Biol.*, 81, 341-349.

161. Koehler, J.K. (1966) *J. Ultrastruct. Res.*, 16, 359-375.

162. Koehler, J.K. (1970) *J. Ultrastruct. Res.*, 33, 598-614.

163. Koehler, J.K., Wurschmidt, U. and Larsen, M.P. (1983) *Gamete Res.*, 8, 357-370.

164. Adroer, R., Queralt, R., Ballabriga, J. and Oliva, R. (1992) *Nucleic Acids Res.*, 20, 609-609.

165. Balhorn, R. (1982) *J. Cell Biol.*, 93, 298-305.

166. Fita, I., Campos, J.L., Puigjaner, L.C. and Subirana, J.A. (1983) *J. Mol. Biol.*, 167, 157-177.

167. Verdaguer, N., Perelló, M., Palau, J. and Subirana, J.A. (1993) *Eur. J. Biochem.*, 214, 879-887.

168. Raukas, E. and Mikelsaar, R.H. (1999) *Bioessays*, 21, 440-448.

169. Brewer, L., Corzett, M., Lau, E.Y. and Balhorn, R. (2003) *J. Biol. Chem.*, 278, 42403-42408.

170. Balhorn, R., Gledhill, B.L. and Wyrobek, A.J. (1977) *Biochemistry*, 16, 4074-4080.

171. Ammer, H. and Henschen, A. (1987) *Biol. Chem. Hoppe-Seyler*, 368, 1619-1626.

172. Creighton, T.E. (1993) *Proteins: Structures and Molecular Properties*. 2nd ed. W. H. Freeman & Co., New York.

173. Loir, M., Bouvier, D., Fornells, M., Lanneau, M. and Subirana, J.A. (1985) *Chromosoma*, 92, 304-312.

174. Blanc, N.S., Senn, A., Leforestier, A., Livolant, F. and Dubochet, J. (2001) *J. Struct. Biol.*, 134, 76-81.

175. Sorgi, F.L., Bhattacharya, S. and Huang, L. (1997) *Gene Ther*, 4, 961-968.

176. Berne, B.J. and Pecora, R. (2000) *Dynamic Light Scattering with Applications to Chemistry, Biology, and Physics*. Dover Publications, Inc., New York.

177. Bloomfield, V.A. (2000) *Biopolymers*, 54, 168-172.

178. Zintchenko, A., Rother, G. and Dautzenberg, H. (2003) *Langmuir*, 19, 2507-2513.

179. Lin, X.M., Wang, G.M., Sorensen, C.M. and Klabunde, K.J. (1999) *J. Phys. Chem. B*, 103, 5488-5492.

180. Fernandez-Barbero, A., Fernandez-Nieves, A., Grillo, I. and Lopez-Cabarcos, E. (2002) *Phys. Rev. E*, 66, art. no.-051803.

181. Suau, P. and Subirana, J.A. (1977) *J. Mol. Biol.*, 117, 909-926.

182. Alfert, M. (1956) *J. Biophys. Biochem. Cytol.*, 2, 109-114.

183. Marushige, K. and Dixon, G.H. (1969) *Dev. Biol.*, 19, 397-414.

184. Louie, A.J. and Dixon, G.H. (1972) *J. Biol. Chem.*, 247, 7962-7968.

185. Honda, B.M., Dixon, G.H. and Candido, E.P. (1975) *J. Biol. Chem.*, 250, 8681-8685.

186. Louie, A.J. and Dixon, G.H. (1975) *Proc. Nat. Acad. Sci. USA*, 69, 1975-1979.

187. Agell, N., Chiva, M. and Mezquita, C. (1983) *FEBS Lett.*, 155, 209-212.

188. Corominas, M. and Mezquita, C. (1985) *J. Biol. Chem.*, 260, 16269-16273.

189. Oliva, R. and Dixon, G.H. (1991) *Prog. Nucleic Acid Res. Mol. Biol.*, 40, 25-94.

190. Dadoune, J.P. (1995) *Micron*, 26, 323-345.

191. Saenger, W. (1984) *Principles of Nucleic Acid Structure*. Springer-Verlag, New York.

192. Rooney, A.P. and Zhang, J.Z. (1999) *Mol. Biol. Evol.*, 16, 706-710.

193. Rooney, A.P., Zhang, J.Z. and Nei, M. (2000) *Mol. Biol. Evol.*, 17, 278-283.

194. Torgerson, D.G., Kulathinal, R.J. and Singh, R.S. (2002) *Mol. Biol. Evol.*, 19, 1973-1980.

195. Tanford, C. (1961) *Physical Chemistry of Macromolecules*. John Wiley & Sons, New York.

196. van Holde, K.E., Johnson, W.C. and Ho, P.S. (1998) *Principles of Physical Biochemistry*. 3rd ed. Prentice-Hall, Inc., Upper Saddle River, New Jersey.

197. Volk, N., Vollmer, D., Schmidt, M., Oppermann, W. and Huber, K. (2004) *Adv. Polym. Sci.*, 166, 29-65.

198. Ubbink, J. and Schar-Zammaretti, P. (2005) *Micron*, 36, 293-320.

199. Cao, A. (2003) *Anal. Lett.*, 36, 3185-3225.

200. Svergun, D.I. and Koch, M.H.J. (2003) *Rep. Prog. Phys.*, 66, 1735-1782.

201. Ferre Da Amare, A.R. and Burley, S.K. (1997) *Methods Enzymol.*, 276, 157-166.

202. Borsali, R. (1996) *Macromol. Chem. Phys.*, 197, 3947-3994.

203. Lodge, T. (1994) *Microchim Acta*, 116, 1-31.

204. Langowski, J., Kremer, W. and Kapp, U. (1992) *Methods Enzymol.*, 211, 430-448.

205. Schurr, J.M. and Schmitz, K.S. (1986) *Annu. Rev. Phys. Chem.*, 37, 271-305.

206. Leng, J., Egelhaaf, S.U. and Cates, M.E. (2003) *Biophys. J.*, 85, 1624-1646.

207. Dragan, A.I., Potekhin, S.A., Sivolob, A., Lu, M. and Privalov, P.L. (2004) *Biochemistry*, 43, 14891-14900.

208. Fang, Y. and Hoh, J.H. (1998) *J. Am. Chem. Soc.*, 120, 8903-8909.

209. Plum, G.E., Arscott, P.G. and Bloomfield, V.A. (1990) *Biopolymers*, 30, 631-643.

210. Pecora, R. (1968) *J. Chem. Phys.*, 49, 1032-1035.

211. Schurr, J.M. (1977) *Biopolymers*, 16, 461-464.

212. Oliva, R., Mezquita, J., Mezquita, C. and Dixon, G.H. (1988) *Dev. Biol.*, 125, 332-340.

213. Gassmann, R., Vagnarelli, P., Hudson, D. and Earnshaw, W.C. (2004) *Exp. Cell Res.*, 296, 35-42.

214. Redi, C.A., Garagna, S. and Zuccotti, M. (1990) *Biol. J. Linn. Soc.*, 41, 235-255.

215. Matulis, D., Rouzina, I. and Bloomfield, V.A. (2000) *J. Mol. Biol.*, 296, 1053-1063.

216. Brewer, L., Corzett, M. and Balhorn, R. (2002) *J. Biol. Chem.*, 277, 38895-38900.

217. Minagawa, K., Y., M., Yoshikawa, K., Khokhlov, A.R. and Doi, M. (1994), 34, 555-558.

218. Englander, J., Klein, E., Brumfeld, V., Sharma, A.K. and Minsky, A. (2004) *J. Bacteriol.*, 186, 5973-5977.

219. Zimmerman, S.B. (2002) *J. Struct. Biol.*, 138, 199-206.

220. Thomson, N.H., Smith, B.L., Almqvist, N., Schmitt, L., Kashlev, M., Kool, E.T. and Hansma, P.K. (1999) *Biophys. J.*, 76, 1024-1033.

221. Hansma, H.G., Golan, R., Hsieh, W., Daubendiek, S.L. and Kool, E.T. (1999) *J. Struct. Biol.*, 127, 240-247.

Vita

Igor Draško Vilfan was born on August 7th, 1976 in Ljubljana, Slovenia, where he attended *'Gimnazija Vič'* (Gymnasium Vič) and graduated in the top of his class in June 1995 after successfully passing the *'Matura'* (the National Advanced Level Examination). From there, he enrolled at *'Univerza v Ljubljani'* (University of Ljubljana) where he attened *'Fakulteta za kemijo in kemijsko tehnologijo'* (School of Chemistry and Chemical Engineering). He graduated in June 2000 with a Bachelor of Science degree in Chemistry after successfully defending his thesis titled *'Binding of ciprofloxacin to oligomeric and polymeric nucleic acids at different ionic strengths'*. Igor pursued his graduate studies in the School of Chemistry and Biochemistry at Georgia Institute of Technology in Atlanta, Georgia, USA.